AFRL-OSR-VA-TR-2015-0041

MULTI-SCALE EXPERIMENTS AND MODELING IN WALL TURBULENCE

Beverley Mckeon
CALIFORNIA INSTITUTE OF TECHNOLOGY

12/23/2014
Final Report

DISTRIBUTION A: Distribution approved for public release.

Air Force Research Laboratory
AF Office Of Scientific Research (AFOSR)/ RTE
Arlington, Virginia 22203
Air Force Materiel Command

REPORT DOCUMENTATION PAGE

Form Approved
OMB No. 0704-0188

Public reporting burden for this collection of information is estimated to average 1 hour per response, including the time for reviewing instructions, searching existing data sources, gathering and maintaining the data needed, and completing and reviewing this collection of information. Send comments regarding this burden estimate or any other aspect of this collection of information, including suggestions for reducing this burden to Department of Defense, Washington Headquarters Services, Directorate for Information Operations and Reports (0704-0188), 1215 Jefferson Davis Highway, Suite 1204, Arlington, VA 22202-4302. Respondents should be aware that notwithstanding any other provision of law, no person shall be subject to any penalty for failing to comply with a collection of information if it does not display a currently valid OMB control number. **PLEASE DO NOT RETURN YOUR FORM TO THE ABOVE ADDRESS.**

1. REPORT DATE *(DD-MM-YYYY)*
19-12-2014

2. REPORT TYPE
FINAL

3. DATES COVERED *(From - To)*
Oct. 2009 - Sept. 2014

4. TITLE AND SUBTITLE
Pecase-Multi-Scale Experiements And Modeling In Wall Turbulence

5a. CONTRACT NUMBER
FA9550-09-1-0701

5b. GRANT NUMBER

5c. PROGRAM ELEMENT NUMBER

6. AUTHOR(S)
MCKEON, BEVERLEY J.

5d. PROJECT NUMBER

5e. TASK NUMBER

5f. WORK UNIT NUMBER

7. PERFORMING ORGANIZATION NAME(S) AND ADDRESS(ES)
CALIFORNIA INSTITUTE OF TECHNOLOGY
1200 E. CALIFORNIA BLVD, MC 301-46
PASADENA, CA 91125

8. PERFORMING ORGANIZATION REPORT NUMBER

9. SPONSORING / MONITORING AGENCY NAME(S) AND ADDRESS(ES)

Air Force Office of Scientific Research (AFOSR)
875 N. Randolph St. Room 3112
Arlington, VA 22203

10. SPONSOR/MONITOR'S ACRONYM(S)

11. SPONSOR/MONITOR'S REPORT NUMBER(S)

12. DISTRIBUTION / AVAILABILITY STATEMENT

Distribution A - Approved for public release

13. SUPPLEMENTARY NOTES

14. ABSTRACT

A systems approach by which to understand the characteristics and scaling of wall turbulence, resolvent analysis (or critical later framework) has been developed, implemented and reported. The approach is in essence a transfer function analysis of the linear Navier-Stokes operator in the streamwise/spanwise wavenumber and temporal frequency space, which identifies and makes use of the low rank nature of this operator in order to achieve order reduction. The outputs have been shown to capture key elements of the turbulence, from statistics to spectral information to arrays of coherent structure. Supporting experiments and modeling have been performed to provide first comprehensive evidence of where in wavenumber-frequency space turbulence activity occurs by characterizing the three-dimensional spectrum of the streamwise velocity fluctuations using time-resolved particle image velocimetry at a range of wall-normal locations, and extending a two-dimensional, three-component model to provide an approximate input mean velocity profile to the analysis. The full resolvent analysis has the potential to provide a self-consistent and self-sustaining model of turbulence.

15. SUBJECT TERMS

Wall turbulence, resolvent analysis, mean profile modeling, spectrum of turbulence

16. SECURITY CLASSIFICATION OF:			**17. LIMITATION OF ABSTRACT**	**18. NUMBER OF PAGES**	**19a. NAME OF RESPONSIBLE PERSON** Beverley McKeon
a. REPORT UU	**b. ABSTRACT** UU	**c. THIS PAGE** UU	UU	90	**19b. TELEPHONE NUMBER** *(include area code)* 626 395 4460

Standard Form 298 (Rev. 8-98)
Prescribed by ANSI Std. Z39.18

FINAL REPORT

Grant # FA9550-09-1-0701

PECASE - Multi-scale experiments and modeling in wall turbulence

Beverley J. McKeon
Graduate Aerospace Laboratories
California Institute of Technology
Pasadena, CA 91125

Abstract

A systems approach by which to understand the characteristics and scaling of wall turbulence, resolvent analysis (or critical later framework) has been developed, implemented and reported in a range of archival publications, beginning with McKeon and Sharma [2010]. The approach is in essence a transfer function analysis of the linear Navier-Stokes operator in the streamwise/spanwise wavenumber and temporal frequency space, which identifies and makes use of the low rank nature of this operator in order to achieve order reduction. The outputs have been shown to capture key elements of the turbulence, from statistics to spectral information to arrays of coherent structure. Supporting experiments and modeling have been performed to provide first comprehensive evidence of where in wavenumber-frequency space turbulence activity occurs by characterizing the three-dimensional spectrum of the streamwise velocity fluctuations using time-resolved particle image velocimetry at a range of wall-normal locations, and extending a two-dimensional, three-component model to provide an approximate input mean velocity profile to the analysis. The full resolvent analysis has the potential to provide a self-consistent and self-sustaining model of turbulence, in which the velocity outputs have the correct amplitude and phase to support the appropriate input forcing and (presently assumed) mean velocity profile. Further work is proposed which exploits sparsity in the frequency domain associated with the resolvent formulation to further reduce the complexity of the representation of turbulence and to continue to explore the implications for the scaling of wall turbulence.

Contents

1 Introduction 5

1.1 Objectives 5

1.2 Dissemination of this work (excluding numerous oral presentations) 5

1.2.1 Archival journals 5

1.2.2 Conference papers 6

2 Approach and Summary of Results 7

2.1 Set-up 7

2.2 Summary of results 9

2.2.1 Key features of wall turbulence captured by resolvent analysis 9

2.2.2 TRPIV characterization of the three-dimensional power spectrum of streamwise velocity fluctuations 14

2.2.3 TRPIV tracking and characterization of individual turbulent structures and their convection velocities 15

2.2.4 Model for the mean velocity 15

3 Background 17

3.1 A brief review of linear processes in wall turbulence 17

3.2 Structure of the turbulent boundary layer 18

4 Critical layer framework 21

4.1 Turbulence as a directional amplifier 21

4.1.1 Formulation for the analysis 21

4.1.2 Optimal low-rank approximation of the resolvent for inhomogeneous coordinates 24

4.1.3 Response of radially-varying traveling waves and the connection with critical layer theory 26

4.1.4 Closing the loop: an explicit treatment of the nonlinearity 29

4.1.5 Where to look in 3D spectral space? 30

4.2 Reproduction and extension of statistical and structural results in unperturbed wall turbulence 30

4.2.1 Near-wall cycle 31

4.2.2 Characteristics of the very large scale motions 32

4.2.3 Hairpin vortices and structural organization 33

4.3 Summary 36

5 Experimental measurements of the frequency/wavenumber spectrum and coherent structure using time-resolved PIV 40

5.1 Experimental Setup 40

5.1.1 Measurements 42

5.1.2 Vector Processing 43

5.2 Flow Properties and Statistics 43

5.3 Spectral energy distributions 44

5.3.1 Calculation of the power spectral density in wall parallel planes 44

5.3.2 Spectral symmetries . . . 46
5.3.3 1D Spectra . . . 48
5.3.4 2D Spectra . . . 52
5.3.5 3D Spectra . . . 57
5.4 Identification of swirling coherent structures . . . 58
5.4.1 SCS identification technique . . . 58
5.4.2 SCS identification results . . . 59
5.5 Swirling coherent structure tracking . . . 62
5.5.1 SCS tracking technique . . . 62
5.5.2 SCS tracking results . . . 63
5.6 Implications for models of swirling coherent structure . . . 66
5.7 Summary of TRPIV results . . . 71

6 2D/3C model for the mean velocity in turbulent pipe flow 73
6.1 Model and numerical methods . . . 73
6.2 Simplified 2D/3C model with deterministic forcing . . . 74
6.3 Stochastic forcing of the 2D/3C model . . . 77
6.4 Summary . . . 81

7 Conclusions and Outlook 83

8 References 84

1 Introduction

The research performed under this PECASE award targeted multi-scale experiments and modeling in wall turbulence. The major contribution of the work has been the introduction and development of a novel, systems approach to understanding the behavior of unperturbed wall turbulence, which we refer to as "resolvent analysis".

1.1 Objectives

The specific objectives of the research, as listed in the original proposal, were as follows.

1. Perform first experimental measurements of the full frequency-streamwise/spanwise wavenumber spectrum in canonical and non-canonical turbulent boundary layers using fast Particle Image Velocimetry in order to identify the influence of multi-scale structure, wall-normal location and Reynolds number on the inferred dispersion relationship relating frequency and wavenumber;
2. Develop novel non-normal mode analysis of harmonic forcing of a canonical wall-bounded turbulent flow in order to categorize the extent, location and scaling properties of structures identified using a singular value decomposition of the linear operator;
3. Concatenate the results of the experimental and analytical projects in order to take steps towards a novel, low order, yet multi-scale, model of wall turbulence.

Significant effort was spent on each of these objectives, and we believe that progress has been made in each. The results have been disseminated widely. In this report, the over-arching approach will be summarized in the following section, before further technical details will be given in each area.

1.2 Dissemination of this work (excluding numerous oral presentations)

1.2.1 Archival journals

1. McKeon, B. J. and Sharma, A. (2010) "A critical layer framework for turbulent pipe flow", J. Fluid Mech.,658, 336-382.
2. Smits, A. J., McKeon, B. J. and Marusic, I. "High Reynolds number wall turbulence", Annual Review of Fluid Mechanics, 43, 2011.
3. LeHew, J., Guala, M. and McKeon, B. J. "A study of the three-dimensional spectral energy distribution in a zero pressure gradient turbulent boundary layer", Expts. in Fluids, 10.1007/s00348-011-1117-z (2011).
4. Jacobi, I. and McKeon, B. J. "New perspectives on the impulsive roughness perturbation of a turbulent boundary layer", J. Fluid Mech., 677, 179-203 (2011).
5. Bourguignon, J.-L. and McKeon, B. J. "A streamwise-constant model of turbulent pipe flow", Phys. Fluids, 23, 095111 (2011).
6. Sharma, A. and McKeon, B. J. "On coherent structure in wall turbulence", J. Fluid Mech. 728, 196-238 (2013); also ArXiV1301.7580, 2013.
7. LeHew, J., Guala, M. and McKeon, B. J. "Time-resolved measurements of coherent structures in the turbulent boundary layer", Expts. in Fluids, 54(4) (2013).
8. McKeon, B. J., Jacobi, I and Sharma, A. S. "Experimental manipulation of wall turbulence: a systems approach", Phys. Fluids 25(3) 10.1063/1.4793444 (2013).

9. Jacobi, I. and McKeon, B. J. “Phase relationships between large and small scales in the turbulent boundary layer”, Expts. in Fluids, 10.1007/s00348-013-1481-y (2013).
10. Moarref, R., Sharma, A. S., Tropp, J. A. and McKeon, B. J. “Model-based scaling of the streamwise energy density in high-Reynolds-number turbulent channels”, J. Fluid Mech., 734, 275-316 (2013).
11. Moarref, R., Jovanovic, M. R., Tropp, J. A., Sharma, A. S. and McKeon, B. J. “A low-order decomposition of turbulent channel flow via resolvent analysis and convex optimization”, Phys. Fluids, 26, 051701 (2014); also ArXiV 1401.6417, 2014.
12. Gómez Carrasco, F., Blackburn, H., Rudman, M., McKeon, B., Luhar, M., Moarref, R. and Sharma, A. “On the origin of frequency sparsity in direct numerical simulations of turbulent pipe flow”, Phys. Fluids 26, 101703 (2014).
13. Moarref, R., Sharma, A. S., Tropp, J. A. and McKeon, B. J. “A foundation for analytical developments in the logarithmic region of turbulent channels” (under review).

1.2.2 Conference papers

1. LeHew, J., Guala, M. and McKeon, B. J. “A study of convective velocities in a zero pressure gradient turbulent boundary layer” AIAA-2010-4474.
2. McKeon, B. J. and Sharma, A. S., “Energetic modes in turbulent pipe flow from resolvent analysis” AIAA-2010-697.
3. LeHew, J., Guala, M. and McKeon, B. J. “Structural and spectral analyisis of the turbulent boundary layer using time-resolved 2DPIV” PIV-11, Kobe, Japan (Ninth International Symposium on Particle Image Velocimetry), July 2011.
4. Bourguignon, J.-L. and McKeon, B. J. “A streamwise-constant model for turbulent pipe flow” TSFP-7, Ottowa (Turbulent Shear Flow Phenomena Symposium -7), July 2011.
5. LeHew, J., Guala, M. and McKeon, B. J. “A simultaneous physical and spectral analysis of the turbulent boundary layer via time-resolved particle image velocimetry” TSFP-7, Ottowa (Turbulent Shear Flow Phenomena Symposium -7), July 2011.
6. Jacobi, I. and McKeon, B. J. “Critical-layer behavior in an impulsively-perturbed turbulent boundary layer” TSFP-7, Ottowa (Turbulent Shear Flow Phenomena Symposium -7), July 2011.
7. Sharma, A. and McKeon, B. J. “Velocity statistics and structure in pipe turbulence derived from a simple critical-layer model” TSFP-7, Ottowa (Turbulent Shear Flow Phenomena Symposium -7), July 2011.
8. Sharma, A. S. and McKeon, B. J. “Closing the loop: an explicit treatment of the nonlinearity in the resolvent analysis of wall turbulence” AIAA-2013-3118.
9. Moarref, R., Sharma, A., Tropp, J. and McKeon, B. J. “Prediction of the streamwise turbulent energy spectrum in high Reynolds number channel flows” AIAA-2013-2480.
10. Moarref, R., Sharma, A. S., Tropp, J. A. and McKeon, B. J. “A predictive low-rank model for turbulent energy spectra at high Reynolds numbers” TSFP-8, Poitiers (Turbulent Shear Flow Phenomena Symposium -8), August 2013.
11. Moarref, R., Sharma, A., Tropp, J. and McKeon, B. J. “On scaling and interaction of the geometrically self-similar modes in turbulent channels” USNCTAM 2014.
12. Moarref, R., Park, J.-S., Sharma, A. S., Willis, A. P., Graham, M. D. and McKeon, B. J. “Approximation of the exact traveling wave solutions in wall-bounded flows using resolvent modes” TSFP-9, Melbourne (Turbulent Shear Flow Phenomena Symposium -9), July 2015 (to appear).

2 Approach and Summary of Results

2.1 Set-up

Our approach to the multiscale nature of wall turbulence has been to develop a scale-by-scale analysis with its foundations in systems analysis and connections with the non-normal mechanisms of disturbance amplification first explored in the extensive literature transient growth. This section gives a high-level description of the approach; further technical details on each aspect can be found in the subsequent sections and the publications listed in section 1.

While many studies have identified the potential for large amplification of disturbances due to the non-normality of the linearized Navier-Stokes operator (LNS), these have mostly been framed in the context of the search for the globally most amplified disturbances and associated flow response. In addition, the majority of work has been in the time domain, considering transient growth. These studies uniformly return streamwise constant, $k_x = 0$, disturbances as the worst-case, most amplified inputs and outputs. The connection to observable, "real" multiscale turbulence then requires further modeling, which has had limited success to-date. Ad-hoc assumptions are required to "shape" input disturbances to approach outputs that have physical relevance. The relevant literature is reviewed in section 3.

In the present work, we have sought to reframe the problem in terms of the disturbances giving rise to realizable features of turbulence, with a view to reconciling a range of observations and hypotheses concerning its structure and origin. As such, the analysis is constructed in the space in which experimental and numerical results are often reported, namely a Fourier decomposition of the velocity field. In particular, we consider the triple Fourier decomposition in the wall-parallel directions, and in time, leading to disturbance amplification systems for each assembly of streamwise and spanwise wavenumbers, and temporal frequency. The picture at each wavenumber/frequency combination is essentially that sketched in figure 1, in which the lower block represents the linear dynamics of fluctuations around the turbulent mean velocity profile, forced by nonlinear triadic interactions from other wavenumbers and frequencies.

At the heart of the theory developed under this grant are two insights. Firstly, that turbulence is robust. Secondly, that the robustness comes from a feedback loop involving the Navier-Stokes nonlinearity, which is energy-conserving, and a highly selective linear system, which leads to highly directional amplification. That is, the nonlinearity provides the correct shaping of the input forcing to sustain an output of a velocity field that corresponds to real turbulence.

Robustness may be defined as the ability of a system to operate in a similar way under a wide range of conditions and uncertainties. Wall turbulence is nothing if not robust, indeed, it is the persistence of complex, but recognizable, features that characterizes these flows as turbulent. Essentially, then, in seeking to understand the processes that characterize wall turbulence, we are seeking to explain its robustness. This is not to say that "turbulence is linear", but rather that the processes that drive turbulence and select structure do appear to have a strong linear flavor (as hinted at by previous studies). We deliberately confine nonlinear effects are confined to the determination of the mean velocity profile and a conservative nonlinearity. By thus doing, we are able to make significant progress by consideration of the linear (not **linearized**) Navier-Stokes operator. We approach the turbulent flow as a system, to give us information about how the system behaves as a whole, inclusive of the nonlinearity and with a view to making direct connections to experimental and numerical observations of wall turbulence. A further benefit of the systems paradigm advocated here is that closed-loop control thinking and technology will carry over in the future for control designs, offering the opportunity for sophisticated closed-loop strategies (effectively based on a perfect-system model), different from the open-loop "manipulation" that has been common in the literature.

The full nonlinear behavior of a turbulent flow is probably too complicated to model in a simple manner, because the interconnection between scales governed by the nonlinear term would require modeling all scales at once. One approach, then, is to pretend we know nothing of the nonlinear interactions between scales and concentrate on the part we can most easily analyze, the linearized system. However, in our case, the nonlinearity is not assumed away; instead, we treat it as an unstructured forcing that has already acted to support an (assumed) turbulent mean profile of the appropriate form. The resulting decomposition of the

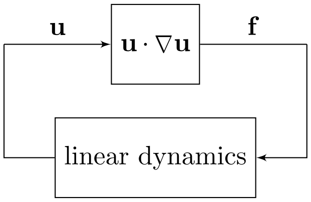

Figure 1: A high-level description of the turbulence process. The lower block contains the linear dynamics of the fluctuations interacting with the mean velocity profile.

NSE as a linear system driven by an unknown nonlinear term works because the linearized system is so selective that the exact form of the forcing is almost unimportant **under this formulation**.

In keeping with similar approaches as applied to other flows in the literature, we refer to our analysis as **resolvent analysis**. At the schematic level, this analysis, reported in detail in McKeon and Sharma [2010] and section 4, can be represented as in figure 2. It provides, first, an exact representation of the NSE in which the output from a linear sub-system at each wavenumber/frequency combination interacts with all others to provide forcing to all linear sub-systems. The operator in each linear sub-system, the resolvent, describes the transfer of energy into the turbulent fluctuations, along with one describing the sustenance of the mean profile that appears in all the resolvents. The inter-wavenumber energy transfer then follows from the nonlinear term as a consequence of gradients in energy distribution and triadic spectral interaction mechanisms. In this sense, the resolvent formulation serves as a road map for the energy transfer in wall turbulence, and captures key dynamical processes.

Such information makes possible theoretical extensions to the basic framework, in order to predict the influence of prescribed external inputs and to design forcing strategies for specific, application-optimized modification of turbulent spectra. Secondly, the formulation admits significant mathematical simplification associated with the low-rank nature of the resolvent, which can be exploited to enable conceptually and numerically simple interrogation, replication and extension of known results in wall turbulence, ranging from the statistical to structural.

Figure 2 shows the full schematic of the resolvent analysis, including the singular value decomposition of the resolvent, which constitutes a gain-based decomposition in the wall-normal direction. The first singular input (forcing) and output(response) modes have been the focus of our investigation because they capture many aspects of wall turbulence. The figure identifies other aspects of the analysis requiring additional study, namely the mechanisms for generating the mean velocity profile, $U(y)$, which is assumed from experimental data in the present analysis, and the required characteristics of the nonlinear term itself, which can be expressed in terms of determining the appropriate response mode amplitudes and phases contributing to nonlinear interactions. Both aspects require explicit treatment of nonlinearity, and resolution of both is required for the system to be self-sustaining, i.e. to fully capture the dynamics of wall turbulence. Preliminary steps towards both of these outstanding issues have been taken under this grant. Time-resolved particle image velocimetry (TRPIV) has been used to provide a first quantification of the three-dimensional (streamwise/spanwise wavenumber and temporal frequency) spectrum of the streamwise velocity throughout the turbulent boundary layer and to identify convection velocities associated with individual coherent vortical turbulent structures, and the so-called “2D/3C” (two-dimensional, three velocity component) model for the mean velocity profile has been extended from plane Couette flow to pipe (Hagen-Poiseuille) flow.

Note that the ability to interact with the resolvent model via external forcing of one transfer function, i.e. actuation at a single wavenumber/frequency combination, was introduced under AFOSR grant 9550-08-1-0049 *“Turbulent boundary layer response to perturbation by dynamically rough surfaces”* and is under continued exploration through a Basic Research Initiative grant 9550-12-1-0479 *“BRI Wall turbulence with designer properties: identification, characterization & manipulation of dominant energy pathways”*. The latter grant has also investigated the pressure signal associated with individual resolvent modes and means by which to implement linear control of the resolvent system using wall actuation.

The detailed outcomes from the present grant are summarized in sections 4-6. A summary of the key results is given below.

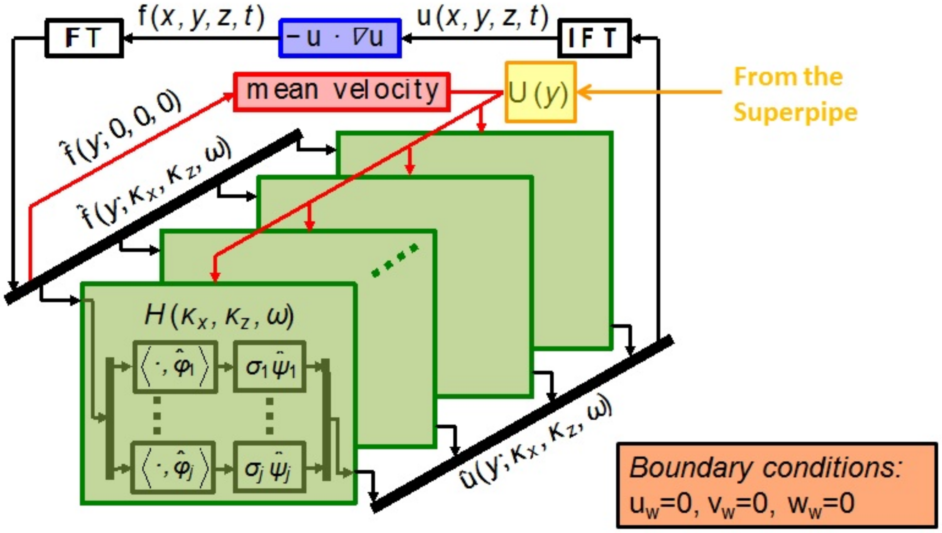

Figure 2: Resolvent analysis as an interconnected system of transfer functions, $\mathcal{H}(k_x, k_z, \omega)$. Each transfer function is decomposed into the most "dangerous", or most amplified directions using a singular value decomposition, such that input forcing, f is ranked at each wavenumber/frequency triplet based on gain (singular, value σ) and giving rise to output u.

2.2 Summary of results

2.2.1 Key features of wall turbulence captured by resolvent analysis

Our publications [McKeon and Sharma, 2010, Sharma and McKeon, 2013b, Moarref et al., 2013]have developed several aspects of wall turbulence that are captured, extended and/or explained using resolvent analysis. The key observations are summarized here.

Examination of the form of the first singular response modes (henceforth velocity response modes) reveals that these in isolation replicate the streak/roll form that is commonly observed in wall turbulence. Figure 3 shows the velocity structure associated with a wavenumber/frequency combination representative of the near-wall turbulence cycle, capturing the wall-normal extent known to be associated with this turbulent activity. The critical layer behavior revealed by the resolvent analysis ensures that this structure is observed at all scales, both attached to and detached from the wall (in the sense of whether the velocity footprint reaches the wall or not).

Examination of the swirling (vortical) motion associated with individual response modes led to the identification of a periodic array of prograde and retrograde hairpin vortices (with heads of both senses of rotation, where prograde indicates a sense aligned with the mean spanwise vorticity and retrograde indicates the opposite sense) associated with each mode attached to the wall. Whereas the velocity response modes can be linearly summed, the swirling diagnostic is nonlinear, and the mean velocity was shown to preferentially emphasize prograde vortices while suppressing retorgrade ones, in line with experimental observations. Further, linear addition of even three response modes at different wavenumber/frequency combinations (chosen to be triadically consistent, such that there is potential for the modes to self-excite through the nonlinear forcing term), leads to a complicated assembly of hairpin vortices, which we deemed "an ideal packet" with characteristics consistent with observed hairpin packets, see figure 4. The resolvent analysis allows a relatively simple origin of the complex "forests of hairpins" observed in high Reynolds number simulations of wall turbulence, as a linear assembly of velocity response modes giving rise to a nonlinear swirling field.

In subsequent work Moarref et al. [2013], geometrical self-similarity of the resolvent in the logarithmic region has been identified, giving rise to self-similar hierarchies of vortices as shown in figure 5. A paper on further

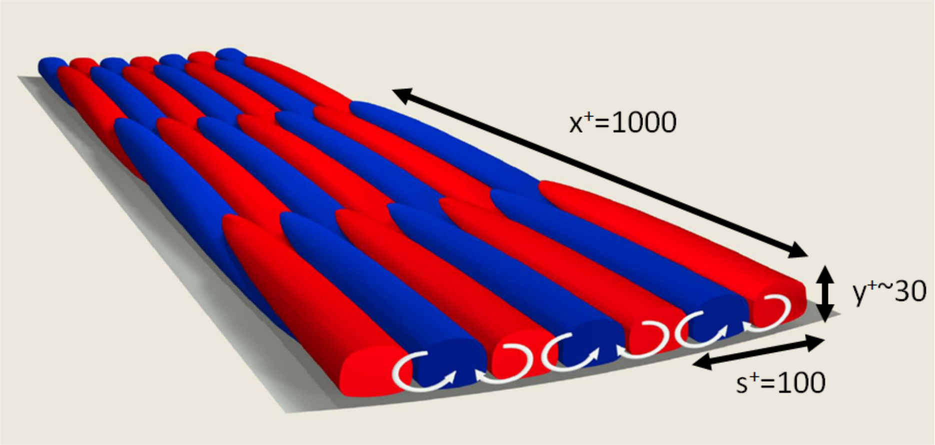
x^+=1000
y^+~30
s^+=100

Figure 3: Shape of the first singular mode representative of the dominant near wall motions. Color denotes isosurfaces of streamwise velocity (streaks), where red and blue correspond to high and low velocity respectively relative to the mean flow (heading into the page), and the white arrows show the sense of the in-plane velocity field.

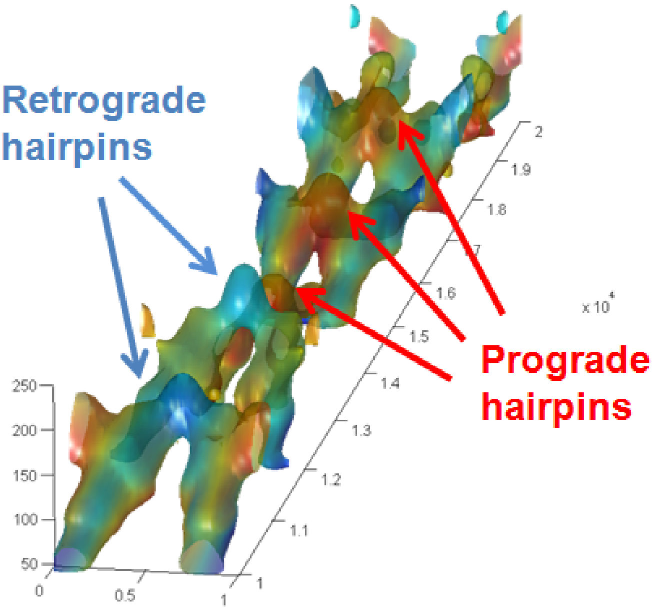
Retrograde hairpins
Prograde hairpins
250
200
150
100
50
0
0.5
1
1
1.1
1.2
1.3
1.4
1.5
1.6
7
1.8
1.9
2
x 10^4

Figure 4: Isosurfaces of constant swirling strength (33% of maximum value) for the "ideal packet" at $R^+ = 1800$, color-coded by the local (model) azimuthal vorticity. Red and blue denote rotation in and counter to the sense of the classical hairpin vortex or prograde and retrograde vortices, respectively.

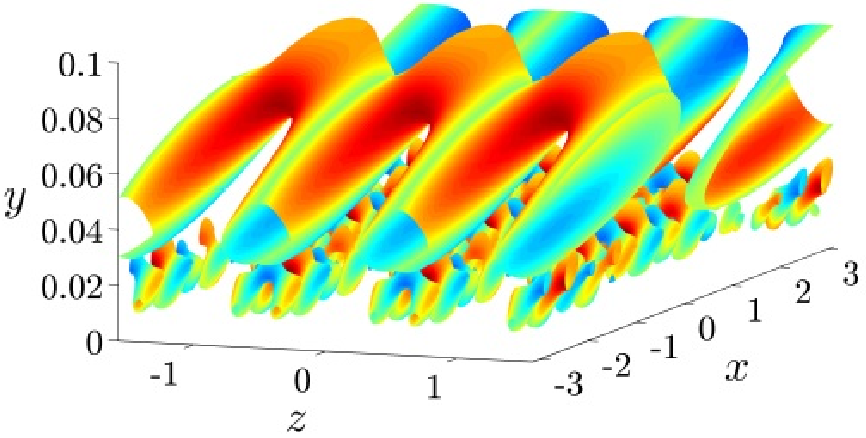

Figure 5: Eddy structure at two scales within a self-similar hierarchy identified using resolvent analysis.

developments associated with this self-similarity, specifically with regards to self-similar interaction between hierarchies forcing other hierarchies is currently under review, [Moarref et al., 2014b].

In Moarref et al. [2013], it was shown that self-similarity of the mean velocity profile, could be used to identify regions of self-similarity of the resolvent and forcing magnitudes, such that the variance of the velocity fluctuations could be modeled satisfactorily to high (atmospheric) Reynolds numbers. An example of the comparison between experimental/numerical results and the resolvent model for channel flow is shown in figure 6. In further work Moarref et al. [2014a], we have shown that the full velocity spectra can be well-matched (figure 7) by formulation of the appropriate optimization problem and using up to twelve resolvent modes at each wavenumber/frequency combination active in turbulence. This constitutes a model with less than 0.03% of the degrees of freedom of the full simulation on which the resolvent modes were projected. The agreement is excellent for the streamwise velocity, which dominates the energy norm used in the singular value decomposition of the resolvent, but work continues on the relatively weaker wall-normal velocity.

This work also supported the earlier observation [Bourguignon et al., 2014b] of sparsity in the frequency domain when DNS data was subjected to the three-dimensional (k, n, ω) Fourier transform. In a recent collaborative publication [Gómez Carrasco et al., 2014] we have shown that this sparsity is a real and significant feature of numerical simulations that is directly attributable to the spatial discretization employed. Figure 8 shows a comparison of the peak gain (amplification, singular value) over a range of azimuthal wavenumbers and temporal frequencies for the continuous case and in the presence of spatial discretization. The "peaky" structure of the discretized case, which is reflected as a sparsity in the frequency domain, suggests a further order reduction for future models.

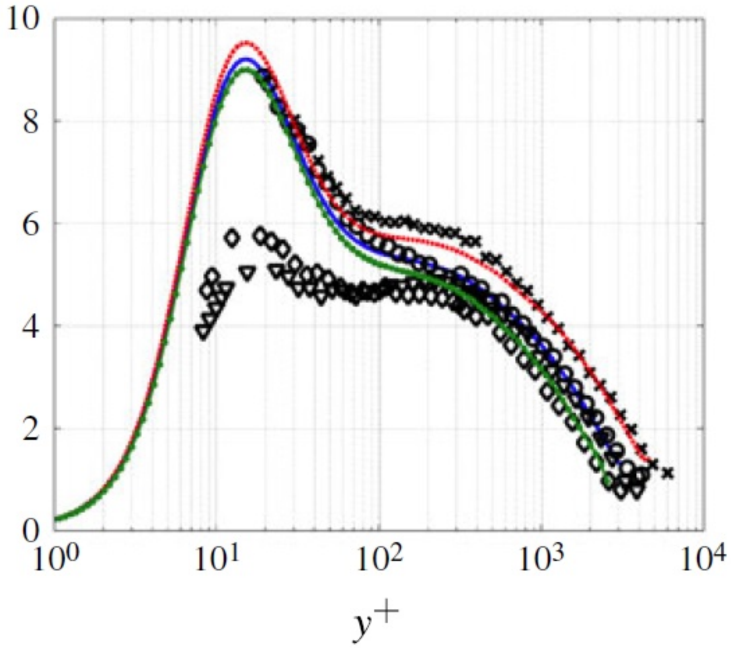

Figure 6: Comparison of experimental and resolvent model results for the streamwise energy intensity. Red, blue, green lines show model results at $Re_\tau = 3165, 4000, 5813$; symbols represent experimental results for $Re_\tau = 3165, 4000$ ($\diamond$, $\triangledown$) [Monty, 2005] and $Re_\tau = 4000, 6000$ ($\circ$, $\times$) [Schultz and Flack, 2013]. Note the influence of spatial averaging on the experimental profiles close to the wall, i.e. the disagreement between model and experiment appears to be dominated by experimental bias.

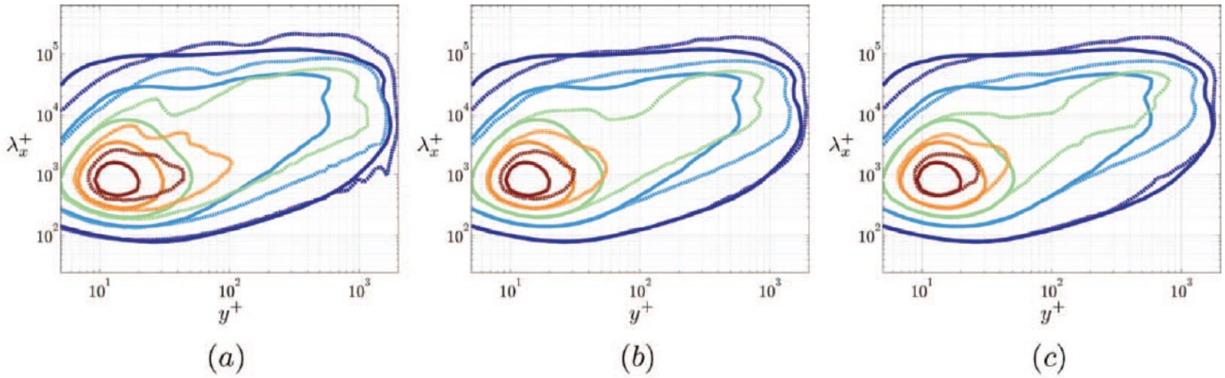

Figure 7: Time-averaged streamwise velocity spectra: from the DNS of Hoyas and Jimenez [2006] for $Re_\tau = 2003$ (solid lines), model-based spectra with the optimal weights using $N = 2, 6, 12$ (a-c) resolvent modes per wavenumber/frequency triplet and $0 < c < U_{cl}$. Contours show 10% to 90% of the maximum in the DNS data with increments of 20%.

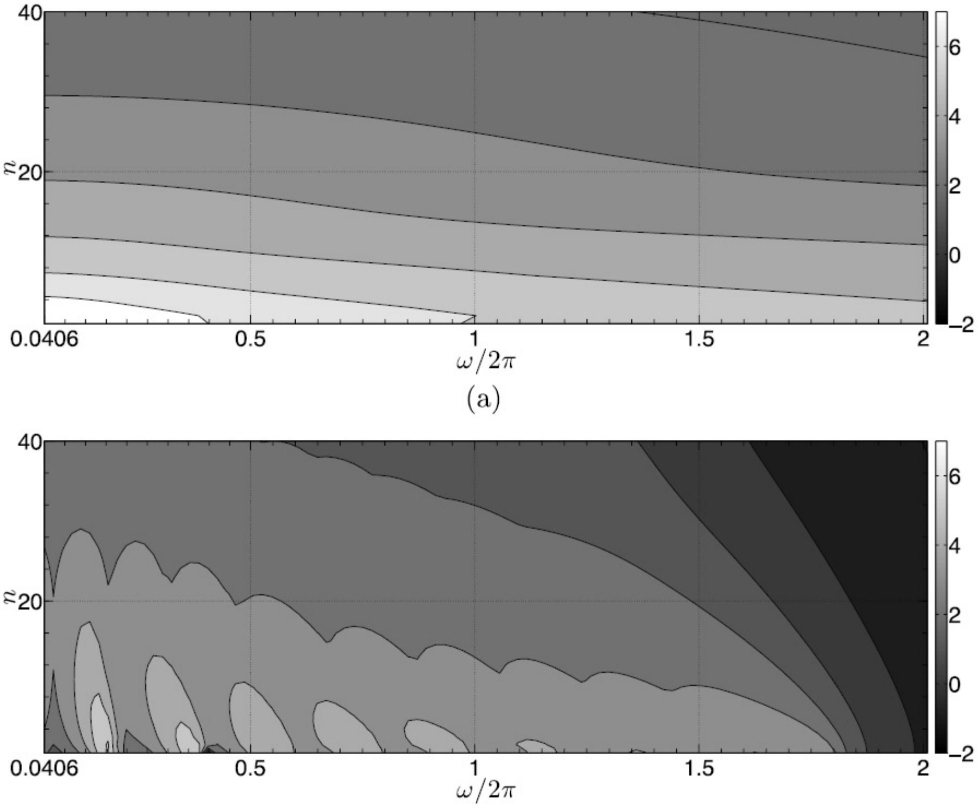

(a)

Figure 8: Distribution of resolvent amplification (singular value) in the energetically active subset of azimuthal wavenumbers n and frequencies $\omega/2\pi$ for the first singular vector at $Re_\tau = 314$. (a) One-dimensional resolvent model assuming continuum of wavenumbers available; (b) two-dimensional resolvent model incorporating spatial discretization adopted in DNS.

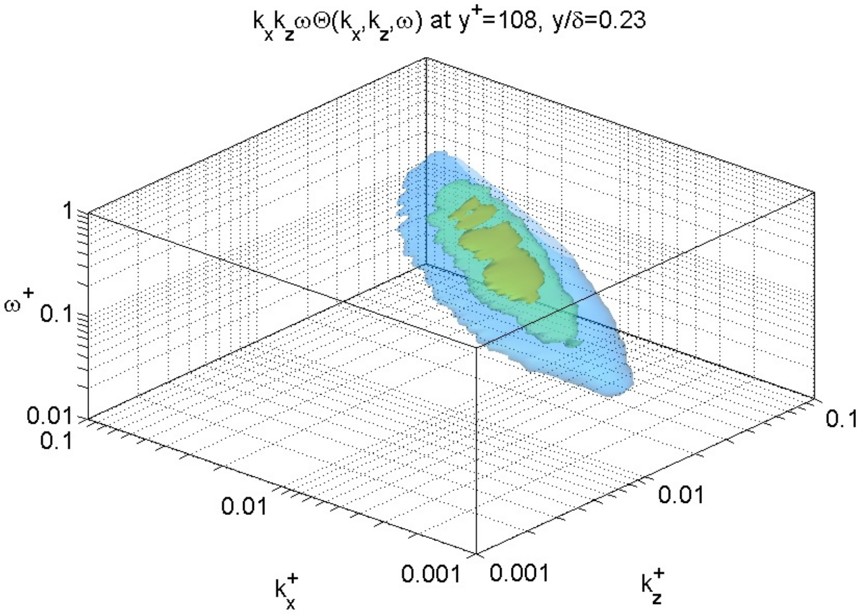

Figure 9: Premultiplied 3D spectrum of the streamwise velocity fluctuations in a turbulent boundary layer. Equal area within an isocontour corresponds to equal energy.

2.2.2 TRPIV characterization of the three-dimensional power spectrum of streamwise velocity fluctuations

The above description of resolvent analysis underscores the importance of understanding the distribution of turbulent energy in the three-dimensional wavenumber/frequency space, in order to provide targeted input. It is an interesting problem in its own right, since both experimental and numerical data are presented after integration in one or two of those dimensions: typical experimental diagnostics either implicitly average in one dimension (e.g. hot wires) or are used in a mode that averages over one dimension in order to reduce the amount of data storage required. One notable exception is the work of Morrison and Kronauer [1969] and Morrison et al. [1971], who obtained three-dimensional information in a wall-normal plane by an exhaustive study that involved changing the separation between two hot wires in order to obtain spatial information. A typical means to move between wavenumber and frequency space is Taylor's hypothesis of frozen turbulence, in which the local mean velocity is used as the convection velocity, such that $U(y) = \omega/k$, but there are known issues with this assumption, particularly for the large scale motions close to the wall. The response mode shapes illuminated by the resolvent analysis underscore the reason for these discrepancies, namely that the critical layers for the larger, attached scales lie far from the wall, while their footprints reach down close to the wall where the local velocity is much less than the correct convection velocity at the critical layer.

Under this grant, and published in two papers in Experiments in Fluids, LeHew et al. [2011] and LeHew et al. [2013], direct measurements of the fully time- and space-resolved velocity field in wall-parallel planes were obtained using a 5kHz, time-resolved PIV (TRPIV)system in a turbulent boundary layer developed over a flat plate in a water channel. This information was processed to obtain the full three-dimensional spectrum of the streamwise velocity fluctuations in regions corresponding, approximately, to the buffer, logarithmic and wake regions of the boundary layer. An example of a premultiplied three-dimensional spectrum obtained near the top of the logarithmic region is given in figure 9. The elongated shape in the $\omega - k$ plane indicates that Taylor's hypothesis is a good first order estimate this far from the wall; any asymmetries in the deviation from a straight line correspond to failures of the hypothesis in an average sense.

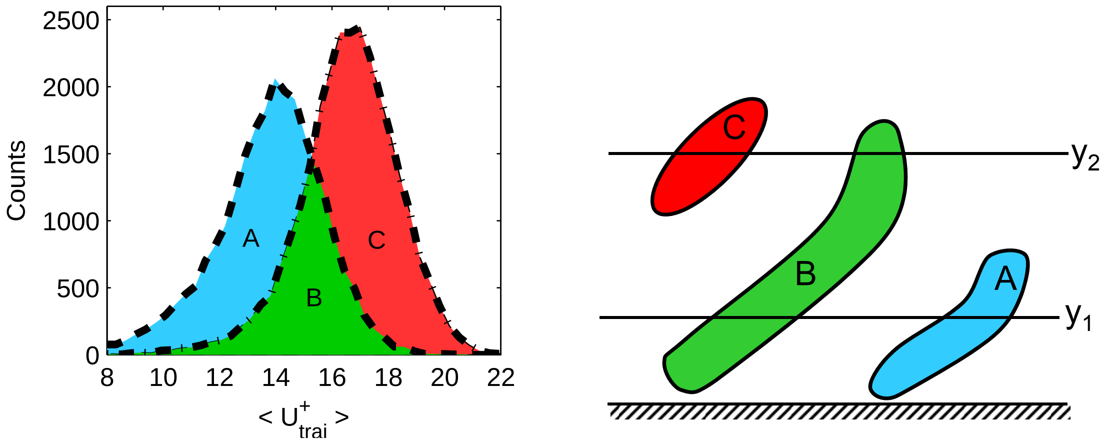

(a) Histogram comparison **(b)** Cartoon of inferred structures

Figure 10: (a) Comparison of convection velocity histograms at $y/\delta = 0.08$ and $y/\delta = 0.30$ leading to the identification of 3 distinct regions. The labeled regions are referenced in (b) showing the structure shapes inferred from the histograms in (a).

2.2.3 TRPIV tracking and characterization of individual turbulent structures and their convection velocities

The time-resolved PIV experiments above were also used to study coherent structures in wall-parallel planes, to track them and identify structure-specific trajectory and convection velocity statistics, and to propose a model for the types of structures observed by linking observations at different wall-normal heights. Figure 10a shows the convection velocity "signatures" of "swirling coherent structures" (SCS), which are identified by identifying swirling motion in the wall-parallel plane and are considered to be a proxy for coherent vortical motions with greater wall-normal extent. The left-most curve corresponds to the distribution of convection velocities observed in the buffer region measurement plane and the (overlapping) rightmost curve to the velocities in the wake region. Statistically, velocities that are populated in both planes are likely to correspond to tall structures with a signature in both planes, as shown in schematic in figure 10ab. The detailed observations in this work were shown to be consistent with Townsend's attached eddy hypothesis, as identified directly from experimental data.

2.2.4 Model for the mean velocity

In the resolvent analysis reported here, a mean velocity profile is required as input to the linear resolvent operator. Experimental data from the Princeton Superpipe McKeon et al. [2004] was used for pipe flow[McKeon and Sharma, 2010], and an eddy viscosity formulation for channel flow [Moarref et al., 2013]. Another model for the mean velocity was explored under this grant, namely an extension of earlier work concerning the development of the turbulent mean profile in Couette flow [Gayme et al., 2010] to pipe flow, Bourguignon and McKeon [2011]. The spirit of this investigation was to provide a rough starting condition for the resolvent analysis, knowing that the correct assembly of mean profile and resolvent modes would be self-sustaining, i.e. it would return the correct mode amplitudes and phases and mean velocity.

The so-called "2D/3C" model uses either a model streamfunction in the cross-stream plane or stochastic noise as input to the equation governing the streamwise-averaged velocity profile, and continues to return encouraging agreement with real mean velocity profiles. Figure 11 shows the mean velocity profiles (b) arising from the (v, w) forcing streamfunctions shown in (a). The agreement with DNS is promising, even for such simplified streamfunctions, indicating a degree of robustness of the mean velocity profile in addition to the turbulent velocities. In Bourguignon and McKeon [2011], stochastic forcing was also used in place of the simple streamfunctions and led to replication of several phenomena observed during pipe flow transition.

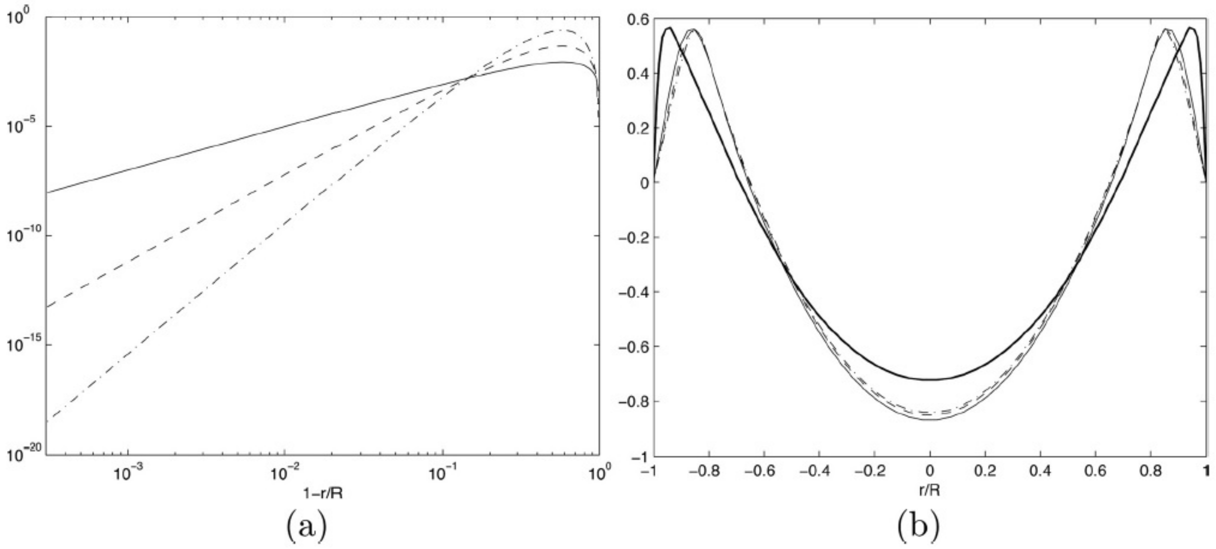

Figure 11: (a)Streamfunctions $\Psi_{1,a-c}(\eta)$ and (b) corresponding velocity profiles $u_0(\eta)$ for $\Psi_{1,a}(\eta) = 0.033(\eta - 3\eta^3 + 2\eta^4)$ (thin solid), $\Psi_{1,b}(\eta) = 0.7(\eta - 3\eta^3 + 2\eta^4)^2$ (dashed), and $\Psi_{1,c}(\eta) = 14(\eta - 3\eta^3 + 2\eta^4)^3$ (dash-dot) and experimental velocity profile of den Toonder and Nieuwstadt [1997] at $Re = 24600$ (thick solid).

Preliminary studies of the resolvent using approximate mean velocity profiles indicated a relative insensitivity to deviations from the real profile, with the exception of regions of high shear, i.e. close to the wall. As such, approximation of the mean velocity profile by a model such as the 2D/3C approach are likely to constitute a reasonable starting condition for a fully-closed resolvent analysis. Such a study, hopefully leading to a self-sustaining model of wall turbulence in due course, is reserved for future work, however the results under this grant provide a promising first step.

3 Background

A full review of the state of the art in wall turbulence was co-authored in 2011 Smits et al. [2011] under this grant. A brief background and literature review relevant to the work described later in the report is given below. Further background information can be obtained by reference to the associated archival journal papers.

3.1 A brief review of linear processes in wall turbulence

In recent years, dynamical systems approaches have had intriguing success in predicting the features of transition, particularly in (linearly stable) pipe flow [Kerswell, 2005], as reviewed by Eckhardt et al. [2007]. Our understanding of transition has also benefited from a model in which small disturbances develop over infinite or finite time horizons [Trefethen et al., 1993, Butler and Farrell, 1992a, Schmid and Henningson, 2001]. In the latter picture, the system is explored by investigating the properties of the linearized Navier-Stokes system, via either its linear stability (eigenvalues) or more recently by a transient growth analysis (which investigates perturbation growth on a finite instead of infinite time horizon). These analyses are linear in nature, though often they go on to consider secondary instabilities arising from the nonlinearity.

One problem with applying perturbation analysis to turbulence is the selection of an appropriate base flow around which to linearize, since the turbulent mean velocity profile does not constitute a solution of the Navier-Stokes equations (NSE) and the transport due to turbulent fluctuations must be treated explicitly. However there have been notable efforts to extend this analysis to characterize stability and transient growth in turbulence, including the work of Butler and Farrell [1992b], del Álamo and Jiménez [2006], Cossu et al. [2009] and Hwang and Cossu [2010], who used a turbulent eddy viscosity to circumvent the closure problem. The use of transient growth methodology in transitional flows is certainly well-motivated. However, despite some informative results, particularly with respect to the match between the most amplified spanwise scales (occurring for streamwise-constant disturbances) and experimental observations [del Álamo and Jiménez, 2006, Hwang and Cossu, 2010], the analysis of infinitesimal perturbations growing in finite time in a system where nonlinear feedback is so prevalent struck us as problematic and motivated the desire to look beyond the time-domain behaviors of unforced perturbations. Turbulent flows experience very large instantaneous deviations from any known fixed point solution and the largest growing initial condition under some time horizon will surely itself be perturbed before it reaches maturity. We suggest that things look simpler in the frequency domain.

Important steps were made in this direction by, among others, Bamieh and Dahleh [2001] and Jovanovic and co-authors [Jovanovic and Bamieh, 2003, 2005]. There is a link, via the pseudospectrum, between the non-normality investigated in the transient growth body of work and the resolvent norm, which we will describe further in what follows [Schmid and Henningson, 2001, Trefethen et al., 1993, McKeon and Sharma, 2010]. Those studies of the non-normality of the linearized Navier-Stokes operator, however, did not go so far as to develop a full, self-consistent approach to wall-bounded turbulence, in the sense that links to experimental observations were not made and the connection with the omitted nonlinear terms was not established. The resolvent analysis that formed a central part of the work performed under this grant seeks to fill this gap.

Linear models of pipe flow, e.g., Schmid and Henningson [2001] have been found to capture general characteristics of the coherent structures present in turbulent flow but are unable to reproduce the change in mean flow associated with transition to turbulence. Linear studies have shown that linear non-normality in subcritical shear flows is required to sustain turbulence [Henningson and Reddy, 1994] and so are the terms linear in turbulence fluctuations [Lim and Kim, 2004]. The non-normality of the linear Navier-Stokes (LNS) operator results in large amplification of disturbances and transient growth of initial perturbations. However, the growth of the most amplified structures modify the mean flow in a way that reduces the amplification potential, i.e., the non-normality. Hence, realistic models for pipe flow transition must include mechanisms leading to a change in mean flow as the perturbations develop.

Since the blunting of the velocity profile is accurately captured by the full Navier-Stokes equations (NSE), a convenient approach is to go back to the NSE and invoke simplifying assumptions in order to reduce the complexity of the model instead of starting from the LNS and adding some sort of nonlinearity. Streamwise-constant models describe the evolution of the three components of velocity in a plane perpendicular to the mean flow and are equivalently referred to as 2D/3C. A streamwise-constant model for fully developed (pipe) flow was derived by Joseph and Tao [1963] and shown to be globally stable for all Reynolds numbers. Thus, the 2D/3C model has the useful property of having a unique fixed point corresponding to the laminar flow. A stochastically forced 2D/3C model formulated in terms of a cross-stream stream- function and the deviation of the streamwise velocity from the (linear) laminar profile was used by Gayme et al. [2010] to study Couette flow and successfully captured both the blunting of the velocity profile and structures similar to the streamwise-elongated vortices and streaks observed in experiments. In general terms, the stochastically forced 2D/3C model exploits the large amplification of background disturbances due to the non-normality of the linearized operator described by Farrell and Ioannou [1998] which has been shown to reach a maximum for streamwise-constant disturbances [Bamieh and Dahleh, 2001]. The latter authors showed that streamwise-constant disturbances are amplified proportionally to Re^3 vs. $Re^{3/2}$ for streamwise-variant disturbances. In addition, Jovanovic and Bamieh [2005] demonstrated that the largest amplification is only obtained by forcing in the plane perpendicular to the mean flow and is observed in the streamwise velocity component.

Pipe flow is well suited for an assumption of streamwise invariance since streamwise-elongated coherent structures have been shown to play an important role during transition as well as in fully developed turbulence, e.g., Eckhardt et al. [2007], Kim and Adrian [1999], Morrison et al. [2004]. The streamwise-elongated coherent structures in pipe flow, both in the near-wall region and further from the wall, take a form dominated by quasi-streamwise vortices and streaks of streamwise velocity. A body of recent work in the literature suggests a connection between these features and studies of the LNS. For example, the most (temporally) amplified mode of the LNS, based on an energy norm, is streamwise-constant with an azimuthal wavenumber $n = 1$ and features a pair of counter-rotating vortices which create streaks by convecting streamwise momentum [Schmid and Henningson, 2001].

Traditionally, the later stages of transition to turbulence in pipe flow have been characterized by the creation of puffs and slugs [Wygnanski and Champagne, 1973]. Puffs have been identified as the flow response to large amplitude disturbances at low Reynolds number, e.g., $Re \sim 2000$, and are characterized by a sharp trailing edge and a smooth leading edge whereas slugs are created by low amplitude disturbances at larger Reynolds number, $Re > 3000$ and have sharp leading and trailing edges.

3.2 Structure of the turbulent boundary layer

The current understanding of the structural and statistical nature of the turbulent boundary layer over a large range of Reynolds number rests primarily upon spatial information from direct numerical simulations (DNS) and particle image velocimetry (PIV) experiments, and temporal information from experimental measurements at a single point, yet there is a lack of simultaneous temporal and spatial measurements to describe the time evolution of the structures and statistics of the flow. While temporal information can be extracted from DNS data, not only is the range of Reynolds numbers limited, but the computational resources required to analyze a time resolved flow over a sufficiently long time period would be enormous. Similarly, in experiments, most commonly used instruments, such as hot wire anemometers, only provide temporal information at a single point, where the recovery of spatial information requires the arduous task of taking measurements at two or more points simultaneously over a range of separations. Planar PIV measurements provide a 2D spatial representation of the flow, and with a sufficiently high frame rate, as shall be discussed, provide simultaneous spatial and temporal measurements allowing a statistical and structural analysis of the turbulent boundary layer over two spatial dimensions and time.

Often, when either the spatial or temporal information is not acquired, a conversion between the two is performed using Taylor's frozen turbulence hypothesis [Taylor, 1938] which states that the spatial field can be reconstructed from the temporal field if the convection velocities of the individual eddies or scales which compose the flow are known. This conversion is performed assuming the eddies are "frozen", or in other words, that their shape does not evolve significantly over the distance projected. While the convection velocity of all such eddies is usually assumed to be equal to the local mean velocity, many studies have shown that this is not always a valid assumption [Morrison and Kronauer, 1969, Kim and Hussain, 1993, Krogstad et al., 1998, Chung and McKeon, 2010, del Álamo and Jiménez, 2009, LeHew et al., 2010]. A recent example of the importance of knowing the correct conversion was demonstrated by Monty and Chong [2009] who compare channel flow computations and experiments under the same conditions using the spatial spectrum from computations and the converted temporal spectrum from experiments. The discrepancies between the spatial and temporal spectra were put into better agreement using a scale dependent convection velocity near the wall. In the PIV measurements performed under this grant, information was recorded in both time and space, so no conversion was necessary, and it was possible to test the validity of Taylor's hypothesis at all measurement locations.

The use of time-resolved PIV to address the need for both spatial and temporal measurements in the turbulent boundary layer was first considered by Dennis and Nickels [2008] at a wall normal location of $y/\delta = 0.16$, where δ is the boundary layer thickness. It was concluded that at this particular wall normal location with a 6δ streamwise field of view, Taylor's hypothesis holds, although deviation was noted between the actual and projected velocity fields at distances beyond 4δ downstream. Based on the works cited previously, a more notable deviation would likely appear with measurements both very near and far from the wall, which will be addressed in the current study over a larger spatial field and considering the entire (k_x, k_z, ω) domain.

Although the use of PIV for simultaneous spatial and temporal measurements of a turbulent boundary layer is promising, there are a number of issues to be addressed. First, the resolution of the spatial fluctuations of the flow, and thus the resolution of the spatial spectrum, is limited by the interrogation window size which attenuates small scale fluctuations on the order of the window size as noted by Willert and Gharib [1991]. A technique to determine the optimal window size, considering both the attenuation from the interrogation window and the noise introduced by the PIV algorithm, was proposed by Foucaut et al. [2004]. An outline of all of the effects of PIV on the spatial spectrum including methods for avoiding spectral leakage and aliasing in space is presented by Tomkins and Adrian [2005]. The study of the space-time correlation in hot and cold jet flows by Wernet [2007] discusses the need for oversampling and low pass filtering in time to avoid temporal aliasing of PIV data. Finally, not only should the smallest energetic scales in the flow be recovered, but also the largest scales found to extend up to 14 times the pipe radius in experiments by Kim and Adrian [1999]. For boundary layer measurements, both the large scale motions (LSMs) with an energetic peak at $\lambda_x = 2 - 3\delta$ and the superstructures, with an energetic peak at $\lambda_x = 6\delta$ as discussed by Hutchins and Marusic [2007], Monty et al. [2009], and Guala et al. [2010], where λ_x is the streamwise wavelength, must be resolved. As discussed by Balakumar and Adrian [2007], streamwise scales longer than 3δ at all wall normal locations and Reynolds numbers considered contain at least 45% of the turbulent kinetic energy in the zero pressure gradient boundary layer. In addition, Ganapathisubramani et al. [2003] found that hairpin packets of comparable streamwise extent contain a significant amount of Reynolds stress, $-\overline{uv}$, and thus these large scales must be resolved to accurately represent the flow. As noted by Monty et al. [2009], while the 6δ superstructure peak becomes almost undiscernable outside the log layer, near the wall this peak is prominent and structures of this size and even larger must be resolved to fully encompass the near wall energy and dynamics.

The visualization and characterization of coherent structures, "organized motions that are persistent in time and space and contribute significantly to the transport of heat, mass, and momentum" [Marusic et al., 2010], in turbulent flows is a powerful tool for unwrapping the complicated dynamics involved in the production and sustenance of turbulence. The streaky structures observed in the hydrogen-bubble visualizations of Kline et al. [1967b] in the turbulent boundary layer, later captured in simulations by Kim et al. [1987], led to the identification of the autonomous near-wall cycle analyzed by Jiménez and Pinelli [1999] as well as Jeong and Hussain [1995] and Schoppa and Hussain [2002], recognized as the major producer of turbulent kinetic energy near the wall. The dynamics of turbulence further from the wall are often associated with the hairpin vortex proposed by Theodorsen [1952] and studied in the smoke visualizations of Head and Bandyopadhyay [1981]. A comprehensive review of the hairpin packet paradigm is given by Adrian [2007]. The literature describing coherent structure is broad, and we review only the papers most relevant to the current study here.

The advent of direct numerical simulation (DNS) and experimental techniques such as particle image velocimetry (PIV) have allowed not only a qualitative, but also a quantitative measure of the flow field associated with these coherent structures. Adrian et al. [2000] found that hairpin vortices tend to form into streamwise aligned packets using PIV in wall-normal planes, and later, Tomkins and Adrian [2003] analyzed these structures in wall-parallel planes. Work by Ganapathisubramani et al. [2003] showed that not only were hairpin packet structures prevalent in the flow, but they also produced significant amounts of Reynolds stress, and were thus linked with the production of turbulence.

In depth analysis of the size and organization of these hairpin vortices was performed by Carlier and Stanislas [2005] using planar 2D2C (two-dimensional velocity field with two in-plane components of velocity) PIV in wall-normal, wall-parallel, and upstream- and downstream-tilted (135° and 45° to the free-stream, respectively) cross-stream planes and stereo-PIV in a vertical cross-stream plane of the turbulent boundary layer over a range $Re_\theta = 7500$–19000, where $Re_\theta = \theta U_\infty / \nu$ is the momentum thickness Reynolds number, θ is the momentum thickness, U_∞ is the free-stream velocity, and ν is the kinematic viscosity. It was found that vortices have a radius ranging from 20–30 δ_ν and that their properties scale universally in inner units in the log region for moderate Reynolds number flows, where $\delta_\nu = \nu / u_\tau$ is the viscous length scale and $u_\tau = \sqrt{\tau_w / \rho}$ is the friction velocity where τ_w is the shear stress at the wall and ρ is the fluid density. Additionally, stereo-PIV measurements from the same authors indicated that vortex structures identified in the cross-stream plane travel near the local mean velocity on average.

Hutchins et al. [2005] also performed stereo-PIV measurements in upstream and downstream tilted planes, 135° and 45° to the free-stream, respectively. In the upstream tilted plane, trains of counter rotating vortex structures were found where the orientation of pairs producing an ejection was preferred, consistent with the hairpin packets proposed by Adrian et al. [2000]. Furthermore, the spacing of vortex pairs scaled in outer units and, using the streamwise velocity correlation coefficient, structures were inferred to uncouple or detach from the wall once they grew beyond the log-layer, and thus the detachment point scaled in outer units as well. Finally, the dual-plane stereo PIV experiments of Ganapathisubramani et al. [2006] helped to elucidate the orientation of vortex structures by obtaining the complete vorticity vector. These measurements verified that the most frequently observed vortex inclination angle ranged from 42° to 46°, showing the predominance of forward or downstream-leaning vortices near the wall with a Λ shaped vortex being the preferred representation, and demonstrated that the density of backward leaning cores is nearly constant with y, while the number of forward leaning cores decreases with y.

While much progress has been made by obtaining static spatial footprints of coherent structures in the turbulent boundary layer, there has been little study of the evolution of these coherent structures in time. This is difficult experimentally due to the need for a full-field velocity measurement in a large field of view, along with fine temporal resolution; usually only one of the two is possible with a given experimental technique. While temporal resolution may not be an issue in DNS, the memory requirements to store a significantly long time history to track coherent structures and recover a statistically significant measure would be large.

Many researchers have identified vortical structures or their signature in the Reynolds stress in direct numerical simulations and explored the relationships between them, e.g. Jiménez and co-workers, del Álamo et al. [2006], Lozano-Duran et al. [2012], albeit constrained to spatial averaging rather than temporal tracking. Here we focus on temporally-resolved measurements, which are predominantly experimental at present.

One alternative to the stringent resolution and field of view requirements in experiment is to acquire two- or three-velocity-component, two-dimensional fields and extrapolate into three dimensions. In order to better understand the 3D structure and evolution of vortex structures, Dennis and Nickels [2011b] and Dennis and Nickels [2011a] used stereo PIV in the cross-stream plane of a turbulent boundary layer to obtain “pseudo-3D” velocity fields and reconstruct the spatial development of hairpin vortices and large-scale coherent structure using Taylor’s hypothesis. This hypothesis is known to be accurate over a large portion of the boundary layer, thus providing a fairly accurate representation of the 3D structure. By conditioning the velocity field on a swirl threshold at a particular height, the ensemble relationship between structures was developed.

Recent time-resolved tomographic PIV measurements in a $1.8 \times 1.8 \times 0.19\ \delta$ (streamwise, spanwise, wall-normal) field of view by Elsinga and Marusic [2010] have satisfied both the spatial and temporal resolution requirement and allowed the measurement of the average lifetime of coherent structures, which they measure to be $14.3\delta/U_\infty$ based on the period of oscillation between the four basic flow topologies (inferred from the invariants of the local velocity gradient tensor; see Chong et al. [1990]), where δ is the boundary layer thickness. Using the same data set, Elsinga et al. [2012] were also able to track vortex structures in time, and observed non-negligible wall-normal displacement of the structures during a typical trajectory.

4 Critical layer framework

In this section, a review of the critical layer/resolvent framework results obtained under this grant is given. This encompasses material published in three papers in the Journal of Fluid Mechanics [McKeon and Sharma, 2010, Sharma and McKeon, 2013b, Moarref et al., 2013]. The initial discussion closely follows the set up in the (invited) Physics of Fluids review paper McKeon et al. [2013]. The origins of this analysis partly lie in nonlinear robust control theory, but a differentiating feature is the connection with, and prediction of, state-of-the-art understanding of velocity statistics and coherent structures observed in real, high Reynolds number flows.

4.1 Turbulence as a directional amplifier

The full analysis described in McKeon and Sharma [2010] was performed for pipe flow primarily because of the geometrical simplicity, the availability of high Reynolds number experimental data for comparison of statistical results [McKeon et al., 2004, Morrison et al., 2004] and the potential for extrapolation to other canonical flows. Turbulent flow through pipes is, of course, important for the transport of fluids such as oil and natural gas, numerous natural and biomedical applications, and is also highly relevant to the study of other canonical flows. Transition to turbulence in a pipe is still not completely understood Hof et al. [2010], but the pipe offers the analytical benefits of statistical homogeneity in the streamwise direction and a simple constraint on the azimuthal wavenumber. The coordinate system in a long, straight pipe of circular cross-subsection for the following analysis is shown in figure 12.

The conceptual picture underlying our analysis is that of a nonlinearity "feeding back" to excite the linear wave propagation dynamics, which in turn drive the nonlinearity. As such, we concentrate on the linear amplification aspect of the turbulent process and examine the corresponding linear transfer function, considering its action at each wavenumber/frequency combination (described below), which is shown to provide highly-directional amplification. This picture is closely related to, but distinct from, the sector-bounding analysis of the NSE for control [Sharma et al., 2011] and model reduction [Sharma, 2009].

A full solution of the NSE would predict the turbulent mean velocity profile. However, a significant restriction on the scope of our modeling efforts is obtained by assuming the mean profile is known and concentrating on the action of the resolvent operators in which it appears. With the particular choice of pipe flow, experimental measurements from the Princeton Superpipe are available up to conditions representative of high Reynolds number applications [McKeon et al., 2004] and the use of a turbulent eddy viscosity can be avoided.

Pipe flow affords the simplification of a priori knowledge that the optimal bases for modeling the flow field in the homogeneous directions are the eigenmodes, which are the Fourier modes, such that the flow can be represented as a summation of finite-amplitude traveling wave fluctuations over a range of two-dimensional spatial wavenumbers and temporal frequencies about the turbulent mean profile, with a natural connection to the gain analysis described previously. Another obvious attraction of Fourier decomposition is the direct connection to the spectral measurements typically made in real flows. At its heart, the analysis that follows seeks to establish the optimal basis for decomposition in the inhomogeneous wall-normal direction, or the radial coherence associated with particular traveling waves. The analysis has been compared to proper orthogonal decomposition, which is a well-known technique for decomposing velocity field data to optimally capture the energy. While there is a superficial correspondence, our analysis differs in that the decomposition is predictive, since it is applied to the NSE and not pre-existing data.

4.1.1 Formulation for the analysis

Our analysis begins with the non-dimensional NSE for fully-developed, incompressible pipe,

$$\partial_t \tilde{\mathbf{u}} = -\nabla p - \tilde{\mathbf{u}} \cdot \nabla \tilde{\mathbf{u}} + Re^{-1} \nabla^2 \tilde{\mathbf{u}}, \quad \nabla \cdot \tilde{\mathbf{u}} = 0 \tag{1}$$

We retain the boundary layer terminology by fixing $y = 1 - r$, and u, $v(= -v')$ and w as corresponding to the streamwise, wall-normal and azimuthal velocities such that $\tilde{\mathbf{u}} = (v', w, u)$, as shown in figure 12. The

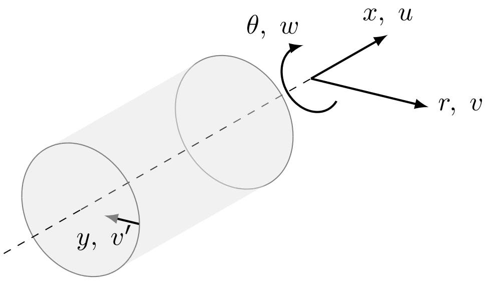

Figure 12: A schematic of pipe geometry and nomenclature.

Reynolds number is defined as

$$Re = \frac{U_{\text{bulk}} D}{\nu},$$

where ν is a constant viscosity, D the pipe diameter (equal to $2R$) and the bulk, volume-averaged velocity is U_{bulk}. We also introduce the Karman number,

$$R^{+} = \frac{D u_{\tau}}{2\nu}.$$

Here, $u_{\tau} = \sqrt{\tau_w/\rho}$ is the friction velocity, τ_w is the mean wall shear stress and ρ is the density.

The NSE are invariant under translation in t (time), x and θ. In view of these symmetries, we Fourier transform in time and the two homogeneous spatial directions, introducing for convenience the wavenumber/wavespeed triplet $K = (k, n, c)$ with $k = k'R$, $n = n'R$ and wavespeed $c = \omega/k$, with $\omega = \omega' R / \mathbf{u}_0|_{y^+=R^+}$ (where the prime denotes the dimensional variables and $\mathbf{u}_0|_{y^+=R^+}$ is the centerline velocity), and let $K \cdot \mathbf{x} = kx + n\theta - \omega t$ (notationally convenient). In addition, we specially define K_0 as $(k, n, \omega) = (0, 0, 0)$ and note that $\mathbf{u}_{K_0}$ ($\mathbf{u}_0$) is the turbulent velocity field averaged over space and time. Thus K with all positive elements refers to a downstream traveling wave (helical in the cylindrical pipe geometry). As yet, only the wall-normal direction remains untransformed; the problem is to find a suitable basis for these functions of r. The velocity field (and forcing field) is expressed as a sum of harmonic, radially varying traveling waves.

$$\mathbf{u}(r, x, \theta, t) = \sum_n \int_{-\infty}^{\infty} \int_{-\infty}^{\infty} \mathbf{u}_K(r) e^{iK\cdot\mathbf{x}} \mathrm{d}k \mathrm{d}\omega \tag{2}$$

We define $\mathbf{u}$ and $\mathbf{f}$ as

$$\mathbf{u} = \tilde{\mathbf{u}} - \mathbf{u}_0 \tag{3}$$

$$\mathbf{f} = -\mathbf{u} \cdot \nabla \mathbf{u} \tag{4}$$

with $\mathbf{u}_K(r)$ and $\mathbf{f}_K(r)$ the (radially varying) Fourier coefficients thereof.

The NSE assuming fully developed flow (i.e. real elements of K) can then be written in a divergence-free basis as

$$-i\omega \mathbf{u}_K = \mathcal{L}_K \mathbf{u}_K + \mathbf{f}_K, \quad (k, n, \omega) \neq (0, 0, 0) \tag{5}$$

$$0 = \mathbf{f}_0 - \mathbf{u}_0 \cdot \nabla \mathbf{u}_0 + Re^{-1} \nabla^2 \mathbf{u}_0 \tag{6}$$

Note that in this formulation, the linearized Navier-Stokes operator, $\mathcal{L}_K$, naturally involves the turbulent mean; yet we have performed no (linearized) stability analysis around a fixed point. Thus the $\mathbf{u}_K$s are exactly the Fourier coefficients of the turbulent fluctuations relative to the mean profile at all y. Previous work concerning analysis of $\mathcal{L}_K$ and globally optimal perturbations has typically employed a turbulent viscosity to account for the turbulent transport that would be excluded by a linearization procedure. In this analysis, the treatment of $\mathbf{f}$ explicitly accounts for this phenomenon, so the resolvent contains only the turbulent mean velocity profile itself.

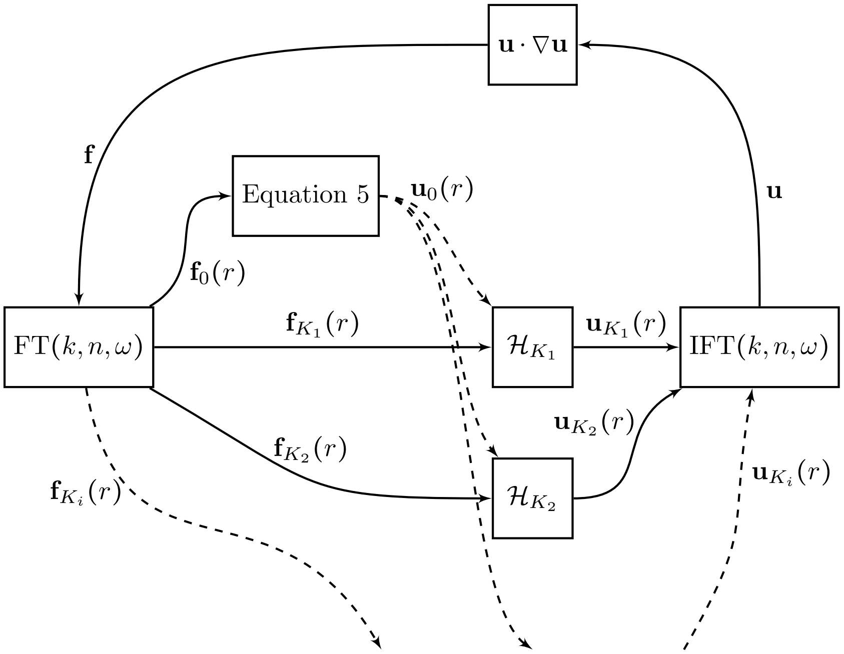

Figure 13: A block diagram showing the network of resolvents, $\mathcal{H}_K$, acting on radially-varying traveling waves of different wavenumber and frequency. An input-output relationship can be written for all K, but $\mathbf{u}_K \neq 0$ for a finite range of K in real flows. FT and IFT denote the Fourier transform and inverse Fourier transform, respectively. u_0 and f_0 describe the equation for the turbulent mean profile.

A trivial manipulation of equation 5 gives the response of the flow at a particular wavenumber combination subjected to harmonic forcing $\mathbf{f}_K$ arising from the interaction between other wavenumbers,

$$\mathbf{u}_K = \mathcal{H}_K \mathbf{f}_K = (-i\omega I - \mathcal{L}_K)^{-1}\mathbf{f}_K, \tag{7}$$

where $\mathcal{H}_K$ is known in the literature as the resolvent [Schmid, 2007]. Using the form for $\mathcal{L}_K$ given in Meseguer and Trefethen [2003], we can write

$$\mathcal{H}_K = \begin{bmatrix} i(k\mathbf{u}_0 - \omega) - Re^{-1}D & -2inr^{-2}Re^{-1} & 0 \\ 2inr^{-2}Re^{-1} & i(k\mathbf{u}_0 - \omega) - Re^{-1}D & 0 \\ -\partial_r \mathbf{u}_0 & 0 & i(k\mathbf{u}_0 - \omega) - Re^{-1}(D + r^{-2}) \end{bmatrix}^{-1} \tag{8}$$

with $D = \partial_r^2 + r^{-1}\partial_r - r^{-2}(n^2+1) - k^2$, and the states being the radial, azimuthal and axial velocities expressed in a divergence-free basis. Thus equations 5 and 6 can be visualized as the block diagram in figure 13, forming a complete representation of the NSE in this basis. The resolvents, $\mathcal{H}_K$, can be derived from the NSE and are interconnected through the nonlinear terms. Note that (as stated in the caption) while an input-output relationship can be written for all K, $\mathbf{u}_K \neq 0$ for a finite range of K in real flows.

Although the resolvents are *linear*, the nonlinear forcing internal to the system is explicitly retained so this is not a *linearized* analysis. Additional effects of the nonlinearity are bound up in the use of the turbulent mean velocity profile in the resolvent. Thus the analysis is fundamentally different from linear stability analysis: it concerns the response of a forced system (in reality lightly forced because the leading singular values in general give rise to large amplification), where the forcing is required to sustain a response in a linearly stable system. Thus, concepts relevant to the study of disturbances in inviscid, linearized laminar flow can be extended to the turbulent case, with the understanding that in the latter case the waves are lightly damped and would asymptotically decay in the absence of forcing $\mathbf{f}$.

Figure 13 describes an interconnected series of linear sub-systems with resolvents of known form. Thus the formulation of equations 5 and 6 lends itself naturally to separate analysis of the individual sub-systems

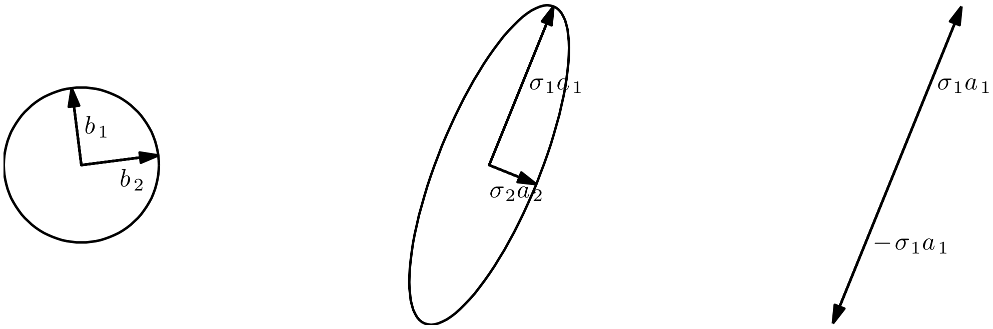

Figure 14: An illustration of the effect of matrix $\mathbf{M}$ on the unit circle (left plot mapped to centre plot). The singular values are the radii of the resulting ellipse and the singular vectors give the rotation of the ellipse. $\mathbf{a}_i$ are the columns of $\mathbf{A}$ and $\mathbf{b}_i$ are the columns of $\mathbf{B}$. The rightmost plot shows the effect of the optimal rank-1 approximation $\tilde{\mathbf{M}}$ to the mapping $\mathbf{M}$ on the unit circle.

associated with each K, under the constraint that the correct amplitudes for each $\mathbf{u}_K$ are required to sustain the (assumed) mean velocity profile in the fully-connected system. Without satisfying this constraint associated with the excitation of all $\mathbf{u}_K$ through the nonlinear term, progress can still be made in terms of determining the radial distributions of velocity for each K, since the linearity of the system allows for simple amplitude scaling of the response mode shapes. In effect, then, we can consider unstructured (unit) forcing of each sub-system, in knowledge that the output response modes can be linearly superposed to return to a representation of the full velocity field subject to the constraint that the response mode amplitudes must ultimately satisfy figure 13. This is another significant advantage of our approach: the ability to dissect the flow into manageable "lumps" (linear sub-systems) that can be analyzed in isolation and then simply reassembled. Further, this formulation proves amenable to approximation of the resolvent at each K that leads to a significant reduction in complexity using standard linear systems techniques.

4.1.2 Optimal low-rank approximation of the resolvent for inhomogeneous coordinates

The symmetries associated with the pipe geometry imply that the resolvent is normal under the integrals over the wall-parallel coordinates and time (see Sharma and McKeon [2013a] for further discussion on this point). In these homogeneous directions, then, the forcing and response modes are equal, orthogonal and are the Fourier modes, which then represent the appropriate choice for basis functions. However, this is not true in the wall-normal direction: the presence of the wall leads to the loss of symmetry with the implication that the forcing and response modes are no longer equal and the fluctuations may now gain energy from the interaction with the mean flow. The potential for momentum production due to this interaction is quantified by this loss of orthogonality. Since the resolvent is not normal with respect to the integral in this direction, the Fourier basis is no longer the optimal choice under the energy norm. We seek a basis that is optimal with respect to the magnitude of response to forcing in order to continue our gain-based analysis. To find this basis, we use the SVD. For the reader less familiar with the SVD, we give a brief example of its underlying action and interpretation in the next two paragraphs which the more accustomed reader may safely skip.

The singular value decomposition (SVD) is a well-known matrix decomposition that splits any matrix $\mathbf{M}$ into the product $\mathbf{M} = \mathbf{ASB}^*$ where $\mathbf{A}$ is a unitary matrix ($\mathbf{AA}^* = \mathbf{A}^*\mathbf{A} = \mathbf{I}$), $\mathbf{S}$ is a diagonal real matrix, and $\mathbf{B}$ is the conjugate transpose of another unitary matrix, all of appropriate dimension, as in the example of figure 14. The diagonal elements of $\mathbf{S}$, σ_i, are ordered such that $\sigma_i \geq \sigma_{i+1}$ and are called the singular values. When applied to statistical data, the SVD is commonly known as principal component analysis, Karhunen-Loéve decomposition, or proper orthogonal decomposition (POD). Comparison across application domains is not very meaningful however, since the object of optimization is quite different.

The singular values contained in the diagonal matrix $\mathbf{S}$ quantify the underlying dimensionality of the mapping being decomposed. Where σ_2 is $\underline{\text{small}}$ compared to σ_1, as in the simple example in figure 14, the full mapping of a unit circle at input to an ellipse at output is well approximated by the lower-dimensional mapping to a line. This example illustrates the use of the SVD to find lower-rank approximations to linear mappings between higher-dimensional spaces. The SVD generalizes to apply to linear operators on Hilbert spaces [Young, 1988] where it becomes known as the Schmidt decomposition.

Hopefully by now the application of the SVD in our context becomes obvious: since we hold that turbulence can be captured by a low-order amplifying process, we must find the "best" low-rank approximation to the resolvent, where what is meant by "best" is quantifiable in a defined sense. The result is simply a truncation of the Schmidt decomposition of the resolvent, or the identification of the right singular vectors (inputs) that give rise to the most amplified left singular vectors (outputs). The relative amplification factor for unit input amplitude is given by the associated singular value. We term the left and right singular vectors the velocity response and forcing modes, respectively; the first singular forcing modes are the most significant in that they can be expected to dominate the full observed response at a given K if the resolvent is truly low rank. We confirm this assumption in the results shown below, noting that the true output from each resolvent will be the product of forcing amplitude and singular value.

The SVD of the resolvent before Fourier decomposition is imposed would itself naturally result in a decomposition into the (optimal) Fourier basis in the symmetric directions for the reasons discussed earlier. For simplicity, we take that stage as given and consider the optimal low rank approximation only in the inhomogeneous, wall-normal direction.

The SVD of the resolvent for a particular K can be written in terms of the forcing (ϕ) and response (ψ) modes associated with the response of the flow as follows:

$$(-i\omega I - \mathcal{L}_K)^{-1} = \sum_{l=1}^{\infty} \psi_{lK}(r)\sigma_{lK}\phi^*_{lK}(r) \tag{9}$$

with the orthogonality condition

$$(\phi_{lK}(r), \phi_{mK}(r))_r = \delta_{lm}, \quad (\psi_{lK}(r), \psi_{mK}(r))_r = \delta_{lm}, \tag{10}$$

where $(\cdot,\cdot)_r$ indicates the inner product over r, such that the sets of both forcing and response modes are normalized with respect to the energy integrated over the radius of the pipe and are orthogonal. The singular values are sorted, with $\sigma_{l,K} \geq \sigma_{l+1,K} \geq 0$. For stable $\mathcal{L}_K$, this decomposition exists for real ω. It is also unique up to a pre-multiplying unitary complex factor on both bases corresponding to a phase shift and up to the ordering in l of σ_{lK}s, hence we fix the relative phases with respect to the first coefficient.

The basis pair defined by ϕ_{lK} and ψ_{lK} can be used to decompose arbitrary forcing and the resulting velocity at any particular frequency/wavenumber component K, such that

$$\mathbf{f}_K(r) = \sum_{l=1}^{\infty} \phi_{lK}(r)\tilde{\chi}_{lK} \tag{11}$$

$$\mathbf{u}_K(r) = \sum_{l=1}^{\infty} \sigma_{lK}\psi_{lK}(r)\tilde{\chi}_{lK}, \tag{12}$$

where the $\tilde{\chi}$'s correspond to the coefficients of projection of the forcing onto the forcing modes.

The radial shape of harmonic forcing that gives the largest disturbance energy (given unit forcing amplitude) at a particular K is $\mathbf{f}_K = \phi_{1K}$, with a gain of σ_{1K}. The next largest arises from $\mathbf{f}_K = \phi_{2K}$ and so on, at a particular wavenumber pair and frequency. The corresponding flow response modes are given by the related $\mathbf{u}_K = \psi_{1K}, \psi_{2K}$, etc. This decomposition of general input forcing is illustrated in figures 15(a) and (b).

At this stage, the analysis is complete in the divergence-free basis, in the sense that no modeling assumptions have been made, other than that the velocity field is statistically homogeneous in x, θ and t. Linearity of the system implies that the resolvent can be analyzed under unstructured forcing, i.e. isolating individual resolvents as shown in figure 15(a), but the appropriate amplitudes of the velocity response modes must be determined before the connected, self-sustaining representation of figure 13 can be reassembled (the topic of ongoing work). The optimal low-rank approximation to the resolvent is defined to arbitrary accuracy related to the number of singular modes included. There is a further technical assumption that the resolvent is compact. The simplest approximation is rank-1, in which the resolvent is modeled using only the first

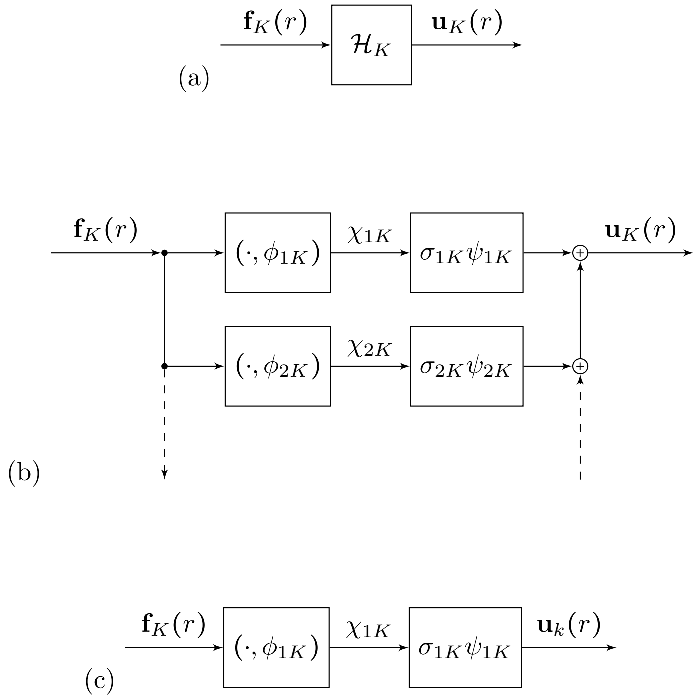

Figure 15: Block diagram for the equations (11) and (12) referring to the linear equations projected onto the forcing and response modes. Diagram (a) depicts the 'true' resolvent and (b) depicts the Schmidt decomposition of the resolvent. The rank-1 approximation is depicted in (c). This approximation can be performed for each lower sub-system in figure 13.

singular modes (figure 15(c)); this approximation is likely to be good if $\sigma_{1K} \gg \sigma_{lK}$ for all $l > 1$. While the assumption that a rank-1 approximation is sufficient to model wall turbulence is quite strong to begin with, it is one of the key outcomes of this formulation that it yields surprisingly good agreement with observations from real flows for the vast majority of observed K combinations. Of course, a higher-rank approximation may simply be made by the same process, should higher fidelity be required.

4.1.3 Response of radially-varying traveling waves and the connection with critical layer theory

The singular response modes were computed using a MATLAB implementation of the decomposition described in equations in the previous subsection and the numerical scheme and divergence-free basis for pipe flow proposed by Meseguer and Trefethen [2003], modified for a turbulent mean flow as in McKeon and Sharma [2010]. Full details of the computational approach can be found in these two papers and, for brevity, are not repeated here. The computational expense is exceedingly low, even for analysis of Reynolds number up to $R^+ = 1.97 \times 10^4$, the highest Re study we have performed to date.

McKeon and Sharma [2010] investigated the variation of the characteristics of the radially-varying traveling waves over a range of K and made some observations with respect to variation with singular value. Recall that the σ_l gives the amplification, and complex functions ϕ_l and ψ_l give the wall-normal variation of the amplitude and phase of the forcing and response mode, respectively (where the phase of the response mode is relative to the forcing). In particular, the orthogonality requirements given in equation 10 require an increase in the number of maxima in the radial amplitude function $\mathbf{u}_K(\mathrm{r})$ with increasing l (with analogy to the orthogonality of Fourier modes), as shown in the comparison of velocity response modes with increasing l in figure 2 of McKeon and Sharma [2010]. (An example of the variation of singular values with l is shown in figure 3 of that paper.) The combination of the increasing complexity of such structures and the rapid drop-off in singular value observed with increasing l support the rank-1 hypothesis for a wide range of K; in

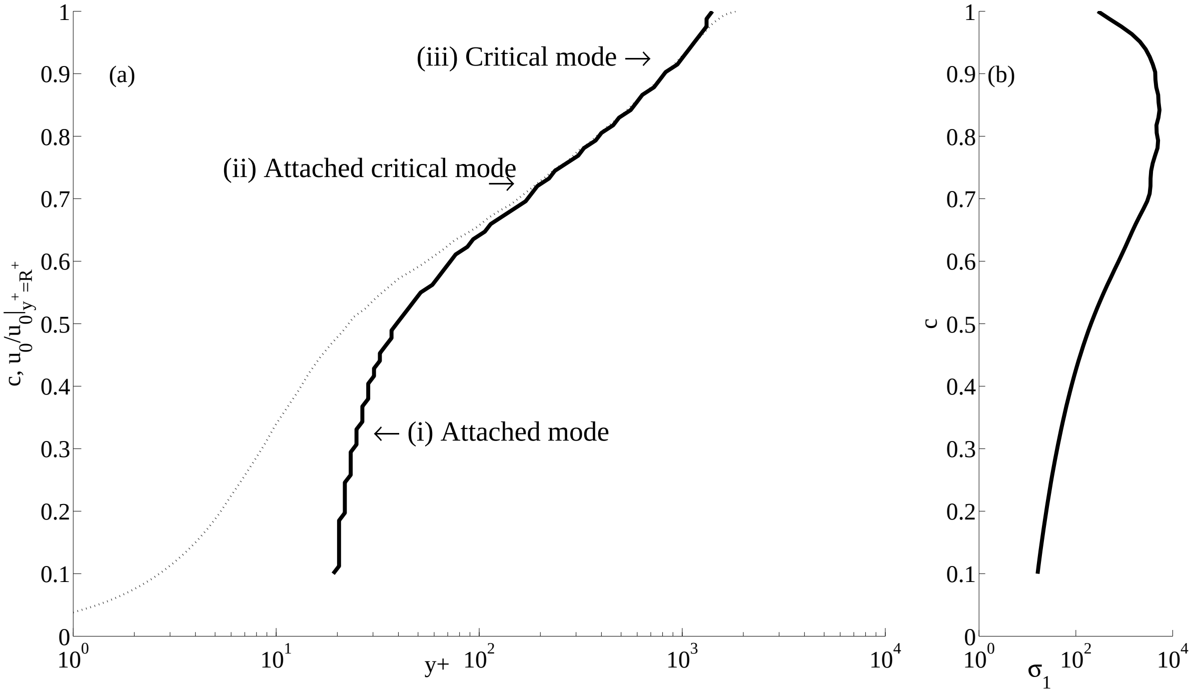

Figure 16: (a) Variation of the location of the peak streamwise velocity with increasing wavespeed, c, for the first velocity response mode with $(k, n) = (1, 10)$ at $R^+ = 1800$ (solid line). The turbulent mean profile normalized by the centerline velocity, $\mathbf{u}_0/\mathbf{u}_0|_{y^+=R^+}$, at this Reynolds number is also shown in dotted gray for reference. (b) The corresponding first singular values.

the rest of this paper, we consider only the output of the rank-1 model of the NSE at each K value (figure 15(c)), which we call the first velocity response modes.

We summarize the general features of the first velocity response modes in figures 16-17, for a particular $(k, n) = (1, 10)$ at $R^+ = 1800$. Figure 16(a) shows the wall-normal variation of the location of the magnitude of the streamwise velocity perturbation with increasing wavespeed c, compared with the local turbulent mean velocity profile $\mathbf{u}_0$. The variation with c of the associated first singular value, σ_1 is shown in figure 16(b); note that for this K (and a wide range of K in general), the magnitude of the first singular value is extremely large, meaning that only very small forcing amplitude will be required to observe a strong velocity response.

Three different types of modes can be identified in figure 16(a). The velocity response mode shapes $\mathbf{u}_K$ corresponding to these three classes of velocity response modes, identified here by (i)-(iii), are shown in figure 17. The variation of the azimuthal component is not shown since it is simply determined from the summation of left- and right-going propagating waves described earlier and the continuity equation, and is out of phase with u in both streamwise and azimuthal directions. When c is small in region (i), the peak magnitude in all components stays at an approximately constant wall-normal distance, $y^+ = yu_\tau/\nu$. We term these "attached modes", because the footprints of the modes reach down to the wall. For large c in region (iii), the location of the peak amplitude tracks the local mean velocity, i.e. $c = \mathbf{u}_0(y)$ and there exists a critical layer. The mode is localized around the critical layer, such that these "critical modes" rapidly become detached from the wall with increasing c. Some special significance will be given to the class of attached, critical modes (ii), i.e. the slowest convecting modes that achieve critical status.

Note also that the Reynolds stress associated with the velocity response modes exhibits slightly different behavior, lifting from the wall to provide a radially-localized distribution with contributions at K_0 and $2K$.

We will not comment here on the first singular forcing mode shapes corresponding to the velocity response modes shown in figure 17, beyond saying that the forcing occurs locally to the velocity response in a radial sense, and that understanding which pairs of other Ks supply a component of forcing in these directions is

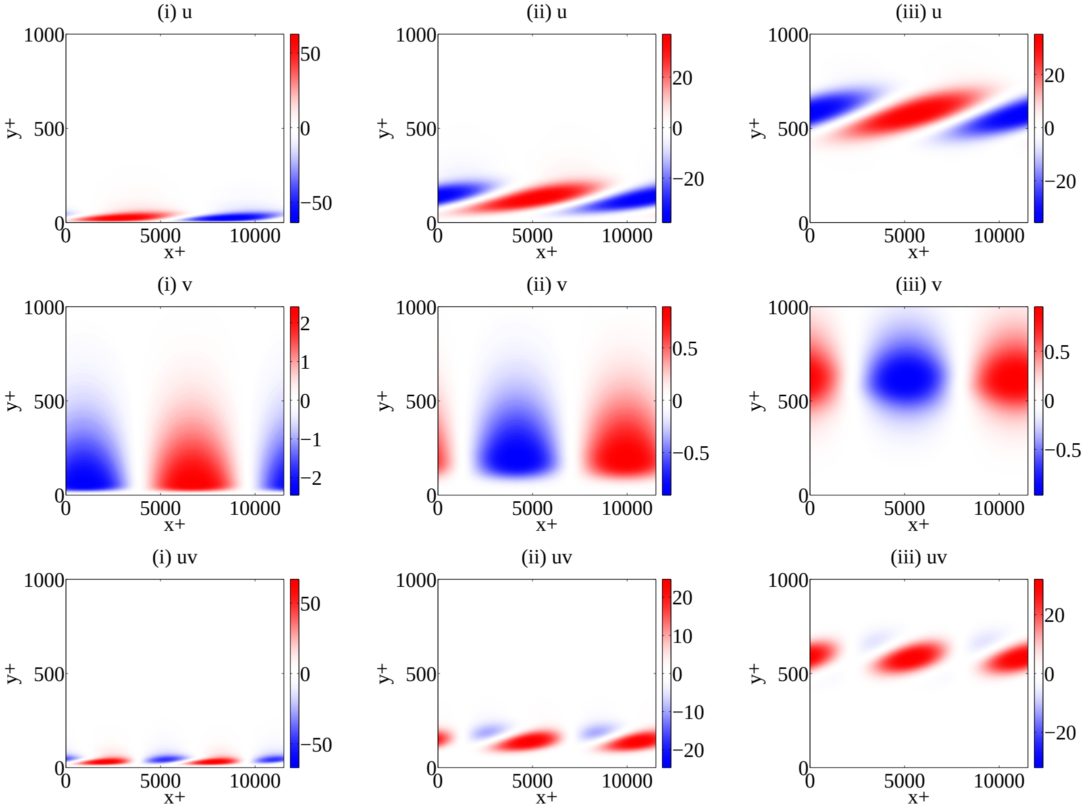

Figure 17: Representative velocity response mode shapes for the "attached", "attached and critical", and "critical modes", shown for conditions corresponding to points $(i) - (iii)$ in figure 16, i.e. $(k, n) = (1, 10)$, $c = 0.25, 0.67$ and 0.85, and $R^+ = 1800$. Top: $u(y^+)$; middle: $v(y^+)$; bottom: $uv(y^+)$.

equivalent to understanding how to close the block diagram of figure 13.

The physics underlying these distinct classes of response modes can be identified by returning to the full rank resolvent of equations 7 and 8 (and noting that the scaling phenomena observed are reflected in the rank-1 approximation). There are two distinct mechanisms by which the resolvent can lead to large amplification [McKeon and Sharma, 2010]: the non-normality associated with the $v\partial_r \mathbf{u}_0$ term coupling the radial perturbation to the mean shear (requiring a mode covering a wider range in the wall-normal direction, since it is powered by the differential in velocity over r [Bourguignon et al., 2013]), and a critical-layer type response where locally $c \simeq \mathbf{u}_0(y_c)$ giving high gain. The former effect is well understood to lead to energy extraction from the mean flow under other formulations. In the latter case, the diagonal terms in the resolvent become extremely large at the location where $c = \mathbf{u}_0(y)$ with large Reynolds number. The concept of a critical layer in wall turbulence has received much less attention, with the notable exception of the analysis by Sreenivasan [1988]. This phenomenon occurs when the resolvent at this location becomes large because, at high enough Reynolds number, the response at the critical layer to forcing is almost singular; the relevant eigenmodes approach neutral stability in the inviscid limit.

A review of the body of work on critical layers in laminar flow is given by Maslowe [1986] and Schmid and Henningson [2001]. There are some essential differences to the current development: we address the turbulent case, we maintain the presence of the nonlinear forcing term and (specific to pipe flow) the wall-normal velocity and vorticity in the Orr-Sommerfeld formulation of the problem do not decouple in cylindrical coordinates [Schmid and Henningson, 2001]. However critical layer concepts are useful, and qualitative connections are made between the theory and turbulent flow in Cartesian geometries in McKeon and Sharma [2010].

4.1.4 Closing the loop: an explicit treatment of the nonlinearity

The linear selection mechanism explains much of the form of the structure of real flow; however the nonlinearity is also important. Though it is not the focus of this work, we will briefly discuss it here for the case of a discretised field, i.e. discrete K. Using the resolvent decomposition of equation 7 and equations 9, 11 and 12, expressing the fields in terms of the coefficients with j, a, b indexing over all lK, we get

$$\mathbf{u} = \sum_j \chi_j \psi_j = \sum_j \psi_j \sigma_j \phi_j^* f_j \phi_j \tag{13}$$

where

$$f_j = \sum_{a,b} \left(-\psi_a \cdot \nabla\psi_b, \phi_j\right)_r \chi_a \chi_b = \sum_{a,b} N_{jab} \chi_a \chi_b. \tag{14}$$

Here, χ_j are the coefficients describing the projection of the velocity field onto the velocity response modes, $\chi_j = \sigma_j \tilde{\chi}_j$, and N_{jab} is the coupling between any three traveling wave singular modes. Note that $N_{jab} = 0$ where Fourier modes are triadically incompatible. The full nonlinear problem can then be reduced to the solution of

$$\chi_j = \sum_{a,b} \sigma_j N_{jab} \chi_a \chi_b. \tag{15}$$

The modeling question is the magnitude and sparseness of both N_{jab} and σ_j. Notice that high gain σ_j can compensate for low (but non-zero) N_{jab} and the quadratic property of $\mathbf{f}$ can determine the amplitudes. Since σ_j and N_{ajb} are calculated from the NSE, this system of equations together with the assumed mean velocity profile constitutes a complete description of turbulence with transient behavior removed. Sparseness makes this representation very efficient.

We see that self-sustaining mode combinations are possible if the nonlinear forcing term resulting from the interaction of component velocity modes is not orthogonal to the forcing modes required to sustain it. We could reasonably look for solutions to (15) to find self-sustaining mode combinations. Such a truncation would give a low-order, discrete representation of (15). This is the subject of ongoing work.

This view also gives an interesting insight into the equivalent of the cascade in the inhomogeneous spatial direction. In this direction, because of the distribution across r of the modes, there is a non-local (distributed) interaction with the mean shear. This possibility of extracting energy from the velocity profile is mathematically captured by the non-normality. The critical layer response, by contrast, is localized in r.

The triadic interaction in homogeneous isotropic turbulence (or the t, x and θ directions) is well understood; the mechanisms for energy transfer have now been effectively extended to the inhomogeneous directions by the analysis. The nonlinearity, in addition to transferring energy across ω, k and n, subject to the rules of triadic interaction, may also transfer energy across response modes in y, subject to the three-way interaction N_{jab} and the singular values σ_j. The ability of a mode to drive others in the wall normal direction, essentially the wall-normal cascade, is determined by the localization of the mode in that direction, which in turn determines N_{jab}. This concept is explored further in Bourguignon et al. [2013].

4.1.5 Where to look in 3D spectral space?

In the absence of a solution to equation (15) that identifies the modes required to sustain the turbulence with $N_{jab} \neq 0$, our analysis at this stage is guided by the range of K observed in real flows, which has been shown to correspond well to the range where the first singular values have large magnitude by Moarref et al. [2013]). This localization and high response at the critical layer dictates that the turbulent flow's energy is concentrated around a thin "spine" in (k, n, ω, l) space, where l is the singular value index, which essentially describes a low-dimensional attractor in this space. This will also be discussed in forthcoming work. As such, we briefly review work that has characterized the scales and wall-normal variation of the three-dimensional, spatio-temporal K spectrum (which in its entirety is still a relatively uncommon result) and has thus informed our work.

The statistics and spectra of the turbulent fluctuations have been historically well studied, such that results including the Reynolds-number independence of the near-wall cycle and the energetic importance of the very large scales emerging with increasing Reynolds number are now well established. However, the classification of coherent structure and their connection to velocity statistics can be said to be a more recent focus, significantly enabled by advances in computational and experimental diagnostic technology. The essential structural features of wall turbulence have been listed recently by Smits et al. [2011]. In order of increasing streamwise scale, this list consists of near-wall streaks of streamwise velocity, hairpin vortices, large scale motions (LSM) believed to correspond to organization of hairpin vortices into packet structures, and very large scale motions (VLSM) with streamwise extent on the order of ten times the outer lengthscale. The temporal frequency is most simply addressed through the range of convection velocities observed in the flow [Morrison and Kronauer, 1969, Morrison et al., 1971, del Álamo and Jiménez, 2006, Dennis and Nickels, 2008, LeHew et al., 2011].

Assuming the approximate universality of spectra between canonical flows documented by Monty and Chong [2009] and the range of scales described in Smits et al. [2011] and references therein, conservative estimates of the energetically active $K = (k, n, c)$ ranges are then $0.1 < k < 2\pi R^+/100$, $2\pi/0.1 < n < 2\pi R^+/10$ and $10/\mathbf{u}_0^+|_{y^+=R^+} < c < 1$. Practically, the sum of K and its complex conjugate, and both left- and right-going waves ($\pm n$) must be considered in order to obtain real-valued amplitudes and avoid a non-zero mean spanwise velocity, respectively. In what follows, we constrain our interrogation of the resolvent analysis to these values and document well-known features of wall turbulence that are captured by the rank-1 approximation to the resolvent.

4.2 Reproduction and extension of statistical and structural results in unperturbed wall turbulence

An array of quantifiable features of wall turbulence have been well described in the extensive wall turbulence literature, including velocity statistics, spectral information and organizations of coherent structure, even if their Reynolds number scaling and dynamical importance still remain sufficiently elusive to preclude effective low order modeling. Of course, even observing these features at high Reynolds number presents severe experimental and numerical challenges, but assimilation of the characteristics of all such recognizable results is required for a full understanding of wall turbulence.

Our analysis naturally leads to information related to velocity spectra and distribution of statistics in the wall-normal direction, and we will present selected results in this subsection. We also target the different classes of structures listed in subsection 4.1.5 above, demonstrating that the analysis has the potential to

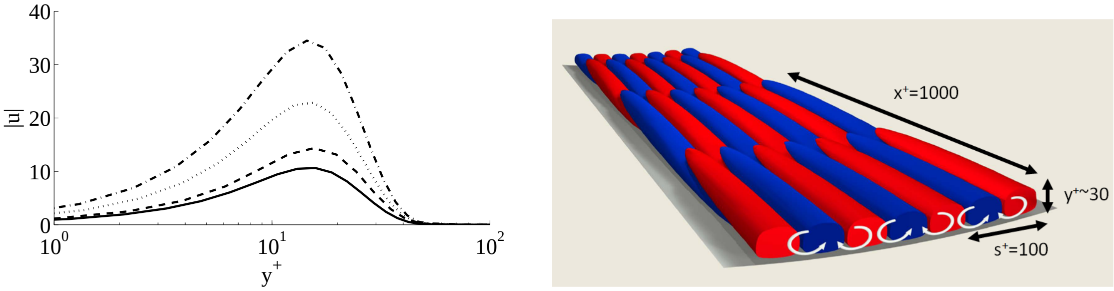

Figure 18: (a) Distribution of streamwise energy over the pipe radius for the near wall mode with $K = (2\pi R^+/1000, 2\pi R^+/100, 10/\mathbf{u}_0^+|_{y^+=R^+})$. Reynolds numbers: — 75×10^3, -- 150×10^3, ··· 410×10^3, ·-· 1×10^6. (b) Shape of the first singular mode representative of the dominant near wall motions. Color denotes isosurfaces of streamwise velocity (streaks), where red and blue correspond to high and low velocity respectively relative to the mean flow (heading into the page), and the white arrows show the sense of the in-plane velocity field.

unify the statistical and structural observations of wall turbulence and lead to inferences about the key underlying physics.

We note that experimental studies typically interrogate data based on averaging conditional on some characteristic typical to the structure to be examined. For instance, Dennis and Nickels [2011b] average conditional on a swirl criterion to identify hairpin vortices, yielding the scale distribution in K and y associated with the structure. In contrast, we work in the opposite direction: specifying K and yielding the wall-normal distribution of the velocity of the response modes, which we associate with coherent structure.

4.2.1 Near-wall cycle

The structure and dominant dimensions associated with the autonomous, near-wall cycle of turbulence have been known since the seminal experiments of Kline et al. [1967a]. Significant study of the dynamics of the flow in this region, performed by, e.g. Waleffe [1997], Jiménez and Pinelli [1999], Schoppa and Hussain [2002] using low Reynolds number data, revealed the well-known quasi-streamwise vortex and streamwise velocity streak structure, while experiments in the atmospheric surface layer [Klewicki et al., 1995] have demonstrated the Reynolds number independence of the streak spacing in viscous units at the near-wall scales identified above, namely $\lambda_x^+ \approx 1000$ and $\lambda_z^+ \approx 100$. Comparison with the structure arising from our analysis requires the specification of an additional parameter, the phase velocity, c. For the dominant wavelengths associated with the near-wall cycle, the first singular mode is critical and attached to the wall, as identified in figure 17, when $c^+ = 10 - 15$, the minimum convection velocity associated with energetic disturbances.

The wall-normal distribution of the streamwise component of the first singular mode with

$$K = (2\pi R^+/1000, 2\pi R^+/100, 10/\mathbf{u}_0^+|_{y^+=R^+})$$

is essentially Reynolds number-independent, as shown by the distributions of the amplitude over an order of magnitude in Reynolds number in figure 18(a). In fact, this independence emerges directly from the Cartesian coordinate version of critical layer scaling [McKeon and Sharma, 2010] for modes with K constant in inner units in a region where the mean velocity profile is self-similar in inner units, i.e. for sufficiently high Reynolds numbers. The first singular velocity response mode captures this scaling and thus postdicts from a low rank approximation to the NSE that the location of the near-wall cycle activity should be Reynolds number independent. Similar results can be obtained for outer scaling modes [McKeon and Sharma, 2010].

The velocity components are distributed in such a way as to create a periodic array of alternating streamwise velocity streaks accompanied by streamwise-aligned vortices in the cross-stream plane, which are elevated slightly from the wall with increasing downstream distance. See figure 18(b), figure 1 from McKeon et al. [2010], for a cartoon of the structure associated with this near-wall mode. There is a strong resemblance to a system of quasi-streamwise vortices and streaks of streamwise velocity, with the simplicity of this

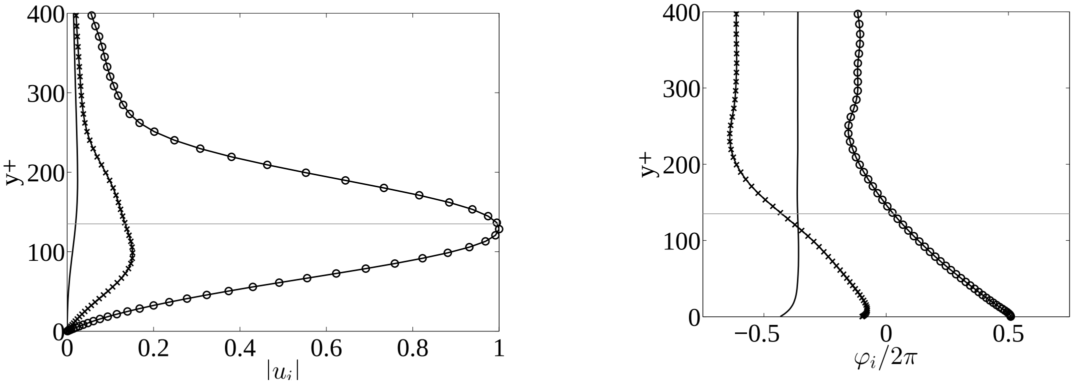

Figure 19: Wall-normal variation of (a) amplitudes of the three velocity components and (b) corresponding phases in multiples of 2π for the VLSM response mode with $K = (1, 10, 2/3)$ at $R^+ = 1800$. The lines denote $-o-$: u, $-$: v, $-\times-$: w. Solid/dashed horizontal line shows the location of the critical layer.

representation made possible because of the absence of decorrelation associated with the many other (less-energetic) K modes that are active in this region of the flow.

Thus we see that, first, the rank-1 approximation to the resolvent generates velocity response modes that display the scaling, distribution and structure consistent with the state of understanding concerning the near-wall cycle. Secondly, a modified critical layer analysis provides scaling consistent with observations of wall turbulence.

4.2.2 Characteristics of the very large scale motions

Similar success can be obtained by studying the first singular velocity response mode at the K combination believed to correspond to the very large scale motions (VLSMs). Figure 19 shows the response mode amplitude and phase associated with $K = (1, 10, 2/3)$, selected by McKeon and Sharma [2010] to best match a series of observations of VLSMs in the literature that are incomplete in terms of the three parameters required for input to our analysis. Irrespective of the exact values selected, the general form of this mode is similar to the attached critical mode shown in figure 16, namely streaks of streamwise velocity with a small inclination from the wall and associated cross-stream vortices, in agreement with the observations of Hutchins and Marusic [2007] and Chung and McKeon [2010]. The strength of each of these features, common to attached critical modes, depends on the aspect ratios given by the ratios of k, n and c, where the last dictates an approximate wall-normal scale associated with the wall-normal distance to the critical layer. Consequently, the cross-stream component is weak for the VLSMs.

Of particular interest are the distributions of the wall-parallel components of the mode. Near the wall, in the region that gives the mode its “attached” designation, the phase of the mode monotonically decreases, leading to the aforementioned small angle of inclination to the wall. However, further from the wall the amplitude is smaller, but there is essentially zero phase variation in the wall-normal direction. Not only does this behavior mirror the expected phase variation beyond the π phase jump associated with classical critical layer theory [Maslowe, 1986], but it is also in good agreement with cross-correlation results in the literature that had remained somewhat puzzling [Tutkun et al., 2008, Guala et al., 2010, Chung and McKeon, 2010]. Guala et al. [2010] observed similar shapes in the two-point cross-correlations, $R_{xx}(r_x^+, y^+, y_{ref}^+)$, in the near-thermally-neutral atmospheric surface layer, with temporal records transformed to the spatial domain using Taylor’s hypothesis. The expected near-wall structural angle was observed with a reference location, y_{ref}^+, close to the wall, while a sufficiently large y_{ref}^+ led to effective capture of a region of weaker correlation with reduced phase variation far from the wall. Interestingly, Chung and McKeon [2010] found similar behavior of the velocity field in LES of long channels conditioned on the occurrence of large-scale negative and positive velocity excursions, with the same dependence on the wall-normal location of the condition. Note that while

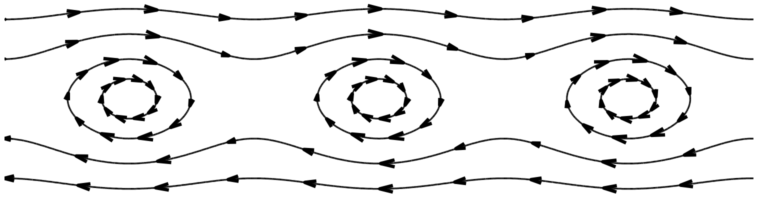

Figure 20: Kelvin's cats' eyes (also called Kelvin-Stuart vortices): structure at the inviscid, laminar critical layer as observed by an observer moving at the critical velocity.

there is some ambiguity concerning the interpretation of streamwise scale from both the cross-correlation results and conditional average procedures, it is clear that the dominant scales are of the order of several boundary layer thicknesses long in the streamwise direction. It also seems that the general variation of phase in the wall-normal direction described above is a common feature that can be more easily isolated by these techniques as the Reynolds number increases and the peak amplitude of the LSM/VLSM both increases and occurs further from the smaller-scale near-wall activity. We note also that the mode shown in figure 19 has a non-negligible amplitude over at least 30% of the radius, in which distance the change in mean velocity is approximately 80% of the centerline velocity, underscoring the underlying reason for the failure of Taylor's hypothesis for very large streamwise scales [Monty and Chong, 2009].

For $K = (1, 10, 2/3)$, a simple prediction of the scaling of the peak location in streamwise amplitude, y_c^+, can be made, where y_c^+ is understood to track with reasonable fidelity the wall-normal location of the critical layer. McKeon and Sharma [2010] showed that the wall-normal location where the response mode with $(k, n) = (1, 10)$ first attains attached critical status occurs at $c = 2/3$, independent of Reynolds number, and that this location lies within the region of logarithmic scaling of the mean velocity. The latter observation allows expression of the y_c^+ in terms of the local mean velocity at the critical layer, two-thirds of the centerline velocity, solely by taking advantage of the log law and Reynolds similarity of the outer flow:

$$\frac{1}{\kappa}\ln y_c^+ + B = \frac{2}{3}\left(\frac{1}{\kappa}\ln R^+ + B + C\right). \tag{16}$$

Here κ is the von Kármán constant, and B and C are the additive constants associated with the mean velocity in the log region and the constant wake function. Solution of equation 16 with standard values for the constants [McKeon and Sharma, 2010] leads to the prediction of

$$y_c^+ = 0.8R^{+\ 2/3}, \tag{17}$$

which appears to be well-borne out by examination of the experimental data of Morrison et al. [2004] (McKeon and Sharma [2010], figure 13).

Despite the difficulties applying critical layer analysis to turbulent pipe flow identified earlier, it is worth mentioning a related result that is at least encouraging. McKeon and Sharma [2010] observed that classical critical layer analysis yields a scaling with $R^{+\ 2/3}$ for the critical layer in the upper branch solution for neutrally stable modes, along with the more recognizable $R^{+\ 1/2}$ for the wall layer in both upper and lower branches. The critical layer in the lower branch scales with $R^{+\ 1/5}$. That the exponent from the classical analysis is in agreement with the scaling of the VLSM energetic peak gives hope that the $c = 2/3$ for the VLSM determined observationally from our analysis is a fundamental theoretical result. However, the comparison of the variation of the location of the VLSM peak in the boundary layer data of Guala et al. [2010] and (a proxy for it) from Mathis et al. [2009] shown in figure 16 of McKeon and Sharma [2010] with the pipe result of equation 17 gives a hint that this behavior (the branch choice) may not be independent of flow geometry.

4.2.3 Hairpin vortices and structural organization

Our discussion of self-organization of coherent structure and its relationship with energetic large scale motions afforded from resolvent analysis begins with reference to the classical structure of the critical layer described by Lord Kelvin, which hints at the origins of hairpin vortices. Figure 20 shows a sketch of the periodic, closed streamline structure seen by an observer moving at the critical velocity associated with a classical, inviscid (two-dimensional) critical layer. The three-dimensional wavenumbers expected from observations of wall turbulence (as opposed to the two-dimensional perturbations that emerge as the most unstable in linearly unstable laminar flow via Squire's theorem) suggest that any structure derived in the turbulent case will be more complex: at the very least, the superposition of left- and right-running velocity response modes suggests a three-dimensional vorticity variation, which we will show below appears to represent the commonly-drawn outline of a hairpin vortex.

A fundamental concern with considering coherent vortical structure in a turbulent field associated with a strong mean shear is the challenge of objective identification of rotation over shear. Recent reviews of this problem are given by, e.g., Jeong and Hussain [1995] and Chakraborty et al. [2005]; for the simplified flow fields associated with the linear superposition of velocity response modes investigated here, all common identifiers give similar results, hence we choose to work with swirl, λ, which is given by the magnitude of the imaginary part of the complex conjugate eigenvalue pair associated with the velocity gradient tensor. This is, as are all the common diagnostics, a nonlinear function of velocity (a characteristic that leads rapidly to structural complexity, as we will show below). Therefore, while the velocity response modes can be linearly superposed to obtain approximations to the full velocity field of increasing veracity, a faithful representation of the full swirl field can only be obtained by summation of all active velocity response modes (with the correct amplitudes). However, our aim here is to show that the recognizable foundations of the structure observed in full flow can be traced to resolvent analysis, and specifically that phenomena like evolving packets of hairpin vortices arise naturally from the resolvent analysis as studiable sub-units.

Figure 21 shows an isosurface of the swirl field associated with $K_1 = (6, 6, 2/3)$, a critical mode in the terminology of subsection 4.1.3 that is just detached from the wall. Sharma and McKeon [2013a] selected this response mode as one of a triadically-consistent set that includes the VLSM (we summarize the full corresponding swirl field below). A periodic array of pro- and retro-grade hairpin-like vortices is found, where prograde implies rotation in the classical sense with a contribution to $-uv$, and the opposite for a retrograde vortex. This is as expected since the response modes represent the velocity distribution relative to the local mean velocity and there can be no mean contribution to the mean shear from the response mode. These coherent vortical structures can be understood phenomenologically to be the three-dimensional equivalent of Kelvin's cats' eyes. Reference to figure 17 confirms that the associated Reynolds stress is localized around the critical layer and detached from the wall, making the characteristics of this mode consistent with the foundational elements of Townsend's attached eddy hypothesis.

The swirl function identifies regions of rotational motion, but it is susceptible to contamination by local shear gradients in the sense that the absolute value of the swirl can be either increased or decreased by the simultaneous presence of shear. Most notably, the positive shear associated with the mean profile can be shown [Sharma and McKeon, 2013a] to increase (suppress) the swirl value associated with prograde (retrograde) hairpin vortex heads. This is a thresholding problem: rotational motion is still captured for both senses of vortex rotation, but the usual thresholding techniques applied to velocity fields lead to a systematic under-accounting of retrograde vortices. McKeon et al. [2010] explored this phenomenon in the context of this work with respect to observations of swirl in the streamwise/wall-normal plane of a zero pressure gradient turbulent boundary layer, while Carlier and Stanislas [2005] documented earlier the general characteristics of the distributions of pro- and retro-grade hairpin vortices.

In the context of exploiting the resolvent analysis to demonstrate recognizable structure, we explore further the effect of local shear associated with combinations of velocity response modes. An energetic VLSM, for example, can be viewed as enforcing a periodic, enhanced and reduced local Reynolds number on the smaller motions, accompanied by positive and negative shear, $\partial u_K / \partial y$. In this sense, it can be considered to be an inactive motion in the terminology of Townsend. A similar effect occurs in the other velocity components and gradient directions, but the strongest of these is the wall-normal gradient of streamwise velocity, at least for the large scales which have long been associated with vortex organization in the literature. Thus the distribution of hairpin vortices with a particular K, which is periodic in the absence of other modes, will be modified by local shear associated with the linear superposition of any other (sufficiently energetic) velocity modes, and this modification gives rise to the self-organization of vortical structures familiar in the literature.

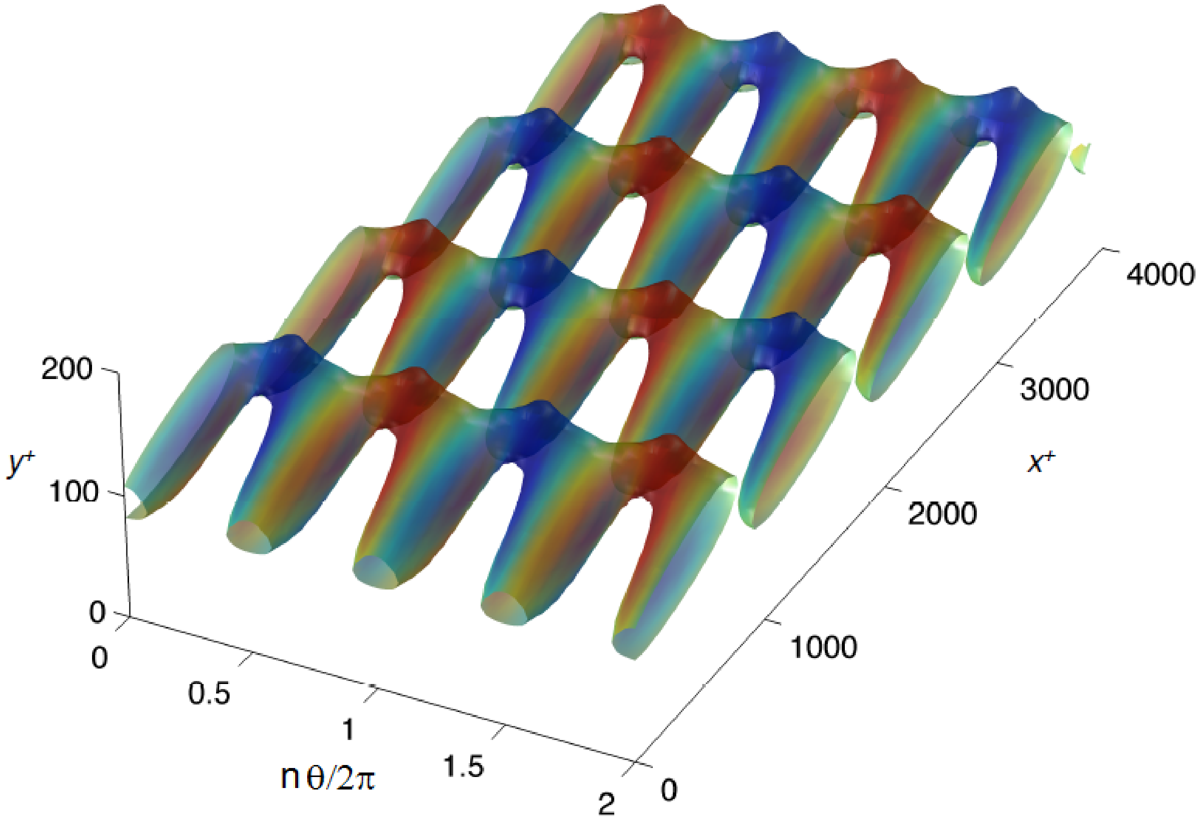
200
y^+
100
0
0
0.5
1
1.5
2
$n\theta/2\pi$
0
1000
2000
3000
4000
x^+

Figure 21: The periodic array of pro- and retro-grade hairpin vortices associated with near-wall velocity response modes at $R^+ = 1800$, identified by an isosurface of constant swirling strength at 50% of the absolute maximum value, color-coded with the local (model) azimuthal vorticity. Red and blue denote rotation in and counter to the sense of the classical (prograde) hairpin vortex respectively.

This phenomenon is described at length in Sharma and McKeon [2013a], but we demonstrate the complexity of vortical structure that can arise under the superposition of three modes in figure 22. The three modes $K_1 = (6, 6, 2/3)$, $K_2 = (1, 6, 2/3)$ (VLSM) and $K_3 = (7, 12, 2/3)$ are triadically-consistent in K and overlapping in the y direction, and will be phase-locked in the sense that the identical wavespeed means that there is no relative motion between the modes and therefore no evolution of the packet. Sharma and McKeon [2013a] selected relative mode amplitudes consistent with experimental observations, specified a $\pi/2$ phase difference between the large-scale envelope of the two shorter modes and the VLSM in the streamwise sense and aligned the peak streamwise intensities in the azimuth, in order to generate the complex swirl distribution shown in figure 22, which is recognizably a series of packets of hairpin vortices. Three prograde vortices with two retrograde ones sitting downstream and above the main packet can be clearly identified, along with some weaker vortices of both senses below the packet. The prograde hairpin heads occur further from the wall with increasing streamwise direction and are collocated with the inclined interface between positive and negative streamwise velocity fluctuation imposed by the VLSM (the location of maximum shear), giving the packet its distinctive shape. We find the complexity of coherent structure arising from even the idealized arrangement of only three modes to be striking.

This assembly of modes was deemed an "ideal packet" by Sharma and McKeon [2013a] because of its lack of evolution (matched wavespeeds) and spatial alignment. Note that this is developed as an example of structure from the resolvent analysis that can be simply interrogated rather than a structure that we expect to observe in a real flow. Relaxing any of the alignments or superposing more velocity response modes will disrupt the coherence of such a packet, such that isosurfaces of the swirl diagnostic identify the canes and arches generally observed in moderate Reynolds number wall turbulence. Permitting a range of wavespeeds leads to packet evolution in space and time. However, Sharma and McKeon [2013a] speculate that this combination of modes is dynamically important and likely to be self-sustaining, in addition to being triadically compatible, and termed it a "turbulence kernel". It should be understood that the Reynolds stress associated with the correct assembly of velocity response modes supports the (currently assumed) mean velocity profile, but in the resolvent interpretation this comes from the mean contributions to the $-uv$ distribution rather than the concentration of stress associated with the hairpin heads, both of which can be observed in the bottom panes of figure 17. The resolvent analysis offers a different explanation for the source of the Reynolds stress from that offered by the attached eddy hypothesis. In the latter, the distribution of eddies effectively describes the mean velocity profile and the scaling of the velocity fluctuations.

A simple superposition of first singular modes gives clear insight into a mechanism of self-organization in wall turbulence. In crude terms, the local variations of shear associated with the linear superposition of velocity modes bias the identification of structure to the edges of regions of energetic large scale streamwise motion (the zones of constant momentum of Adrian et al. [2000]), implying that coherent vortex structure is most likely to be observed around streamwise streaks of low velocity, as shown, e.g., in the elegant conditional averaging of time-resolved PIV by Dennis and Nickels [2011a]. Perhaps, then the well-known organizational characteristics of LSMs and VLSMs in terms of the observed preferential wall-normal and spanwise locations of hairpin vortices flanking large scale energetic motion can be at least partially attributed to the choice of nonlinear diagnostic for measuring swirling motions.

4.3 Summary

The agreement between response modes and observations of the real flow detailed above suggests that the low rank approximation to the NSE afforded by the first singular response modes over the range of wavenumbers and frequencies observed in real flows is a useful tool for modeling wall turbulence and illuminating dominant flow dynamics. It is important to stress that the *dynamics* of the flow are captured and explained by the analysis. Of particular note is the faithful connection to observed results and the potential for informed, minimum effort control. The frequency-domain interpretation, essentially a decomposition into propagating waves in the homogeneous directions, leads to a self-sustaining system in which the Navier-Stokes nonlinearity acts as a feedback mechanism to excite a set of sub-systems with highly directional amplification. The formulation can appear somewhat controversial because in important respects it is a *linear* analysis of a flow that is known to be nonlinear, but, as shown in figure 13, this representation is complete in the divergence-free basis. In essence, the nonlinearity is accounted for implicitly through the assumption of the turbulent

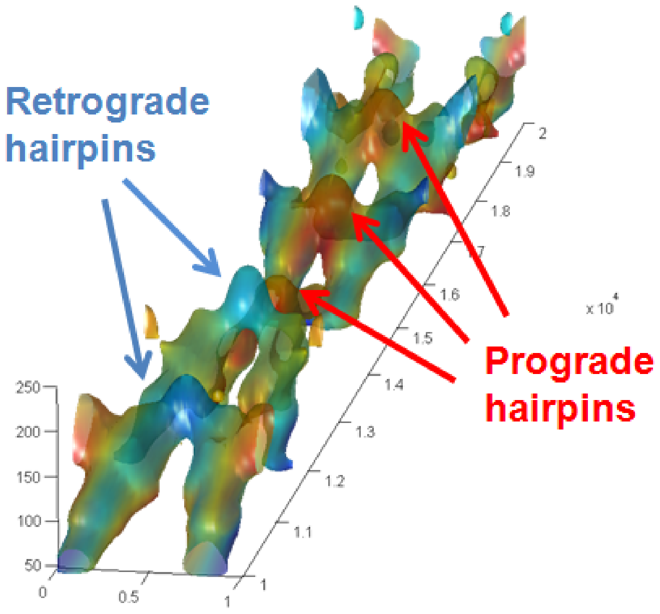

Figure 22: Isosurfaces of constant swirling strength (33% of maximum value) for the "ideal packet" at $R^+ = 1800$, color-coded by the local (model) azimuthal vorticity. Red and blue denote rotation in and counter to the sense of the classical hairpin vortex or prograde and retrograde vortices, respectively.

mean velocity profile and explicitly as providing a forcing at all wavenumber/frequency combinations, which is required to sustain the turbulent fluctuations. More information on the organization of the flow, essentially the amplitudes and relative phases of the velocity response modes, appears to be available from consideration of the triadic interactions such as those presented by our turbulence kernel; this is beyond the scope of the current manuscript, but is explored in Sharma and McKeon [2013a]. Another benefit of using the systems paradigm is the potential for carrying over closed-loop control thinking and technology to explore the possibilities for turbulence control in the presence of an almost ideal model.

Our discussion has focused on the (linear) resolvent operator relating the nonlinear interaction between scales and the velocity response modes at each wavenumber/frequency combination. The resolvent contains an analytical description, derived from the NSE, of the linear contents of Clauser's black box. To a large extent, its form determines the form of the lower-dimensional attractor guiding turbulent flow.

Much of the analytical development described here has been devoted to determining the appropriate basis for the inhomogeneous wall normal direction. In the spirit of a gain analysis, we used the singular value decomposition, which ranks input forcing distributions (right singular vectors) at a particular wavenumber/frequency combination, K, in terms of the amplification described by the singular values. The observed output will be a product of the amplitude of forcing and singular value summed over the singular values. At heart, the decomposition yields a basis for coherence in the wall normal direction.

The success of the first singular velocity response modes (left singular vectors) in describing a range of observed features in unperturbed high Reynolds number wall turbulence demonstrates that the resolvent can be considered low rank over the range of K observed in real flows, and rank-1 in many cases, with little error. In particular, the rank-1 approximation appears capable of providing coupled insight into the existence and organization of coherent structure within the framework of the distribution of fluctuating velocities, which we believe to be a first for an NSE-based analysis.

We believe that the resolvent formulation represents a promising approach towards the pre- and post-diction of the behavior of wall turbulence, for understanding the essential dynamics of a perturbed flow, effecting control, and developing low order models.

Limitations of the approach

We include here a brief description of the limitations of the resolvent analysis, both in its current formulation and in terms of extension to other flows.

A key limitation in the current analysis lies in the lack of information that emerges concerning relative amplitudes and phases between modes. This is a consequence of the use of unstructured forcing and the decomposition being optimized for "gain". Other choices of decomposition can give weight to relative phase information, including the sector-bounding analysis mentioned earlierSharma et al. [2011], Sharma [2009], which will be more important where the critical layer mechanism is less dominant and non-normality drives the modesBourguignon et al. [2013]. This would seem to correspond to regions where Taylor's hypothesis fails. The amplitudes can be determined by establishing the requirements on self-sustaining sub-systems put forward in equation 15. The velocity response modes contain information analogous to the power spectral density, in that amplitude and spatial localization can be determined by the SVD.

The first singular response modes appear to capture many features of wall turbulence, but the strict rank-1 approximation has been shown to be insufficient to capture details of the globally most energetic Fourier modes projected out of DNS of turbulent pipe flow [Bourguignon et al., 2013]. These Fourier modes span a significant portion of the pipe radius, leading to a relatively large integral contribution to the turbulent kinetic energy despite a local amplitude distribution that is a fraction of that from other K values. As such, the wall-normal coherence of these modes can be identified by proper orthogonal decomposition. Bourguignon et al. [2013] show that the failure of the rank-1 approximation for this class of mode is associated with its extended radial span and can be predicted by analysis of the resolvent itself. As such, a low-rank approximation (with rank greater than one but nonetheless less than ten) still appears to capture the majority of the energy content. We believe that the absence of this type of radially tall coherence in the rank-1 approximation is responsible for the absence of "bulges" or LSM in our analysis. Again, we associate these with modes for which phase is important.

The gain formulation of the SVD means that the results are in essence weighted to capture the most energetic streamwise velocity component for the majority of K combinations. The success of the rank-1 approximation in capturing the other velocity components, and in particular the wall normal velocity, requires additional investigation. The Reynolds stress profiles associated with the first singular response show promising agreement with the attached eddy hypothesis and experimental observations, but a good approximation to this distribution will be required in order to sustain the (currently assumed) mean velocity profile.

With respect to application of our analysis to other canonical flows, the spatial inhomogeneity associated with a boundary layer also suggests the possibility of fundamentally different behavior to fully-developed flows, particularly if the locally-parallel approximation is not good.

Lastly, we note that the current level of sophistication in this approach does not support modeling based on coherent structure, a method that has been a focus of research aimed at finding low order models for wall turbulence motivated by the importance of structure to momentum transport, concentration of Reynolds stress, etc. Our work to date identifies the complexity of coherent structure, associated with a nonlinear diagnostic, in an otherwise linear model. In essence, a full description of all energetically-active modes may be required to observe the full dynamics and evolution of coherent structure, which would probably preclude simple low order modeling.

Future trends

We conclude by briefly outlining possible future developments ranging from further interrogation and modeling of the current formulation to extension to account for increasing flow complexity. We believe that features of wall turbulence beyond those described in subsection 4.2 are amenable to description using our analysis. For example, there appears to be a strong relationship between the wall-normal profiles of skewness and the amplitude modulation coefficient, in particular with respect to triadically-consistent K combinations that include the VLSM motion [Sharma and McKeon, 2013a]. These two measures can then be interpreted as giving information about the relative phases between velocity response modes, one of the missing pieces of our analysis to date, as identified above.

We have also noted the likely potential of the resolvent analysis to treat rough walls, or at least those with periodic geometries. Under this scenario, admitting a spatial variation of the mean flow and perhaps excitation of a range of frequencies due to local flow separation seem to be conceptually simple extensions likely to give insight into roughness-induced changes to the flow.

An important next step will be to "close the loop", in the sense of determining the amplitudes of the velocity response modes observed in (projected out of) real flows that are required to fulfill the condition of self-sustenance implied by the full NSE formulation of figure 13. Once these amplitudes have been identified, a full description of energy transfer pathways and scaling with Reynolds number can be obtained. Extraction of energy from the mean flow, spatial transport, spectral transfer and local triadic interactions responsible for sustaining the flow all follow from examination of the resolvent and energy gradients. The existence of self-sustaining turbulence kernels, or limited combinations of modes that are capable of self-exciting via triadic interaction, is a topic of current study. Well-known examples exist in the literature without the coherent propagating wave interpretation, but additional such solutions seem likely [Sharma and McKeon, 2013a]. We note also the likely connection between this kind of development and nonlinear traveling wave solutions identified for transitional pipe flow [Kerswell, 2005]. Closed-loop control, given a sufficiently good model, also seems a logical next step.

As noted in the previous subsection, our analysis begins by assuming a mean velocity profile, which must be sustained by the combined action of the perturbations about it. Although the resolvent associated with the mean velocity is contained in the formulation via the K_0 mode, a means of approximating it and identifying the sensitivity of the response modes to deviation from the true profile would be useful, to say the least. Towards this end, one of the authors has investigated a two-dimensional, three-component ("2D/3C") model which appears to isolate the appropriate dominant nonlinear mechanism governing the mean velocity [Gayme et al., 2010, Bourguignon and McKeon, 2011] Future advances seem feasible. In this vein, we note that all the turbulent mean profiles we have encountered lead to stable $\mathcal{L}_K$. With appropriate tribute to Malkus [1956], we conjecture that the turbulent mean velocity profile $\mathbf{u}_0$ always leads to stable $\mathcal{L}_K$, to avoid a singular resolvent response.

5 Experimental measurements of the frequency/wavenumber spectrum and coherent structure using time-resolved PIV

One component of the work performed under this grant was a first characterization of the three-dimensional spectrum of the velocity fluctuations in a canonical turbulent boundary layer, i.e. the decomposition of the fluctuation energy by streamwise and spanwise wavenumber and temporal frequency. Typical experiments and simulations consider either the streamwise wavenumber or temporal frequency spectrum; conversion between the two can be estimated using Taylor's hypothesis of frozen turbulence. While some attention has been paid to the associated implications for structure convection velocity, there has been only limited investigation into the distribution of energy in this spectral space. By employing time-resolved particle image velocimetry (PIV) in a water channel, the measurements reported here detail the three-dimensional spectrum in three wall-parallel planes at wall-normal heights corresponding to different scaling regions of the boundary layer. Besides providing a fundamental contribution to characterization of wall turbulence, this information provides direct input to the resolvent analysis described in subsequent sections.

In addition, the time-resolved information was used to identify and track individual coherent structures in the measurement domains and characterize their trajectory, lifetime and footprint at the wall.

Full details of this work reported in this section were published in Experiments in Fluids as LeHew et al. [2011] and LeHew et al. [2013].

5.1 Experimental Setup

Measurements of a zero-pressure gradient boundary layer developing over a flat plate were performed on a 1.1m long by 0.45m wide Plexiglass plate with an elliptical leading edge and an adjustable wedge-shaped trailing edge flap situated in a 2m long by 1m wide test subsection of a free surface water tunnel facility. The 13.9mm thick boundary layer on the bottom of the plate was studied to avoid interaction with surface waves. A shroud with a wedge-shaped leading edge was placed along the sides of the plate to promote a two-dimensional flow. A thin strip of tape (approximately 3mm long, 0.25mm thick, and spanning the width of the plate) was placed immediately downstream of the elliptical leading edge on the measurement side to promote transition and favor the establishment of a turbulent regime at the measurement location. The flow was conditioned by passing it through a perforated plate, a honey comb, three turbulence reducing screens and finally a 6:1 contraction. Measurements were made starting 0.63m downstream of the leading edge. The free stream velocity was 0.67m/s and the free stream turbulence level was less than 0.1%. The free stream velocity, and thus Reynolds number, for these experiments was set to provide the best flow conditions possible and to allow a small enough displacement per frame for accurate PIV mesurements. It should be noted that this choice led to a relatively low Reynolds number, $Re_\tau = 470$, which limits the scale separation observable in these experiments. A diagram of the tunnel and a photograph showing the test subsection and coordinate system are presented in Fig. 23.

Time resolved 2D PIV was used to measure the flow field in the wall-normal and wall-parallel directions in two separate experiments using a LaVision PIV system with 2 Photron Fastcam APX-RS high speed cameras equipped with Tamron SP AF 180mm F/5.5 macro lenses. The cameras acquired images at 2000 frames per second with 1024x1024 pixel resolution for all experiments. The flow was seeded with 10μm hollow glass spheres with a specific gravity of 1.1. The seeding density was similar in both wall normal and wall parallel measurements and the average particle image diameter was 2.2 and 3.1 pixels, respectively. The flow was illuminated by a Photonics DM20-527 solid state laser providing 20mJ/pulse with a sheet thickness of approximately 1mm. The sheet was thick enough to nearly eliminate out-of-plane loss with $|\hat{v}|\Delta t/y_0 < 0.04$, much less than the maximum allowable value of 0.25 suggested by Keane and Adrian [1990], where y_0 is the laser sheet thickness, Δt is the time between images, and $\hat{v}$ is the out-of-plane velocity estimated from the rms velocity fluctuations. The two-dimensionality of the flow in wall parallel planes is verified in Fig. 24 showing the velocity averaged over the streamwise direction and time for $y^+ = 34$. For this plane, the local mean streamwise velocity at a given spanwise location varied from the global mean by no more than 1%. The spanwise variation of velocity is similar at the other wall normal locations.

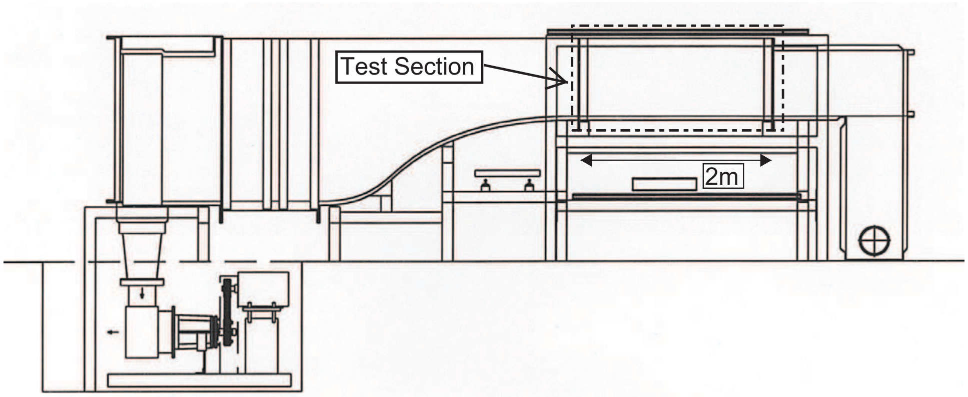
Test Section
2m

(a) Tunnel diagram [Bobba, 2004]

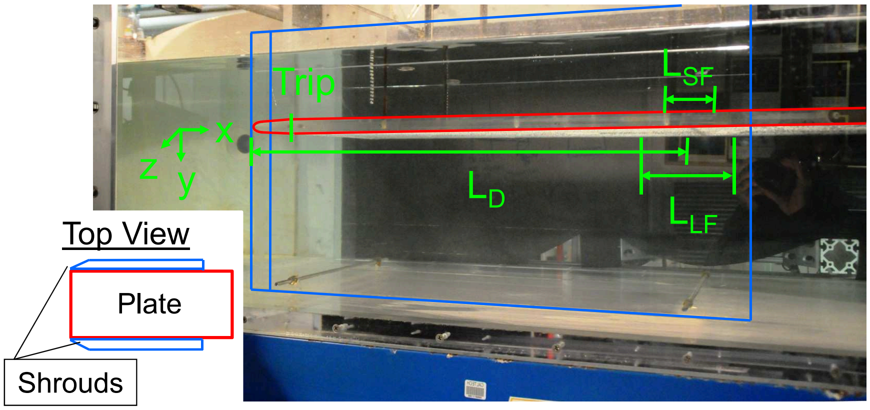
Trip
x
z
y
L_SF
L_D
L_LF
Top View
Plate
Shrouds

(b) Test subsection

Figure 23: (a): Water tunnel schematic showing the location of the test subsection. (b): Photograph of the test subsection; red lines outline the plate and blue lines outline the shroud and its wedge-shaped leading edge. A top-down view is provided in the inset to clarify the shroud orientation.

Table 1: Experimental parameters, spectral measurements

Re_τ	Re_θ	δ	θ	U_∞	u_τ	ν/u_τ	Δy^+	Δt^+
470	1280	13.9mm	1.72mm	0.67m/s	0.03m/s	29.5μm	10.0	0.5

Plane	y^+	y/δ	U^+	U/U_∞	u^+_{rms}	Δx^+, Δz^+	L_x/δ	L_z/δ
1	34	0.07	13.1	0.59	2.10	37.6	9.98	4.91
2	108	0.23	16.4	0.73	1.53	37.1	9.85	4.84
3	278	0.59	20.2	0.90	1.25	37.5	10.03	4.89

5.1.1 Measurements

Wall normal measurements were taken first to characterize the flow at the start of the measurement location using only one camera. The field of view was $50.6mm \times 50.6mm$ ($L_x \times L_y$). Due to camera memory limitations, a maximum of 2048 images could be taken at a time. For collapse of the mean profile, 5 experiments were performed.

For wall parallel measurements, two cameras were placed side-by-side in the streamwise direction with a 10-20 pixel overlap producing a total field of view of approximately $140mm \times 70mm$ ($L_x \times L_z$) with some slight deviation between the three planes investigated. A laser sheet was guided into the test subsection parallel to the flat plate and was centered at locations 1mm, 3.2mm, and 8.2mm from the wall in order to capture spectral information in the near wall, outer log layer, and wake regions of the turbulent boundary layer. For each plane, 40 experiments were performed providing over 80,000 instantaneous realizations allowing collapse of the calculated power spectra. Experimental conditions for this set of experiments are summarized in Table 1.

A second set of wall-parallel measurements were taken at four wall-normal locations independently ranging from y/δ = 0.08–0.48 in order to track coherent structures. Two cameras were placed side-by-side in the streamwise direction to elongate the streamwise field of view. 25 runs of 2048 images were recorded at 2500 Hz, providing 950 eddy turnover times (T_E) of data per point. Additional experimental parameters are provided in Table 2 where Δx and Δz are the vector spacings in the x and z directions, respectively, L_x and L_z are the size of the field of view in the x and z directions, respectively, Δt is the time between images, and T_M is the total measurement time.

Given that most of the swirling coherent structures identified in this study did not extend more than 75–90δ_ν (5–6Δx) in either x or z, the resolution of the equivalent radius, r_{eq} and inclination angle, α, was limited, as will be discussed in Subsection 5.4.2. In addition, the field of view, $L_x/\delta \approx 4.3$ limited the average observation time of a vortex, $T_o = L_x/\overline{U}(y)$ to 5–6.3T_E, with T_o increasing with decreasing y, as will be discussed in Subsection 5.5.2.

Table 2: Experimental parameters for swirling coherent structure experiments

Re_τ	Re_θ	δ(mm)	θ(mm)	U_∞(m/s)	u_τ(m/s)	δ_ν(μm)
410	1085	13.5	1.60	0.63	0.028	32.9

Plane	y^+	y/δ	U/U_∞	Δx^+, Δz^+	L_x/δ	L_z/δ	Δt^+	T_M/T_E
1	33	0.08	0.63	15	4.3	2.2	0.34	950
2	58	0.14	0.69	15	4.3	2.2	0.34	950
3	122	0.30	0.77	15	4.4	2.2	0.34	950
4	198	0.48	0.86	14	4.3	2.1	0.34	950

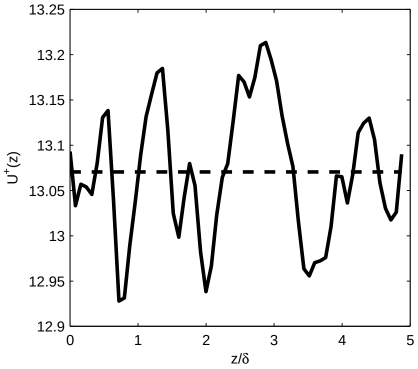

Figure 24: The spanwise variation of the velocity averaged over the streamwise direction and time at $y^+ = 34$

5.1.2 Vector Processing

The velocity field calculations for both the wall normal and wall parallel planes were performed using LaVision's Davis software. In the case of the wall parallel planes, the vector fields were stitched together after processing. To assure an exact overlap of the processed fields, the original images were cropped before processing to ensure overlap of an integer number of interrogation windows after processing. In addition, due to bubbles and particles occasionally aggregating at the wall, for the plane nearest the wall, an average over all images was taken and subtracted from each raw image before vector calculation to reduce the effects of stationary tracers on this calculation.

A 50% overlap of interrogation windows was used to satisfy the Nyquist criterion, which, as will be discussed in Sect. 5.3.1, is necessary to resolve the spectrum properly. The correlation peak fitting was done using a Gaussian three-point estimator in each coordinate direction independently, Whittaker reconstruction was used for image reconstruction, and in-plane particle pair loss was minimized by using a window shift. For wall normal measurements the window size was reduced from 16x16 to 12x12 pixels over two passes and for wall parallel measurements, both passes were performed with a 32x32 pixel window with each camera processed separately. The non-dimensional vector spacing, field size, and wall normal locations are summarized in Tables 1 and 2.

After the initial vector calculation, spurious vectors were removed and replaced via interpolation. In all images, less than 3% of the vectors were removed so the effect of interpolation on the measurements was considered minimal. While the wall normal data was smoothed with a 3x3 filter, no smoothing was performed in wall parallel planes as to preserve the fluctuating velocity signal and spectral shape.

5.2 Flow Properties and Statistics

The mean velocity profile and boundary layer thickness were calculated from the wall normal measurements averaged in the nearly homogeneous streamwise direction, over all frames, and over all experiments. The boundary layer thickness, calculated using the $U(y) = 0.99U_\infty$ criterion, varied by 5% over the 50mm window. The mean profile is compared to the experiments of DeGraaff and Eaton [2000] at a similar Reynolds number ($Re_\theta = \theta U_\infty/\nu = 1430$) in Fig. 25a. θ is the momentum thickness and U_∞ is the free stream velocity.

Since no direct measurements of the wall shear stress were made in this experiment, the friction velocity was calculated from a least squares fit to the predetermined log layer marked with circles in Fig. 25a.

In the wall parallel measurements δ changed by about 10% over the whole field of view. While the outer scale, y/δ, is not constant over the measurement plane, the inner scaled wall distance is nearly constant since u_τ only decreases weakly with streamwise extent. Thus, each plane of the wall parallel data is representative of a particular inner-scaled distance from the wall. Data will also be presented using an averaged outer scale in some cases for convenience.

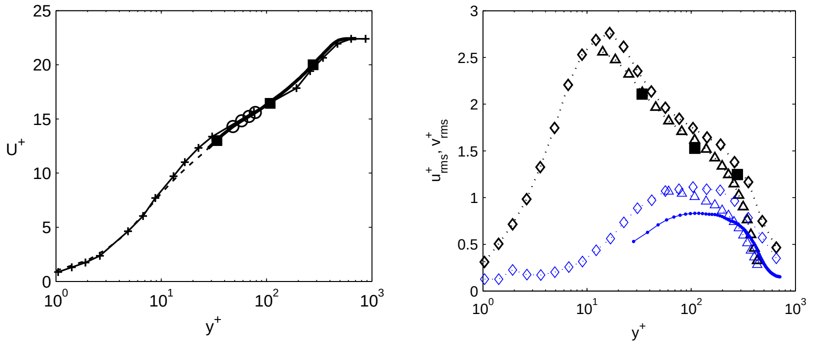

(a) Mean profile **(b)** Streamwise rms fluctuations

Figure 25: In (a): the mean velocity profile is presented where the symbols are —-: Mean profile from wall normal measurements, ■: mean velocity from wall parallel plane measurements, – – –: Spalding fit [Spalding, 1961], –+–: data from DeGraaff and Eaton [2000] at $Re_\theta = 1430$, and ○: points selected to represent the log layer. In (b): black lines and symbols are for u^+_{rms} and blue lines and symbols are for v^+_{rms} where, ■: u^+_{rms} from wall parallel plane measurements, – • –: v^+_{rms} from the wall normal plane measurement, – – ◊ – –: data from DeGraaff and Eaton [2000] at $Re_\theta = 1430$, and – – △ – –: data from Erm and Joubert [1991] at $Re_\theta = 1003$

The rms streamwise velocity fluctuations for each wall parallel plane are presented in Fig. 25b and match closely with the data from DeGraaff and Eaton [2000] and Erm and Joubert [1991]. Any small deviation from the literature values may be from the spatial averaging present in the PIV calculations as discussed in Sect. 5.3.1. The wall normal fluctuations measured in the wall normal plane are also presented for completeness and deviate from the data shown, particularly near the wall. This deviation arises from limited resolution in the wall normal plane and is also observed in the streamwise velocity fluctuations in this plane. As already noted this is not an issue in the wall parallel planes which will be the focus of all discussion from here on.

5.3 Spectral energy distributions

5.3.1 Calculation of the power spectral density in wall parallel planes

The power spectral density is defined as the Fourier transform of the correlation function of the velocity fluctuations, where the relevant non-normalized 3D correlation function is defined in equation 18.

$$R_{u_i u_j}(\rho_x, \rho_z, \tau) = \langle u(x, z, t) u(x + \rho_x, z + \rho_z, t + \tau) \rangle \tag{18}$$

In the above equation, ρ_x and ρ_z are the separation between points in the streamwise and spanwise directions, respectively, τ is a separation in time, the subscripts i and j represent velocity components, and the triangle brackets represent an ensemble average. The Fourier transform pair relating the correlation function to the power spectrum Θ is given in Equations 19 and 20.

$$\Theta_{u_i u_j}(k_x, k_z, \omega) = \frac{1}{(2\pi)^3} \iiint_{-\infty}^{\infty} R_{u_i u_j}(\rho_x, \rho_z, \tau) e^{-i(\rho_x k_x + \rho_z k_z + \tau\omega)} d\rho_x d\rho_z d\tau \tag{19}$$

$$R_{u_i u_j}(\rho_x, \rho_z, \tau) = \iiint_{-\infty}^{\infty} \Theta_{u_i u_j}(k_x, k_z, \omega) e^{i(\rho_x k_x + \rho_z k_z + \tau\omega)} dk_x dk_z d\omega \tag{20}$$

k_x and k_z are the streamwise and spanwise wavenumbers, respectively, and ω is the angular frequency. The Fourier transform pair is defined as above to allow for proper normalization of the spectrum, where the normalization is defined by combining Equations 18 and 20 at zero shift in time and space as given in Equation 21.

$$R_{u_i u_j}(0,0,0) = \langle u_i u_j \rangle = \iiint_{-\infty}^{\infty} \Theta_{u_i u_j}(k_x, k_z, \omega) dk_x dk_z d\omega \tag{21}$$

In practice, the auto-spectrum is calculated as the square magnitude of the finite Fourier transform of the velocity fluctuations and is normalized using Equation 21.

2D spectra can be calculated by integration of the 3D spectrum over one dimension as shown in Equation 22 (where the limits are finite in practice), or by calculating the finite Fourier Transform of a 2D subset of the original 3D sample records and taking an ensemble average over all subsets.

$$\Phi_{u_i u_j}(k_1, k_2) = \int_{-\infty}^{\infty} \Theta_{u_i u_j}(k_1, k_2, k_3) dk_3 \tag{22}$$

k_1, k_2, and k_3 are any three wave vectors. Similarly, 1D spectra can be calculated as the integral of a 2D spectrum or by using a 1D subset of the original 3D dataset and ensemble averaging over all subsets.

As discussed by Adrian [1988], the velocity measured by the PIV algorithm, $\tilde{U}_i(x,y,z,t)$, is not the velocity at a single point in the flow, $U_i(x,y,z,t)$, but the velocity signal averaged over the laser sheet thickness (~1mm) and convolved with a rectangular window, $h(x,z)$, which represents the averaging effect of an interrogation window. The relation between the measured and the true velocity is given in Equation 23 and the measured fluctuating velocity is defined in Equation 24.

$$\tilde{U}_i(x,y,z,t) = \left[\int_{y-y_0/2}^{y+y_0/2} U_i(x,y',z,t)dy' \right] \star h(x,z) \tag{23}$$

$$\tilde{u}_i(x,y,z,t) = \tilde{U}_i(x,y,z,t) - \overline{\tilde{U}}_i(y) \tag{24}$$

U is the instantaneous velocity, u is the fluctuating velocity, the star represents convolution, and the overbar indicates an average over all space, time, and experiments that closely approximates the true mean as discussed by Tomkins and Adrian [2005].

The spatial averaging from the interrogation window, h, greatly attenuates fluctuations smaller than two window widths, and will also attenuate scales near this limit to a lesser extent. This, then, leads to an attenuation of the measured mean square fluctuations and the velocity spectrum.

When considering the measured velocity signal, $\tilde{u}$, given in Equation 24, a different spectrum will result. The square magnitude of the Fourier transform of Equation 24 is given in Equation 25, where the convolution theorem has been used to separate out the effects of smoothing from the interrogation window.

$$\begin{gathered} \tilde{\Theta}_{u_i u_j}(k_x, k_z, \omega) = \Theta_{u_i u_j}(k_x, k_z, \omega)\Gamma(k_x, k_z) \\ \Gamma(k_x, k_z) = sinc^2\left(\frac{W_x}{2}k_x\right) sinc^2\left(\frac{W_z}{2}k_z\right) \end{gathered} \tag{25}$$

$\tilde{\Theta}$ is the 3D power spectrum of the measured velocity signal, Γ is the square magnitude of the Fourier transform of the rectangular window, h, and W is the PIV interrogation window size in either x or z as denoted by the subscript. The measured spectrum, $\tilde{\Theta}$, should be normalized by the measured mean square value of the velocity fluctuations, which is the mean square value of the fluctuations defined in Equation 24.

The effect of Γ is to attenuate the spectrum, particularly at high wavenumbers, where the amplitude of Γ goes to zero at $k = 2\pi/W$. Since Γ is known, one could recover the original spectrum, Θ simply by dividing by

Γ, although, in practice, this does not work where Γ approaches zero. As noted by Foucaut et al. [2004], the attenuation become significant (more than 50% attenuation) above a wavenumber $k_{cut} = 2.8/W$. Following their criterion, all data beyond this cutoff will be ignored.

Since the experimental data is not periodic and of finite length, the data is windowed prior to calculating the Fourier transform to prevent spectral leakage. A 3D Hanning window, an extension of the 2D Hanning window used by Tomkins and Adrian [2005], is used here. With the current data, the effect of leakage is most prevalent at the low frequency end of the spectrum. Multiplying the measured signal by the 3D Hanning window, denoted by g, provides an estimate of the spectrum as presented in Equation 26.

$$\hat{\tilde{\Theta}}_{u_i u_j}(k_x, k_z, \omega) = \Big[\left[(U_i H) \star G \right] \left[(U_j^* H^*) \star G^* \right] \Big] \tag{26}$$

The hat indicates that this is an estimate of the spectrum since the signal is windowed and of finite length, the capital letters are the finite Fourier transform of the corresponding lower case quantity where $UU^* = \Theta$, $HH^* = \Gamma$, and the asterisk represents the complex conjugate. Estimates of the 2D and 1D spectra can be calculated as before and the mean square fluctuations are the same as for the non-windowed data using a proper weighting of the windowing function.

The division of this estimate of the spectrum by Γ to correct the high wavenumber range gives a reasonable estimate of the true spectrum since the convolution with G in spectral space mainly affects the low frequency/wavenumber range. The same operations were performed by Tomkins and Adrian [2005]. In presenting the spectra, both the corrected form (divided by Γ) and the uncorrected form will be shown to illuminate the effects of this correction.

To avoid spatial aliasing, interrogation windows with 50% overlap were used which attenuate aliased energy content above the Nyquist frequency. To avoid temporal aliasing, the data was oversampled during recording, low pass filtered, and then subsampled before calculating the spectrum as discussed by Wernet [2007]. The low pass filter cutoff for the time signal is set so that $\omega_{cut} = \overline{U}(y) k_{cut}$.

To summarize, small scale features of the flow are attenuated by the averaging over the PIV interrogation window and large scale features are smoothed out by spectral leakage. To account for these issues and prevent aliasing, the data is recorded at a higher sampling rate than necessary and the vector fields are calculated using 50% overlap of the interrogation windows. Before any calculations are performed, the data is low pass filtered in time to get rid of unwanted noise. Prior to calculation of the spectrum, the signal is split into subsets (split twice in z and thrice in time with each region overlapping by 50%) and windowed using a Hanning window to help reduce spectral leakage. Finally, the finite Fourier transform of each subset is calculated, all calculations are averaged, and the data is divided by the smoothing function Γ to get an estimate of the true spectrum Θ where data beyond the cutoff in k_x and k_z is ignored. 1D and 2D spectra are calculated by integration of the resulting 3D spectrum.

5.3.2 Spectral symmetries

We present here a discussion of the symmetries present in the 1D, 2D, and 3D streamwise velocity spectra and the proper normalization of each before moving on to present the 1D, 2D, and 3D spectra calculated from the PIV measurements. Due to a lower than desirable dynamic range of the spanwise velocity fluctuations, neither the spanwise velocity spectrum nor the streamwise-spanwise velocity cross-spectrum will be presented here. For this reason, in the remainder of this document, the $u_i u_j$ subscript for the spectra will be dropped since all spectra will be streamwise velocity spectra.

The 3D auto-spectrum is even and real which provides symmetry about any coordinate plane if the spectrum is rotated by 180° about the origin, and thus only 4 independent octants exist. Similarly, all 2D spectra are even and real with rotational symmetry about the origin, and thus have only 2 independent quadrants each. Therefore, any 2D spectra can be represented by any half plane and the 3D spectrum by any 4 connected octants. In this half space representation, the magnitude of the spectra are doubled to conserve energy. The 2 non-redundant quadrants of each 2D spectrum are shown in Figs. 26a, 26b, and 26c and the four non-redundant octants (choosing $\omega > 0$) of the 3D spectrum are shown in Fig. 27 for one wall normal location.

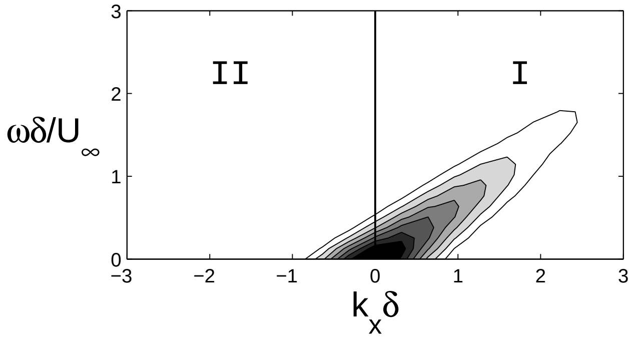

(a) $\Phi(k_x, \omega)$

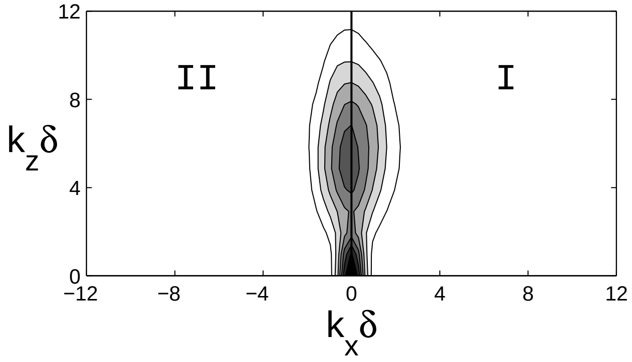

(b) $\Phi(k_x, k_z)$

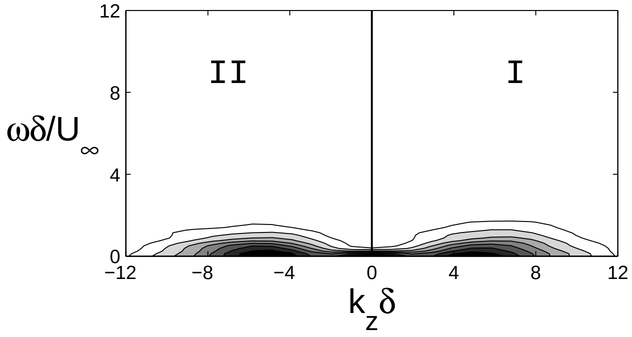

(c) $\Phi(k_z, \omega)$

Figure 26: The panels show the half space representation of each 2D spectrum at $y^+ = 108$. The spectra at other wall normal locations are qualitatively similar. The levels shown are from 20% to 80% of the maximum energy in 10% increments moving from light to dark shades

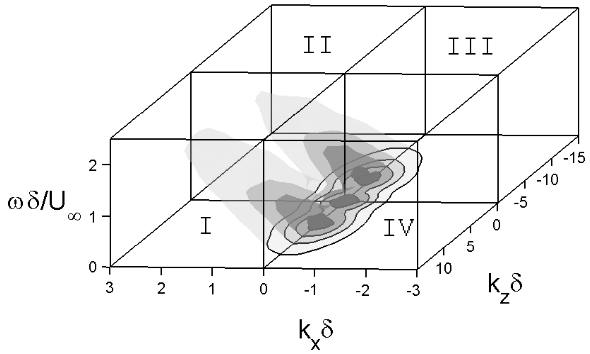

Figure 27: The half space representation of $\Theta(k_x, k_z, \omega)$ at $y^+ = 108$ is shown, where the spectra in other planes are qualitatively similar. The levels are from 15% to 75% of the maximum energy in 20% increments moving from light to dark shades. The intersection of the spectrum with $\omega = 0$ is denoted by solid black lines to better illuminate the shape of the spectrum

From Figs. 26b and 26c only a very slight asymmetry is noted in k_z which arises from poorer resolution in this direction as well as slight tilting of the PIV cameras, although some corrections have been made for the latter. For all practical purposes, these spectra are symmetric in k_z. For $\Phi(k_z, \omega)$ this symmetry arises since there is no mean spanwise flow and thus no spanwise directional preference. For $\Phi(k_x, k_z)$ there should physically be no distinction between the positive and negative wavenumber pairs. Thus, both of these spectra can be represented in one quadrant with the magnitude doubled to conserve energy.

For $\Phi(k_x, \omega)$ the two quadrants are not equivalent, where quadrant I is interpreted as downstream traveling waves and quadrant II as upstream traveling waves. The amount of energy in quadrant II is not negligible (at $y^+ = 108$ quadrant II represents about 12% of the total area under the spectrum) as originally suggested by Morrison and Kronauer [1969], and it is necessary to use both planes when integrating $\Phi(k_x, \omega)$ to recover $\phi(k_x)$, $\phi(\omega)$, or any other integral quantities, otherwise a low wavenumer spectral distortion will result.

For the 3D spectrum shown in Fig. 27, the same symmetry exists in k_z and the same asymmetry exists in k_x as might be expected from the 2D spectral plots. Thus, the spectrum can be represented by the two octants covering all k_x and positive k_z and ω with the magnitude doubled to preserve the normalization as given in Equation 27.

$$\begin{aligned}\overline{u^2} &= \iiint_{-\infty}^{\infty} \Theta(k_x, k_z, \omega) dk_x dk_z d\omega = 4 \iiint_{0}^{\infty} \left[\Theta(k_x, k_z, \omega) + \Theta(-k_x, k_z, \omega)\right] dk_x dk_z d\omega \\ &= 4 \iiint_{-\infty}^{\infty} k_x k_z \omega \left[\Theta(k_x, k_z, \omega) + \Theta(-k_x, k_z, \omega)\right] d\ln k_x \, d\ln k_z \, d\ln \omega\end{aligned} \tag{27}$$

While the energy in the upstream traveling waves is non-negligible and must be included for proper normalization of $\Theta(k_x, k_z, \omega)$, it is customary in the literature to only plot data for positive streamwise wavenumber, k_x, when these spectra are presented in pre-multiplied form. While this may seem wrong at first, when premultiplied and presented in log coordinates, the energy in the first decade, which encompasses the upstream traveling waves, is spread out while the remaining 80% of the energy in the second decade is concentrated and, when considering absolute energy levels, appears much more energetic. Therefore, for the energy levels shown in the following figures, the upstream traveling waves do not appear so plots are presented over positive k_x only.

5.3.3 1D Spectra

Figs. 28a, 28c, and 28e show the 1D premultiplied streamwise velocity spectrum over streamwise wavenumber, spanwise wavenumber, and frequency, respectively, for the uncorrected data. The corrected data is shown

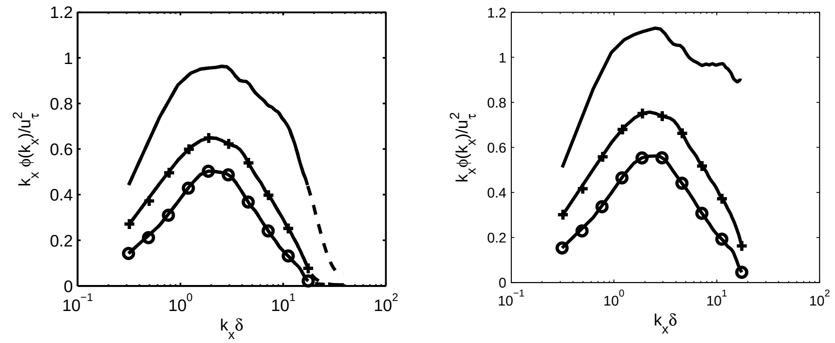

(a) $k_x\phi(k_x)$ **(b)** $k_x\phi(k_x)$

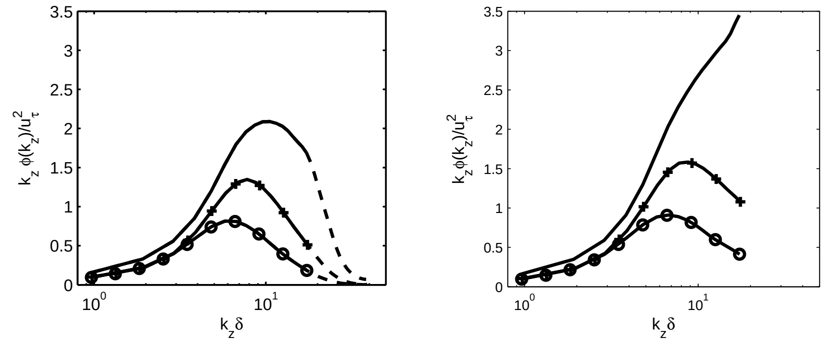

(c) $k_z\phi(k_z)$ **(d)** $k_z\phi(k_z)$

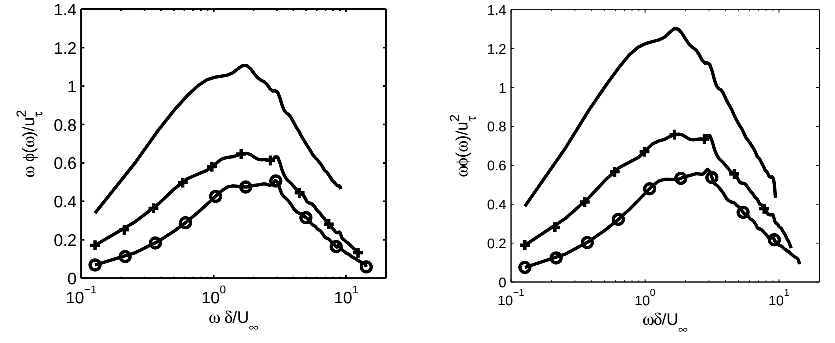

(e) $\omega\phi(\omega)$ **(f)** $\omega\phi(\omega)$

Figure 28: 1D premultiplied streamwise velocity spectra over (a,b): streamwise wavenumber, (c,d): spanwise wavenumbers, and (e,f): frequency where the lines are in all cases —-: $y^+ = 34$, − + −: $y^+ = 108$, − ○ −: $y^+ = 278$. The uncorrected data is shown in the left column and the corrected data is in the right column. For the uncorrected data, the dashed lines indicate data beyond the imposed cutoff, k_{cut}, beyond which the data begins to be attenuated

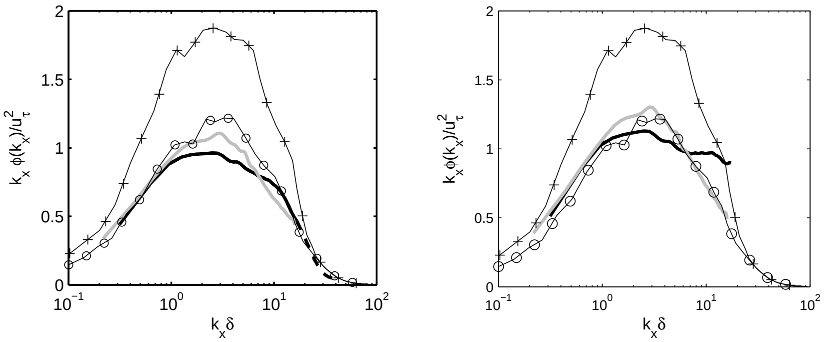

(a) $y^+ = 34$, $y/\delta = 0.07$ **(b)** $y^+ = 34$, $y/\delta = 0.07$

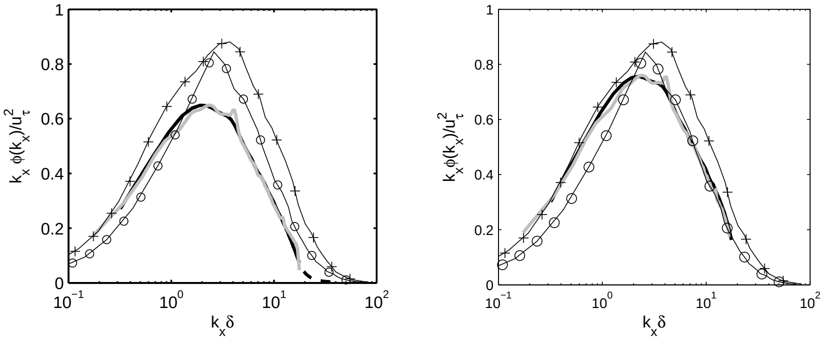

(c) $y^+ = 108$, $y/\delta = 0.23$ **(d)** $y^+ = 108$, $y/\delta = 0.23$

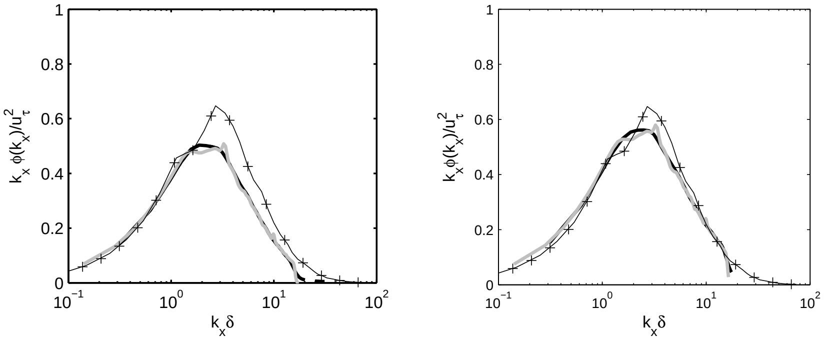

(e) $y^+ = 278$, $y/\delta = 0.59$ **(f)** $y^+ = 278$, $y/\delta = 0.59$

Figure 29: The streamwise wavenumber and frequency spectra are compared where the colors are black: $k_x\phi(k_x)$, gray: Taylor conversion of $\omega\phi(\omega)$. The uncorrected data is shown in the left and the corrected data is on the right. For the uncorrected data, the dashed lines indicate data beyond the imposed cutoff, k_{cut} beyond which the data begins to be attenuated. Data from Erm and Joubert [1991] at $Re_\theta = 1020$ is represented by symbols where the wall normal locations are (a,b): $y/\delta = 0.04(+), 0.1(\circ)$, (c,d): $y/\delta = 0.2(+), 0.35(\circ)$, and (e,f): $y/\delta = 0.55(+)$

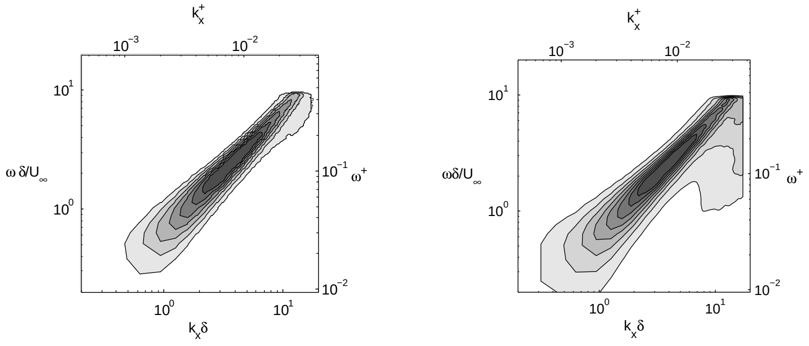

(a) $y^+ = 34$ **(b)** $y^+ = 34$

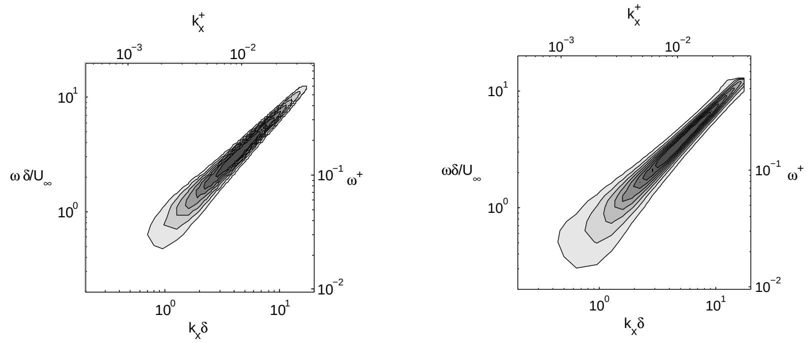

(c) $y^+ = 108$ **(d)** $y^+ = 108$

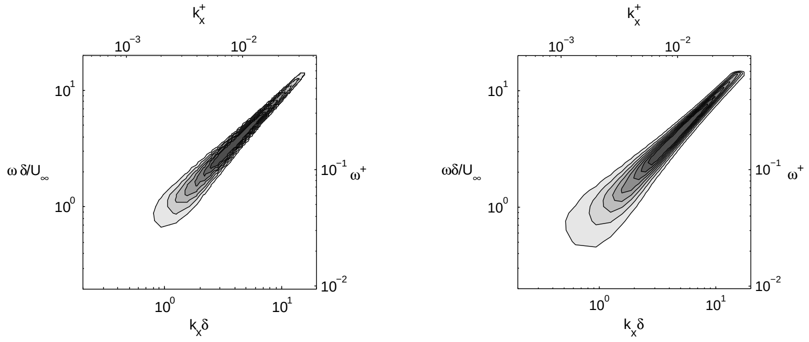

(e) $y^+ = 278$ **(f)** $y^+ = 278$

Figure 30: $k_x\omega\Phi(k_x, \omega)$ is presented for all three planes. The uncorrected data is presented in the left column and the corrected data is in the right column. For each plot, the contours represent 20% to 80% of the maximum energy of the spectrum moving from lighter to darker shades in 10% increments

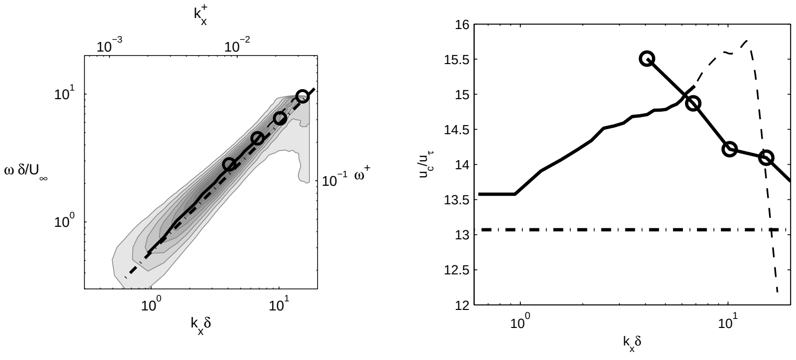

(a) **(b)**

Figure 31: (a): The convection velocity calculated by finding the line of local maxima along $k_x\omega\Phi(k_x,\omega)$ at $y^+ = 34$ is indicated by the solid black line (dashed black line beyond the point where noise influences the calculation) and displayed on top of the spectrum where the contours represent 20% to 80% of the maximum energy of the spectrum moving from light to dark shades in 10% increments. The dash-dot line indicates where $\omega = \overline{U}k_x$ signifying a convection velocity equal to the local mean. The four open circles are data from Krogstad et al. [1998] at the same y^+ and similar Reynolds number. This data was converted from its original form, convection velocity plotted against streamwise probe separation, by converting the separation to a wavenumber and using the convection velocity for each wavenumber to define an associated frequency. (b): The convection velocity is plotted as a function of wavenumber where the lines and symbols are the same as in (a)

in Figs. 28b, 28d, and 28f for comparison. The peak in the spectrum over spanwise wavenumber moves to lower k_z (larger spanwise scales) when moving away from the wall indicating that the signature of the dominant scales is growing in spanwise extent in this direction. This has also been shown in the channel flow computations of Jiménez et al. [2004] and boundary layer experiments of Tomkins and Adrian [2005], among others. In the present data, as the peak moves to higher k_z closer to the wall, a larger energetic portion of the spectrum is cut off by spatial averaging. In fact, at $y^+ = 34$ a better resolution would be required to resolve the peak in the spectrum over spanwise wavenumbers. Therefore, any integral quantities in the z direction, including the rms velocity fluctuations and spectra, will be more in error as the wall is approached. This is likely the reason for the slight underestimation of u_{rms} at $y^+ = 34$ shown in Fig. 25b.

In Fig. 29, the 1D spectra over frequency and over streamwise wavenumber are compared to one another using Taylor's hypothesis and to the hotwire measurements of Erm and Joubert [1991] at a similar Reynolds number and comparable wall normal locations. The 1D spectra are in fair agreement with the data of Erm and Joubert [1991], and this agreement is improved when the data is corrected as shown in the plots in the right column of Fig. 29. This improved agreement with the corrected 1D spectra should also be indicative of a proper correction for the 2D and 3D spectra as the correction is applied to the 3D spectrum and all other spectra are calculated via integration of this spectrum. The only major deviation between the temporal and spatial spectra is at $y^+ = 34$. This deviation may be indicative of the variation of the convection velocity of scales from the local mean, although noise may also be contributing to this variation, particularly at the high k_x end, as shown in the 2D spectra in Sect. 5.3.4. Some error may be expected at this wall normal location since there is a slight deviation of the mean velocity profile from the measurements of DeGraaff and Eaton [2000] as shown in Figure 25a, and thus other statistics may be adversely affected. For the other two planes, there is almost no deviation between the spatial and Taylor converted temporal spectra, indicating that the frozen flow assumption should hold at these locations.

5.3.4 2D Spectra

The 2D premultiplied $\Phi(k_x,\omega)$ streamwise velocity spectra, i.e. $k_x\omega\Phi(k_x,\omega)$, are shown for each plane in Fig. 30 with the uncorrected data in the left column and the corrected data in the right column. Note that

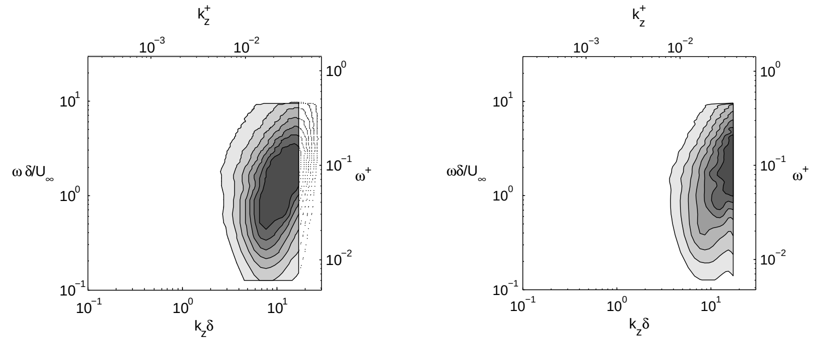

(a) $y^+ = 34$ **(b)** $y^+ = 34$

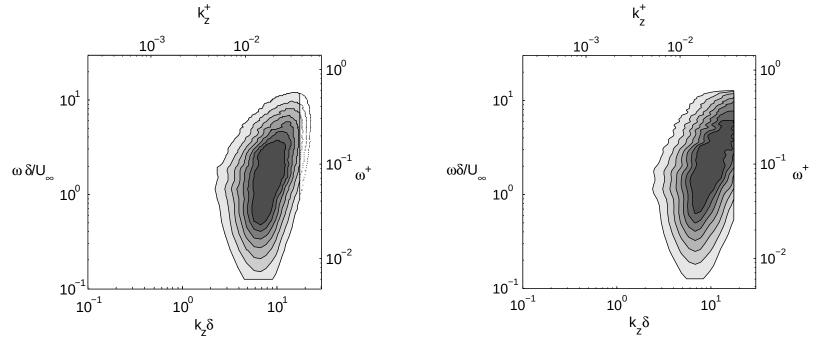

(c) $y^+ = 108$ **(d)** $y^+ = 108$

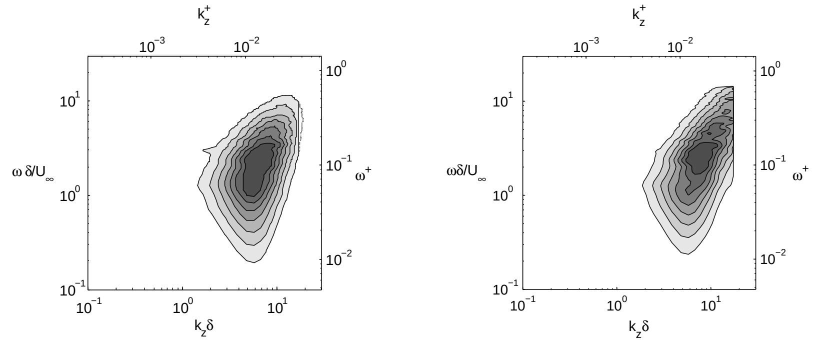

(e) $y^+ = 278$ **(f)** $y^+ = 278$

Figure 32: $k_z \omega \Phi(k_z, \omega)$ is presented for all three planes where the contours represent 20% to 80% of the maximum energy of the spectrum moving from light to dark shades in 10% increments. The uncorrected data is presented in the left column and the corrected data is in the right column. For the uncorrected data, the unshaded contours are regions of the spectrum beyond the streamwise and spanwise cutoff, k_{cut}, that may be irregularly shaped due to spectral attenuation, but are included for visualization

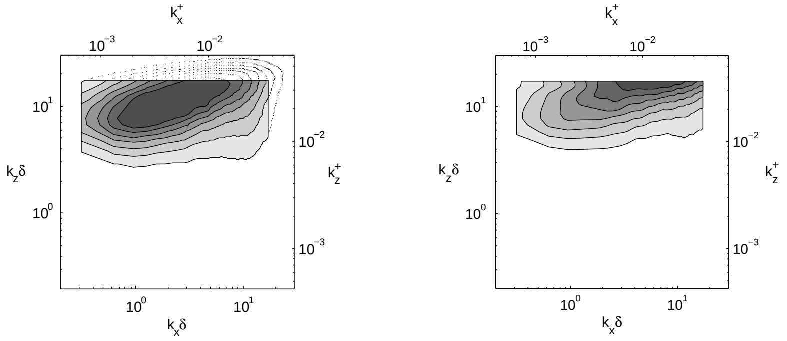

(a) $y^+ = 34$ **(b)** $y^+ = 34$

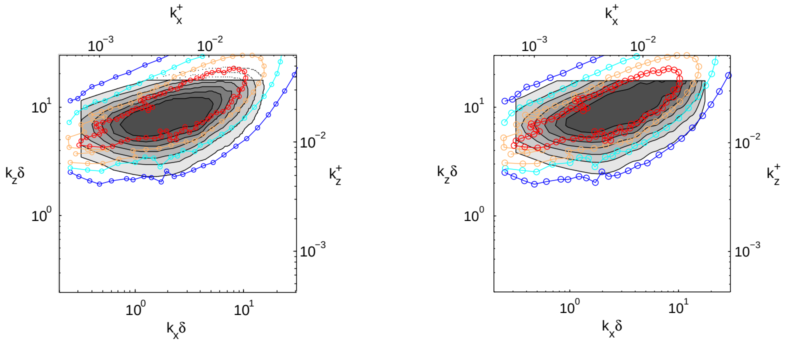

(c) $y^+ = 108$ **(d)** $y^+ = 108$

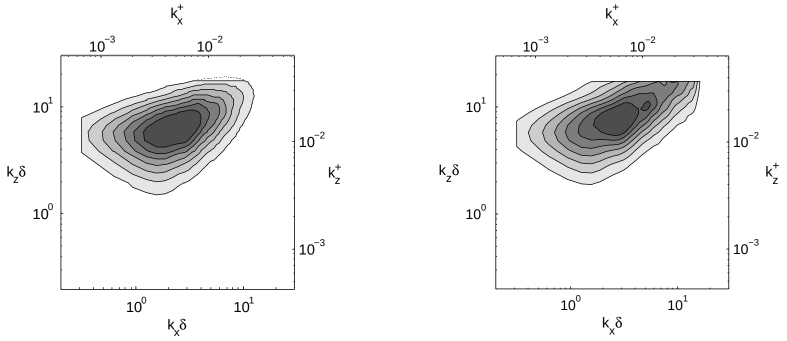

(e) $y^+ = 278$ **(f)** $y^+ = 278$

Figure 33: $k_x k_z \Phi(k_x, k_z)$ is presented for all three planes where the contours represent 20% to 80% of the maximum energy of the spectrum moving from light to dark shades in 10% increments. The uncorrected data is presented in the left column and the corrected data is in the right column. For the uncorrected data, the unshaded contours are regions of the spectrum beyond the streamwise and spanwise cutoff, k_{cut}, that may be irregularly shaped due to spectral attenuation, but are included for visualization. Linearly spaced spectral contours from del Álamo and Jiménez [2001] for a channel flow computation at $Re_\tau = 550$ at $y^+ = 90$ are shown with colored circles where cool colors indicate less energetic portions of the spectrum. This is compared to the current data in (c) and (d) to show the validity of the correction

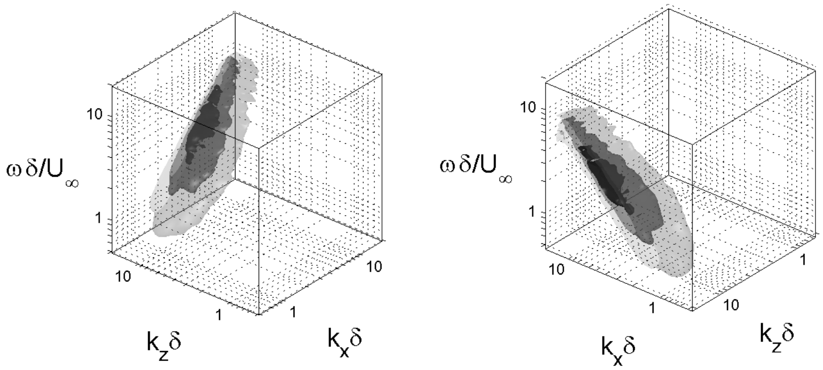

(a) $y^+ = 34$ **(b)** $y^+ = 34$

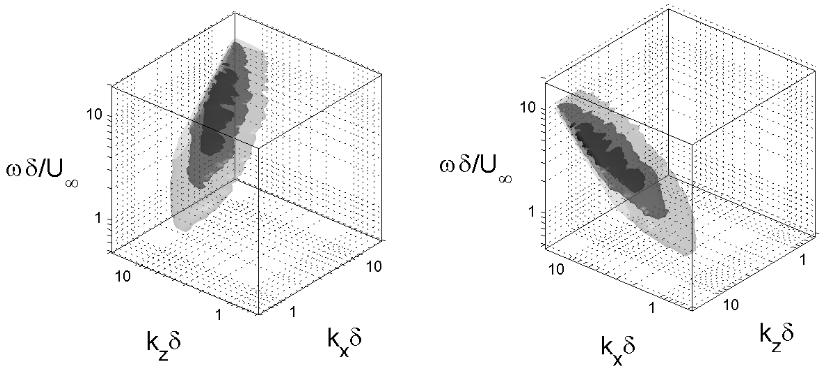

(c) $y^+ = 108$ **(d)** $y^+ = 108$

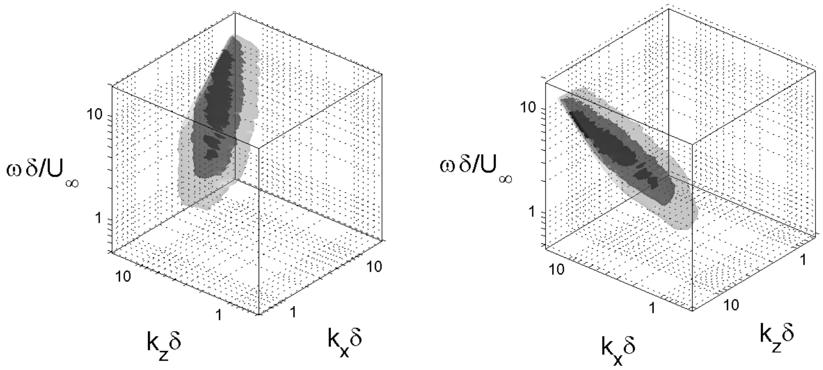

(e) $y^+ = 278$ **(f)** $y^+ = 278$

Figure 34: $k_x k_z \omega \Theta(k_x, k_z, \omega)$ is presented at each wall normal location. The surfaces represent 25%, 50%, and 75% of the total energy in each spectrum moving from light to dark shades. The left and right columns offer two different views. Data beyond the k_x and k_z cutoffs are not shown

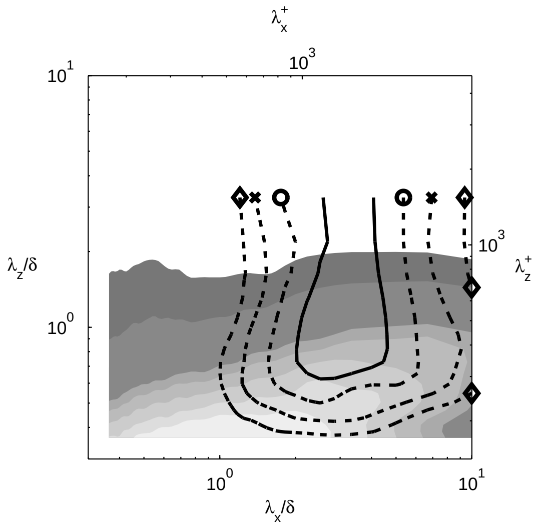

Figure 35: The contour lines represent the convection velocity at $y^+ = 34$ using the method outlined in Equation 28 where solid contours denote a convection velocity equal to the local mean and dotted contours with symbols are convection velocities below the local mean with o: $\overline{U}^+ - u_\tau$, x: $\overline{U}^+ - 2u_\tau$, and ◊: $\overline{U}^+ - 3u_\tau$. The shaded contours represent 20 to 80% of the maximum energy of $k_x k_z \Phi(k_x, k_z)$ in 10% increments moving from light to the dark shades

in the 1D spectra of Fig. 28, the maximum energy of each spectrum decreases as measurements are taken further from the wall, as expected. In the 2D plots here and 3D plots to follow, contour levels represent a fraction of the maximum energy of each individual spectrum so this variation will not be present. Also, note that the total energy of a spectrum is different before and after correction, so the levels shown for the uncorrected spectra do not represent the same levels shown for the corrected spectra.

One notable difference between the corrected and uncorrected $k_x \omega \Phi(k_x, \omega)$ is the apparent noise that appears in the corrected spectrum in the range of $7 < k_x\delta < 20$ and $1 < \omega\delta/U_\infty < 9$. In this same high wavenumber range, there is a discrepancy between the spatial and temporal 1D spectrum as shown in Fig. 29a and more prevalently in the corrected spectrum in Fig. 29b where the amplitude of the spatial spectrum exceeds the temporal spectrum. Since the 1D temporal and streamwise wavenumber spectra should agree for the nearly homogeneous small scales, the discrepancy beyond $k_x\delta = 7$ likely comes from noise. It is hypothesized that this noise in the near wall plane is from the measurement of nearly stationary particles or bubbles that clustered near the surface and were illuminated by the laser sheet during PIV acquisition.

From $\Phi(k_x, \omega)$, a convection velocity can be calculated for each streamwise scale as shown in Fig. 31. The method of finding the ridge line, the line of maxima along the spectrum as outlined by Goldschmidt et al. [1981], is used here where the convection velocity is then defined as ω/k_x along the ridge line (the solid line in the Fig. 31). For the plane shown at $y^+ = 34$, it is apparent that most scales travel faster than the local mean velocity. This is in fair agreement with Krogstad et al. [1998], whose data from hotwire measurements is presented for comparison. The discrepancy beyond $k_x\delta = 7$ may again be affected by the noise in this region as described previously, and for this reason data beyond this point in Fig. 31 has been denoted by a dashed line. In addition, the slow convection velocities for low wavenumbers reflects the lack of scale separation at this low Reynolds number, namely the dominance of the near-wall structures over the superstructures which are centered at locations further from the wall but inhabit a similar wavenumber range.

Premultiplied $\Phi(k_z, \omega)$ and $\Phi(k_x, k_z)$ are shown for each plane in Figs. 32 and 33, respectively. The uncorrected data is shown in the left column and the corrected data is shown in the right column. In addition, data from the channel flow computations presented by del Álamo and Jiménez [2001] at $y^+ = 90$ and $Re_\tau = 550$ are included for comparison to the current data at $y^+ = 108$ to validate the correction applied (some differences are expected due to the difference in geometry between these two flows as well as the slight difference in

Reynolds number and wall normal location). The correction appears to push the spectral peak in the right direction and align the current data to the data from del Álamo and Jiménez [2001]. The dotted contours for the uncorrected data show the region that is beyond the wavenumber cutoff and again shows that the resolution in z is not sufficient to resolve the peak in the spanwise direction at $y^+ = 34$. Again, the correction pushes the peak in the spectra to higher k_z and increases the energy in the spectra in general near this cutoff. Upon integration in k_z, the resulting corrected 1D spectra will have a higher level throughout than the uncorrected spectra, as evidenced in the $\phi(k_x)$ and $\phi(\omega)$ plots in Fig. 29.

$\Phi(k_x, k_z)$ shows some variability between the three planes becoming less elongated in streamwise wavenumber further from the wall as shown in Figs. 33a, 33c, and 33e. The range of energetic streamwise scales narrows while the range of spanwise scales remains fairly constant moving further from the wall leading to a more homogeneous distribution of the energy in the wake region.

Note that all 2D spectra show that the range of streamwise scales becomes smaller and the larger streamwise scales become less dominant beyond the log layer. Recall, that these conclusions are drawn upon low Re data so the scale separation is not large, yet this conclusion about the change in scale size from the inner layer to the wake region should apply to higher Reynolds number data. This illustrates the difficulty in performing PIV in planes near the wall as the range of energetic scales is broader and large scales play a more dominant role. Thus, both a very large field of view and a very fine resolution are needed, which was difficult to achieve in the current experiment. The best solution is to analyze both a large field to obtain the large scale features and a small, well resolved, field from which a composite spectrum can be produced covering the whole wavenumber range, which is the focus of future experiments.

5.3.5 3D Spectra

Finally, two views of the 3D premultiplied streamwise velocity spectra, $k_x k_z \omega \Theta(k_x, k_z, \omega)$, are presented in each wall parallel plane in Figs. 34a to 34f for the corrected data. The uncorrected data has been omitted since differences between the two are already clearly outlined by the 2D spectra in Sect. 5.3.4. The cutoff of each spectrum is clearly shown here, and the effect of this cutoff on all of the spectra presented so far can easily be understood by considering an integration in one or more coordinate directions.

These three-dimensional spectra show not only the energy distribution over all scales, but over all scales traveling at all velocities, where the convection velocity of a scale is defined as $u_{c,x} = \omega / k_x$. In this framework, if the flow is decomposed into traveling waves as in the model of McKeon and Sharma [2010], then the spectra are the footprints of these waves at particular wall normal locations. For flow control applications, measurements taken at several wall normal locations would provide a well characterized response of the boundary layer to a periodic excitation (as studied in Jacobi et al. [2010] and Jacobi and McKeon [2011] using hotwires) and alterations of the spectra could be used to see how a particular input restructures the flow. Such information could be used for optimal control design.

To gain insight into the convection velocity of different scales in the flow, a single convection velocity can be calculated for each streamwise and spanwise scale pair from the three-dimensional spectra using equation 28 from del Álamo and Jiménez [2009] and used in earlier works by Jiménez et al. [2004] and Flores and Jiménez [2006].

$$u_c(k_x, k_z, y) = \frac{1}{k_x} \frac{\int_{-\infty}^{\infty} \omega \Theta(k_x, k_z, \omega, y) d\omega}{\int_{-\infty}^{\infty} \Theta(k_x, k_z, \omega, y) d\omega} \tag{28}$$

This convection velocity definition uses a value of ω that is weighted by the 3D streamwise velocity spectrum. In this way, it gives the dominant convection velocity for each streamwise-spanwise scale pair. A map of the convection velocity is presented in Fig. 35 where lines of constant convection velocity are plotted on top of $k_x k_z \Phi(k_x, k_z)$ to highlight the convection velocity of the most energetic scales. From this chart, it is apparent that most scales at $y^+ = 34$ travel slower than the local mean except for the large scales in the range $2 < \lambda_x / \delta < 5$. This differs from the trend in Fig. 31 where almost all scales recovered traveled faster than the local mean. This difference may be expected as the method of calculating the convection velocity differs between the two figures where one searches for a maximum (method for Fig. 31) while the other looks for a “center of mass” (method for Fig. 35). Also, the noise that exists over a range of ω as well as the cutoff imposed in ω will manifest itself differently when using an integral method such as Equation 28. An investigation of such convection velocity maps, as well as the definition of convection velocities in general, is a subject of future work.

5.4 Identification of swirling coherent structures

5.4.1 SCS identification technique

The identification of swirling coherent structures (SCS), that is, coherent structures identified by regions of swirling flow in wall-parallel planes which could be interpreted as wall-parallel cuts through coherent, three-dimensional hairpin vortices, are discussed here. Many methods have been proposed for identifying vortices, and subsequently SCS, but as discussed by Jeong and Hussain [1995], most simple intuitive measures fail to identify these structures correctly. In order to identify vortex cores in a Galilean invariant setting, methods including the Δ [Chong et al., 1990], Q [Hunt et al., 1988], λ_2 [Jeong and Hussain, 1995], and swirling strength ($\lambda_{c,i}$) [Zhou et al., 1999] criteria have been proposed, as summarized in the reviews of Jeong and Hussain [1995] and Chakraborty et al. [2005]. These methods generally provide different results in a 3D flow field, but in an incompressible flow in a 2D plane, as studied here, all of the criteria give identical results.

In the current study, the wall-normal component of the swirling strength, given in Eqn. 29 for a 2D2C wall-parallel measurement, was used for SCS identification, where the subscripts x and z represent derivatives in x and z, respectively, of the instantaneous streamwise, U, and spanwise, W, velocity. We follow the convention that $U = u + \overline{U}$, (and similarly for W) where U is the instantaneous velocity, u is the fluctuating velocity, and $\overline{U}$ is the mean velocity averaged in the homogeneous spanwise direction, nearly homogeneous streamwise direction, and time, and thus is only a function of the wall-normal distance.

$$\lambda_{c,i}(x,z) = \left| Im\left[\sqrt{(U_x + W_z)^2 + 4(U_x W_z - U_z W_x)}\right]\right| \tag{29}$$

A signed swirling strength was also used to identify the direction of swirl. This is calculated by multiplying $\lambda_{c,i}$ by the sign of the wall-normal vorticity, as in Natrajan et al. [2007].

To reduce the noise in the numerical derivatives needed to calculate $\lambda_{c,i}$, the velocity field was convolved with a smoothing kernel before differentiation. Three different types of smoothing were investigated including: (1) A moving average filter with no weighting, (2) a moving average filter with Gaussian weighting, and (3) the Savitzky-Golay (SG) filter where the calculation of this filter and the smoothing kernels used are documented in Savitzky and Golay [1964]. To compare these filters and chose the best filter size, 5 x 5, 7 x 7, and 9 x 9 smoothing kernels of each filter type were tested on a subsubsection of the flow field. The Gaussian weighted average as well as the SG filter performed better than the simple moving average as they both smoothed the velocity field while keeping nearby cores separate. Of the two, the SG filter (with a quadratic polynomial) was chosen with a 7 x 7 kernel size, as it allowed derivatives to be calculated simply. A sample velocity field, with the signed swirling field overlaid, is shown in Fig. 36. Note that while smoothing is necessary to reliably extract SCS from the velocity fields, the accuracy with which the properties of the SCS can be measured is reduced as the signal is smeared out in a $3\Delta x$ radius ($45\delta_\nu$) about a given point using the 7 x 7 smoothing kernel.

From the continuous swirl field, individual SCS were identified by extracting regions where $\lambda_{c,i} > \lambda_{rms}$, the rms swirling strength, which can be considered a measure of background noise. This threshold was also considered by Wu and Christensen [2006], although they found a more stringent threshold of $\lambda_{c,i} > 1.5\lambda_{rms}$ separated vortex cores better for their measurements in the wall-normal plane. For the sake of tracking SCS (to be described in Subsection 5.5), SCS bounded by a box of size less than 2 vector spacings in the streamwise or spanwise direction were neglected. These small SCS were generally found to be energetically insignificant and would often disappear from one timestep to the next, which indicates that they likely arose from noise in the swirl calculation.

One interpretation of persistent SCS is the wall-parallel signature of circular vortex tubes, perhaps tilted with respect to the downstream direction and possibly consistent with the footprint of hairpin vortices. In

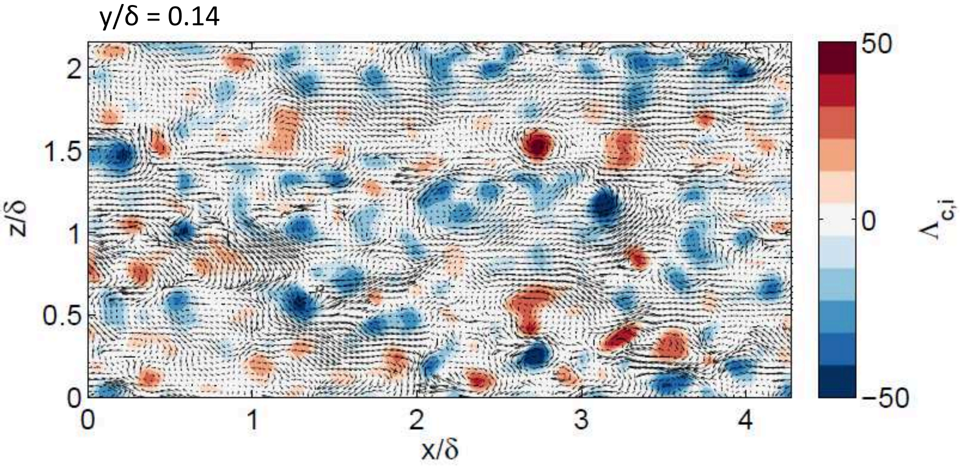

Figure 36: Clockwise (red) and counter-clockwise (blue) swirling motions are presented on top of a velocity field with the mean velocity subtracted, shown by the black vectors, at y/δ = 0.014 at one point in time. Flow is from left to right.

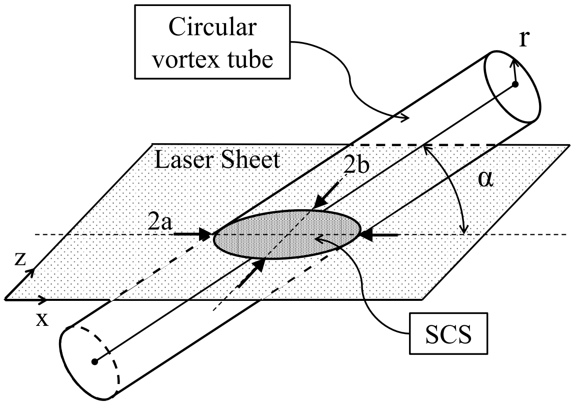

Figure 37: The SCS, a signature of a circular vortex tube cutting the wall-parallel plane of view, is shown with the major, a, and minor, b, axes of the elliptical SCS labeled along with the vortex tube inclination angle, α, and radius, r.

the latter case, the SCS would be expected to consist of elliptical, not circular, signatures in wall-parallel planes as discussed by Tomkins and Adrian [2003] and illustrated in Fig. 37. Under this interpretation, SCS are considered to be the signature of structures which are coherent in space, time and the wall-normal direction, and hence travel at a y-independent convection velocity.

5.4.2 SCS identification results

From each extracted SCS, the area, A, eccentricity (of the ellipse), ϵ, swirling strength weighted centroid, and average core velocity, U_{core}, in the streamwise direction were determined (note that a convection velocity in the wall-normal direction cannot be determined from these wall-parallel measurements). From these measurements the equivalent radius of the SCS, r_{eq}, and the inclination angle with respect to the streamwise direction, α, were calculated. Note that a distinction cannot be made between upstream and downstream inclination from our data since the elliptic footprint sketched in figure 37 would appear identical in the wall-parallel plane. For each plane, a compilation of SCS properties in 500 statistically independent snapshots were compared to the literature to verify the identification method.

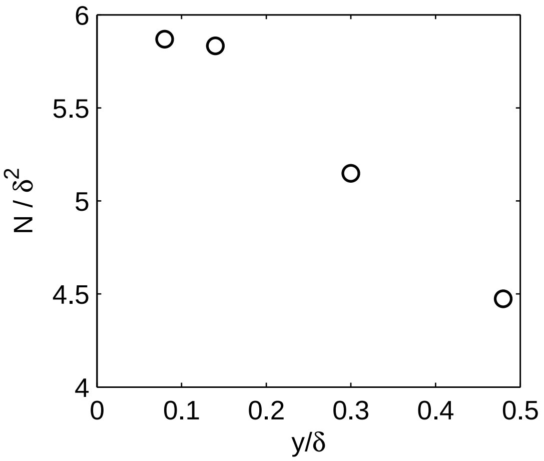

Figure 38: The number of SCS found per $\delta \times \delta$ area for each wall-normal location

The average number of SCS identified in a given $\delta \times \delta$ region of the flow is shown in Fig. 38 for each wall-normal location. As with the measurement of spanwise vortex heads by Wu and Christensen [2006], the current data also shows a decrease in the number of SCS with wall-normal distance, particularly beyond the log layer, consistent with the attached eddy hypothesis.

The eccentricity of SCS, $\epsilon = \sqrt{1-(b/a)^2}$, where a and b are the major and minor axes of an ellipse, respectively, was calculated by constructing an ellipse with the same second moments of area as the identified swirling region and measuring the ratio of the major and minor axes of this construction. From the eccentricity, the inclination angle, α, of a circular vortex tube cutting a wall-parallel plane (see Fig. 38) was inferred using Eqn. 30. α is defined as the angle the vortex core makes with respect to the wall and ranges from 0 to 90°. 0° indicates a vortex core locally parallel to the wall (not observable in the present experiments) and $90^c irc$ indicates a vortex core locally perpendicular to the wall.

$$\alpha = \sin^{-1}\left(\sqrt{1-\epsilon^2}\right) \tag{30}$$

The distribution of α binned to the nearest 5° is shown in Fig. 39a. Note that the pdf presented in Fig. 39a, as well as all subsequent pdfs (unless noted otherwise), was normalized such that the area under the pdf was equal to 1. The peak near 40° convincingly demonstrates that the extracted SCS are elliptical in shape on average. In addition, the α distribution does not vary significantly with wall-normal distance. Comparison is made with the data of Ganapathisubramani et al. [2006], which resolved inclination angles ranging from 0 to 180°, by summing the portion of their pdf from 0 to 90° with that from 180 to 90° to produce a pdf of α as defined in the present work. Further investigation by Gao et al. [2011], however, found a variation of inclination angle (what they call θ_{xz}) with height changing from 25° at a distance of $y^+ = 47$, to 45° at $y^+ = 110$, to 50° at $y^+ = 198$ for a similar Reynolds number. Note that while the error in the inferred inclination angle, which arises from uncertainties in determining the length and width of the SCS, changes with the ratio b/a as shown in Fig. 39b, it changes little when $b/a < 0.5$, decreases with increasing a, and is usually below about 20° over a wide range of a and b. For $a > 3\Delta x$, the error falls to about 8°. The differences between our data and those reported by Gao et al. [2011] close to the wall may be partially explained by the differing structure detection criteria, and perhaps the resolution of swirl and the difficulty identifying strongly inclined (low α) structures.

Differences between the present data and the data of Ganapathisubramani et al. [2006] in Fig. 39a can be explained as follows. First, an inclination angle of 0° (indicating swirling motion parallel to the wall) cannot be inferred from the present 2D2C PIV measurements. Also, for all core sizes considered, there were generally 2 or fewer inclination angles that could be inferred between $\alpha = 50°$ and $\alpha = 90°$ on account of the the discrete pixel locations, with the number of angles decreasing with decreasing SCS size, as indicated by the black dots in Fig. 39b. Thus the inferred α has a tendency to be binned to 50° or 90° degrees, but not in

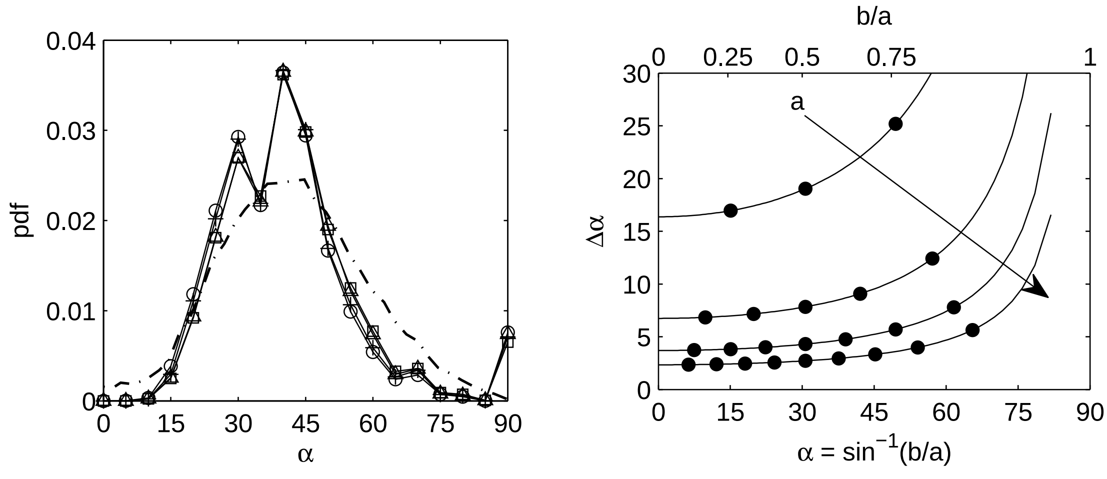

(a) Inclination angle histogram

(b) Error in angle with aspect ratio

Figure 39: (a): Distribution of the SCS inclination angle, α, for plane 1: ○, 2: +, 3: △, and 4: □. Dashed black line: elevation angle distribution from Ganapathisubramani et al. [2006] (modified as described in the text) at $y/\delta = 0.09$. (b): Error in the inferred inclination angle, $\Delta\alpha$, with varying aspect ratio for an elliptical SCS with a major axis, a. The length, a, changes from 3 to 6 vector spacings, increasing in the direction of the arrow.

between, particularly for small SCS. The deficit of counts at angles beyond 50° as well as the spike at 90°, compared to the pdf from Ganapathisubramani et al. [2006], likely arose from this poor resolution in α.

Since the SCS were shown to be elliptical in wall-parallel planes, the equivalent radius, $r_{eq} = \sqrt{A/\pi}$, was used as a measure of the SCS radius to validate the identification method. The PIV spatial resolution was $15\delta_\nu$, hence the equivalent diameter would only be measurable to this value, and half this value for the equivalent radius. For this reason, the distribution of the equivalent radii of SCS was binned to the nearest $7.2\delta_\nu$ as shown in Fig. 40a. As noted previously, though, filtering the velocity field before calculating the swirl field decreased the accuracy with which the vortex radius could be measured, with the smallest measurable radius $15\delta_\nu$, potentially smeared out to $60\delta_\nu$. The change in the mean radius with wall-normal location is recorded in Fig. 40b. While the two planes near the wall share an almost identical radius distribution, as the free stream is approached, the distribution begins to skew towards larger core radii consistent with the wall-normal growth in eddy dimension associated with Townsend's attached eddy hypothesis. The lack or the variation of the core radii for planes nearer the wall may be at least partially explained as an artifact of the smoothing of the swirl field already discussed.

Comparing to the literature, Carlier and Stanislas [2005] measured a mean radius of 20–30δ_ν, increasing with wall-normal distance. Differences between the current measurements and Carlier and Stanislas [2005] can be rectified by calculating the radius of the vortex tube cutting the wall-parallel plane, inferred from the inclination angle and the aspect ratio of the SCS measured in plane. Making reference to Fig. 37 and using the relationship $r_{eq} = \sqrt{A/\pi}$, the area of an ellipse $A = \pi ab$, assuming a tilted circular vortex tube $a = b/sin(\alpha)$, and the core radius, $r = b$, then:

$$r = r_{eq}\sqrt{sin(\alpha)} \tag{31}$$

By applying this correction, the corrected radii fall within the expected range of sizes as shown by the triangle symbols in Fig. 40b. Thus our identification method gave results consistent with the existing literature based on ensemble averages of spatial fields and an analysis of the temporal behavior of the SCS was performed.

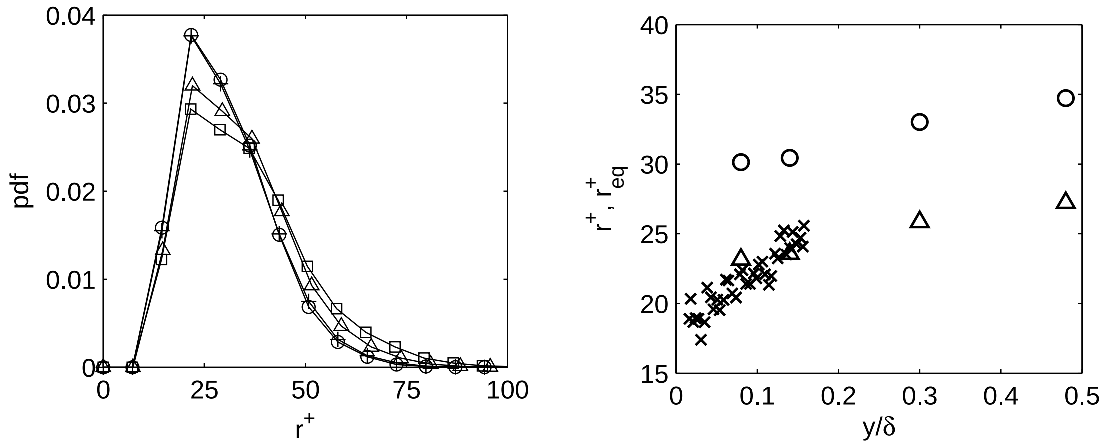

(a) Core radius distribution

(b) Mean core radius

Figure 40: (a): Distribution of the SCS equivalent radii, r_{eq}, for plane 1: ○, 2: +, 3: △, 4: □. (b): Wall-normal variation of the mean value of ○: r_{eq}, △: r (calculated from r_{eq} using Eqn. 31), and x: the vortex radius from the wall-normal measurements of Carlier and Stanislas [2005] at $Re_\theta = 7500$.

5.5 Swirling coherent structure tracking

5.5.1 SCS tracking technique

The swirl-weighted centroids of SCS were tracked in time using the time-resolved data to analyze SCS trajectories in the wall-parallel plane as well as to investigate their average lifetime and properties. Tracking was performed on Eulerian structures; that is structures were identified in each frame independent of one another as opposed to tracking the evolution of Lagrangian tracers in time, e.g. Yang and Pullin [2011]. The velocity fields were subsampled in time so that, on average, a SCS would travel forward at least one vector spacing between frames; $\Delta t_{new} = \Delta x / \overline{U}(y)$.

The SCS centroids in consecutive frames were compared to determine the SCS (centroid) trajectories. For each SCS in the first frame, a nearest neighbor with the same swirling direction was identified in the second frame. If the nearest neighbor was within a "reasonable" distance of the original SCS, then the two were identified as being the same structure. The criteria for a valid nearest neighbor required that the SCS either not move in the streamwise direction (for any convection slower than the local mean, the SCS will not move a whole vector spacing) or that it did not move faster than the free-stream velocity. This range, defined as $0 \le (x_1 - x_0) \le U_\infty / \overline{U}(y) \Delta x$, was widened to account for inaccuracies in determining the SCS centroid by Δx on both ends. In addition, spanwise motion was restricted such that $|z_2 - z_1| \le 2\Delta z$ per time step. This constraint was applied to assure that neighboring SCS were not mistakenly picked up in the tracking method and was deemed a reasonable limit given that the main direction of flow was in the streamwise direction and the spanwise motion was observed to be only a small fraction of this.

Regardless of the restrictions placed, there were still issues with tracking SCS in time; one example is shown in Fig. 41. In the first frame, two nearby SCS of the same sign are illustrated by blue circles with the x marking their centroids. In the second frame, the SCS are wrongly marked as a single core due to poor spatial resolution of the nearby structures, and thus only one centroid is found. The circled SCS in the first frame has now lost its trace as only one of the two SCS can be linked with this new structure. In the final frame, the SCS are again correctly identified, but the circled SCS is incorrectly marked as a new SCS as there was no distinct nearest neighbor in the previous frame. To help alleviate this issue, after identifying all SCS trajectories, the SCS position at the end of a trajectory was projected forward at the local mean velocity for the next two frames. Following Fig. 41, the position of the circled SCS in frame 1 would be projected forward in frames 2 and 3. Then, if the start of a new SCS trajectory was found to be a nearest neighbor of that projected SCS, the two trajectories would be merged together. Referring to Fig. 41, the

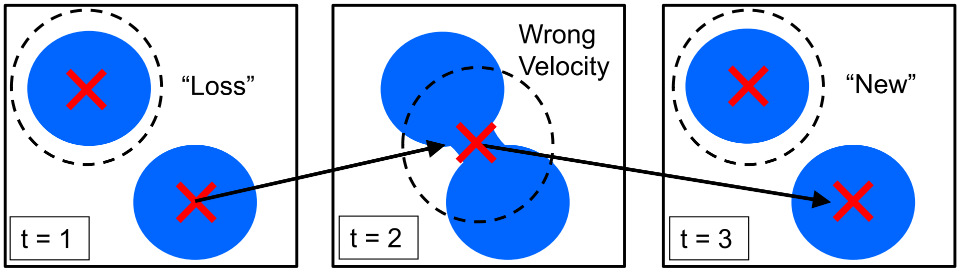

Figure 41: Cartoon showing how a SCS trace can be lost due to poor resolution. SCS are represented by blue regions and the SCS centroids are marked with red x's. The dashed circles indicate where tracking of a particular SCS has failed.

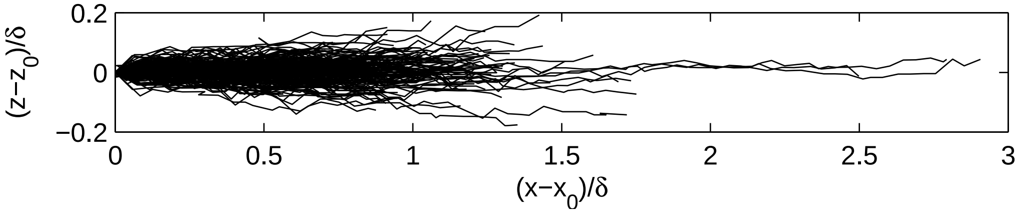

Figure 42: SCS trajectories at $y/\delta = 0.3$ that persist for more than one eddy turnover time (δ/U_∞)

SCS trajectory ending with the circled SCS in frame 1 would be merged with the trajectory staring with the circled SCS in frame 3.

5.5.2 SCS tracking results

The SCS were found to move predominantly in the streamwise direction, as expected, with limited motion in the spanwise direction, as shown in the trajectories of Fig. 42. Note that no additional smoothing has been applied to these trajectories in order to maintain a faithful representation of the spanwise resolution. The average trajectory angle, θ_t, was calculated by fitting a straight line to each trajectory. A histogram of the trajectory angles is shown in Fig. 43a. The width of these histograms, and thus any spanwise motion, is small, and decreases with wall-normal distance. At all wall-normal locations, one would expect a trajectory angle of 0° on average due to the symmetry of the pdf about 0°.

The dominant peak in the θ_t histograms at 0°, along with observations from the time-resolved velocity fields, suggests that vortex packets on average travel on nearly straight trajectories, deviating very little in their spanwise location over the entire field of view, but likely growing in the vertical direction. It seems unlikely that the well-known spanwise growth with distance from the wall occurs by continuous expansion of individual SCS in the spanwise direction, in time, as they convect downstream, but rather through a discrete mechanism such as the packet merging mechanism of individual component vortices discussed by Tomkins and Adrian [2003]. Note, however, that the combination of our tracking algorithm and spatial resolution is not sufficiently sophisticated to distinguish convincingly between such mechanisms.

Using the time-resolved data, the distribution of the SCS lifespans was determined, where T_L denotes the lifespan of a SCS. The lifespan is defined as the amount of time that a SCS in one of the wall-parallel planes can be tracked in time. The lifespan is skewed toward lower values due to SCS which leave the field of view in x or z. Also, it is possible for a SCS to travel up or down in the wall-normal direction (y) as time progresses or to grow away from the wall with the boundary layer, which grows by about 10% over the field of view, and thus leave the field of view and further decrease the measured lifespan. With these constraints in mind, a pdf of the SCS lifespan for each plane is shown in Fig. 43b. A majority of the SCS persist for less than 1 eddy turnover time, T_E, with an initial decay rate of 1.6 decades per T_E for all wall-normal locations. In all cases, the pdf has dropped to 0.01–0.02 by $T_L = T_E$. It must be noted that most of these counts at small

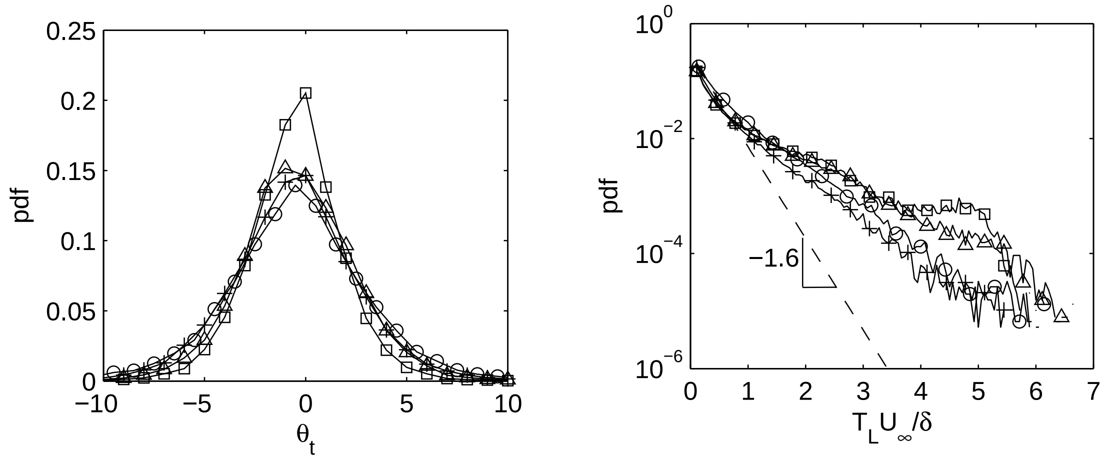

(a) Trajectory angle

(b) Vortex lifespan

Figure 43: (a): Histogram of the SCS trajectory angles for planes 1: ○, 2: +, 3: △ and 4: □. Data is compiled from both CW and CCW swirling motions and for all runs recorded. (b): Pdf of SCS lifespan for planes 1: ○, 2: +, 3: △, and 4: □. Dashed line: the slope of all pdfs before $0.5\delta/U_\infty$

T_L are likely due to issues with tracking a particular SCS in time, such as the issue illustrated in in Fig. 41. As the free stream is approached, SCS tend to live for longer periods of time, as noted by the larger values of the pdf at long times for planes 3 and 4 in Fig. 43b, which is postulated to be an effect of the reduction of turbulent stresses deforming and possibly destroying these structures further from the wall. The plateau in the pdf at long times (between 3.5 and 5 $T_L U_\infty/\delta$) in plane 4 is an effect of the limited observation time (limited by the size of the domain) as will be discussed later in this subsection in conjunction with Fig. 46.

A simple estimate of the SCS convection velocity was extracted from the SCS trajectories by dividing the change in streamwise position of the SCS centroid by the time between the two frames investigated. Note that this linear scheme cannot identify changes in streamwise convection velocity, which have been observed to occur over timescales larger than the Lagrangian timescale by Elsinga et al. [2012], spanwise convection velocity, or a non-zero wall-normal convection velocity, but does provide a robust characterization of convection velocities over our large wall-parallel domain. Of course more sophisticated schemes could be applied. Between individual time steps, the measured convection velocity, U_{traj} fluctuated due to issues in finding the SCS centroid. In particular, expecting a positioning error of half the window length, $7.5\delta_\nu$, would result in an error in the measured velocity of $u^+_{error} = 7.1$–9.6. Over a number of time steps the average convection velocity quickly converged to a mean value and this error shrinks. For this reason, the average convection velocities over a trajectory, $< U_{traj} >$ and $< u_{traj} > = < U_{traj} > - \overline{U}$ are reported, where the triangle brackets indicate an average over the entire vortex trajectory.

The pdf of $< u_{traj} >$ for SCS whose lifespan exceeded one eddy turnover time, i.e., $T_L > T_E$, is shown in Fig. 44a for each wall-normal location. For these cases, the convection velocity has been calculated and averaged over at least 16 time steps ($t^+ \geq 5.44$). The peaks of all the pdfs are close to the local mean, $\overline{U}(y)$, with the peak shifting toward slightly slower values as y increases. All pdfs also have a similar low-speed tail which is longer than the high-speed tail. The major differences between different wall-normal locations is a thinning of the high-velocity end of the pdf, and hence an increase in the peak amplitude of the pdf, most notable at $y/\delta = 0.48$, an effect of the upper limit on the convection velocity set by the free-stream velocity. This is readily observable in the pdf of $< U_{traj} >$ in Fig. 44b and is also evident in the estimates of the convection velocity of spanwise vortex cores obtained by integration of the spatial velocity field by Wu and Christensen [2006]. It is apparent that no SCS traveled at speeds above the free-stream velocity ($U^+_\infty = 22.5$) and none were observed below $U^+ = 8$, the estimate of the lower bound on the convection velocity of energetic disturbances in the boundary layer identified by Morrison et al. [1971].

The average of all velocity vectors within each SCS, U_{core} (a commonly-used approximation to the convection

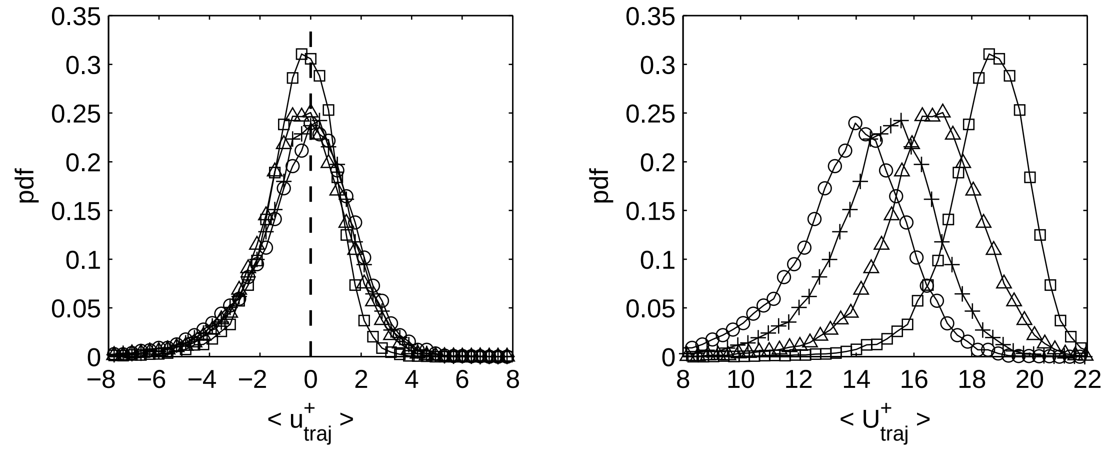

(a) SCS convection velocity pdf

(b) Absolute convection velocity pdf

Figure 44: (a): Pdf of $< u_{traj} >$ for planes 1: ○, 2: +, 3: △, and 4: □. (b): Distribution of SCS trajectory velocity, $< U_{traj} >$ for plane 1: ○, 2: +, 3: △, and 4: □.

velocity for non-time-resolved PIV studies - note that U_{traj} cannot be calculated from an ensemble of instantaneous fields), was also calculated as a measure of the SCS convection velocity. It is equivalent to the convection velocity that, when subtracted from the instantaneous velocity, would produce a set of closed streamlines at the location of the SCS. For comparison, the calculated values are averaged over the vortex trajectory to obtain $< U_{core} > = < u_{core} > + \overline{U}$. The mean value of $< u_{core} >$ over all trajectories, $< u_{core} >_m$, is compared to $< u_{traj} >_m$ at each wall-normal location in Fig. 45a, showing values of $< u_{core} >_m$ closer to the local mean velocity than $< u_{traj} >_m$, with a value slightly higher than the local mean near the wall and slower than the mean far from the wall. The finding that $< u_{traj} >_m$ is lower than the local mean at all wall-normal distances is similar to the findings of Gao et al. [2011] that vortices propagate at 96-98% of the local mean with stronger vortices convecting slower than weaker ones.

To explain the difference between $< u_{core} >_m$ and $< u_{traj} >_m$, the convection velocity pdfs of each at plane 3 are compared in Fig. 45b. This figure shows a similar distribution of velocities above the local mean, but the $< u_{traj} >$ pdf has a longer low speed tail and lower central peak than the $< u_{core} >$ pdf, and hence a lower mean value. While the distribution of convection velocities is similar for $< u_{core} >$ and $< u_{traj} >$ at all wall-normal locations, the u_{traj} measure identifies more slow-moving SCS. This effect could be at least in part attributable to the importance of the (unquantified) wall-normal convection velocity, v_{traj}, of the SCS. Under the assumption of a $< v_{traj} >$ pdf with a width of the same order as for the streamwise convection velocity, the error associated with the neglected wall-normal motion can be determined to lead to a broadening of the $< u_{traj} >$ pdf that is not negligible with respect to the differences identified in Fig. 11b. Positive $< v_{traj} >$ could give rise to longer apparent tails of the $< u_{traj} >$ pdf. The temporal evolution and growth of SCS-like structures is well-known. However, in the absence of synchronous measurements of the PIV measurements in the wall-normal direction, no conclusive statement can be made about the magnitude and importance of any wall-normal convection velocity. It is believed that the trends discussed below are robust to this potential source of error.

Finally, to complete the picture, the lifespan and convection velocity of SCS are considered simultaneously using joint pdfs as presented in Fig. 46 for each wall-parallel plane. The red line indicates the edge of the domain determined by dividing the size of the streamwise field of view by the convection velocity, $< U_{traj} >$. This edge is the time at which a SCS would leave the field of view if the SCS started at the most upstream end of the field of view and was traveling at a fixed velocity, $< U^+_{traj} >$. A large buildup of counts at this limit is found at $y/\delta = 0.48$ as shown in Fig. 46d. Thus, in this plane, the lifespan of a reasonable portion of the SCS persist for longer than 5 eddy turnover times. This buildup of counts was previously identified as a plateau in the SCS lifespan histograms shown in Fig. 43b (i.e., the integral of the jpdf over $< U^+_{traj} >$) and

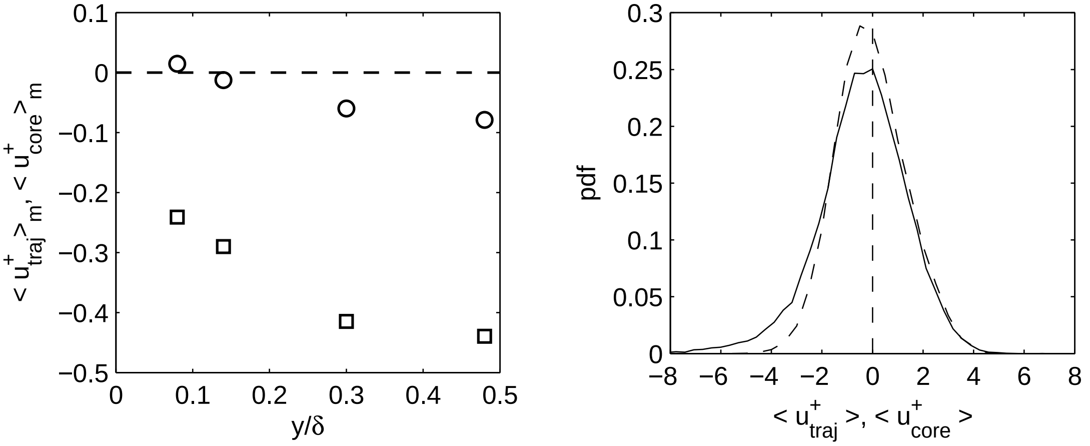

(a) Mean convection velocity **(b)** Pdf comparison

Figure 45: (a): Mean convection velocity for each plane where □: $< u_{traj} >_m$ and ○: $< u_{core} >_m$. (b): Comparison of convection velocity pdfs for plane 3. Dashed line: $< u_{core} >$, solid line: $< u_{traj} >$

confirms the trend of increasing lifespan with wall-normal distance. Despite the relatively large field of view in this study, it still places a constraint on the statistics associated with long life-time SCS.

5.6 Implications for models of swirling coherent structure

The subsections above present the statistical features associated with swirling coherent structures identified non-synchronously in four wall-parallel planes. In what follows, we exploit converged statistics over many realizations of SCS, rather than a rigorous connection of instantaneous structures, to investigate how well the data agree with a model of SCS behavior that constrains the structures to travel at or close to an identical convection velocity at all wall-normal planes in order to remain coherent for a significant time. We then ascribe observations in different planes to distinct "model structure types" with similar convection velocities. Of course the decorrelation effect associated with the full turbulent velocity field may prevent a single structure from being observed to span multiple planes, however structures traveling with the same convection velocity will be understood to have a similar origin.

Such a model is entirely consistent with the attached eddy ideas proposed by Townsend [1976] and developed further by Perry and co-workers, e.g. Perry and Chong [1982], Perry et al. [1986], Perry and Marusic [1995]. These authors developed a model for the underlying mechanics of wall turbulence based on the action of self-similar hierarchies of hairpin-like vortices that scale on distance from the wall. The wall-normal extent of each such vortex would be understood to be associated with a single structure convection velocity. The subsequent conceptual model of vortical structure developed by Adrian et al. [2000], illustrated in their Fig. 25, outlines packets of hairpin vortices that travel with similar convection velocities. By extension, for such packets to have temporal coherence, individual structural components must be assumed to convect at similar speeds across their full wall-normal extents. This assumption is supported by the film of Bandyopadhyay and Head [1979], which shows that all points on a given vortex, identified using smoke visualization, appear to convect at a uniform streamwise velocity. However, indications from DNS [Lozano-Duran et al., 2012] suggest that wall-normal variation of the convection velocity for a range of structures is likely, leading necessarily to reduced temporal coherence as structures are stretched and eventually torn apart.

In what follows, we investigate model structures whose signature in different planes is constrained to travel at the same convection velocity. While multi-plane, synchronous PIV measurements would be required to prove the hypothesized relationships, we believe that our approach suggests a useful and statistically-sound means of classifying possible SCS connectivity for the cases where individual, constant structure convection velocities are appropriate. We note that the discussion that follows is limited to these cases only.

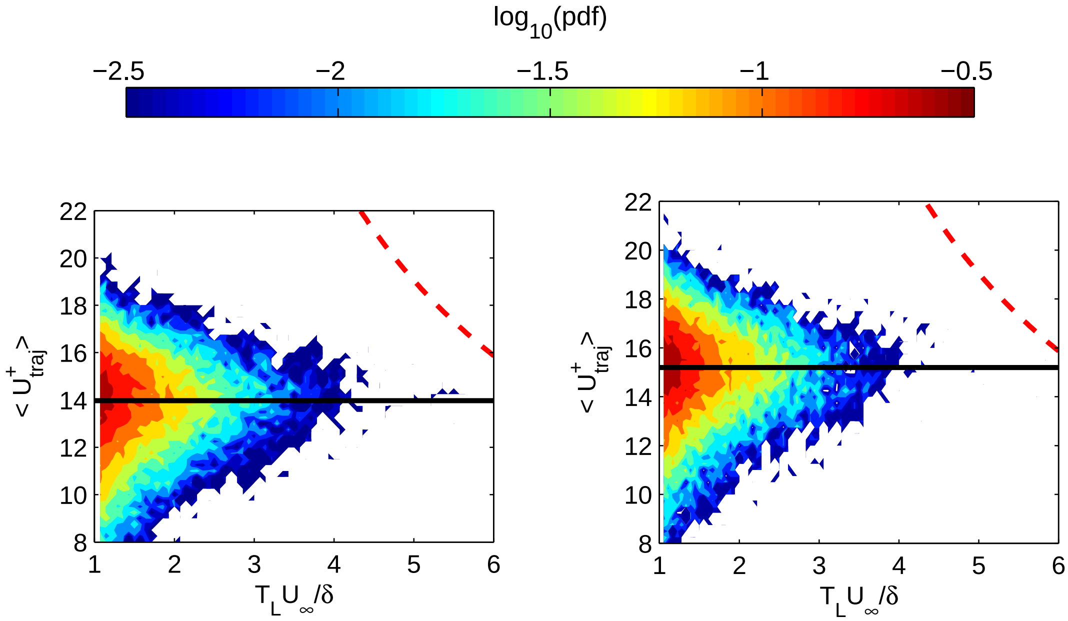

(a) Plane 1, $y^+ = 33$ **(b)** Plane 1, $y^+ = 58$

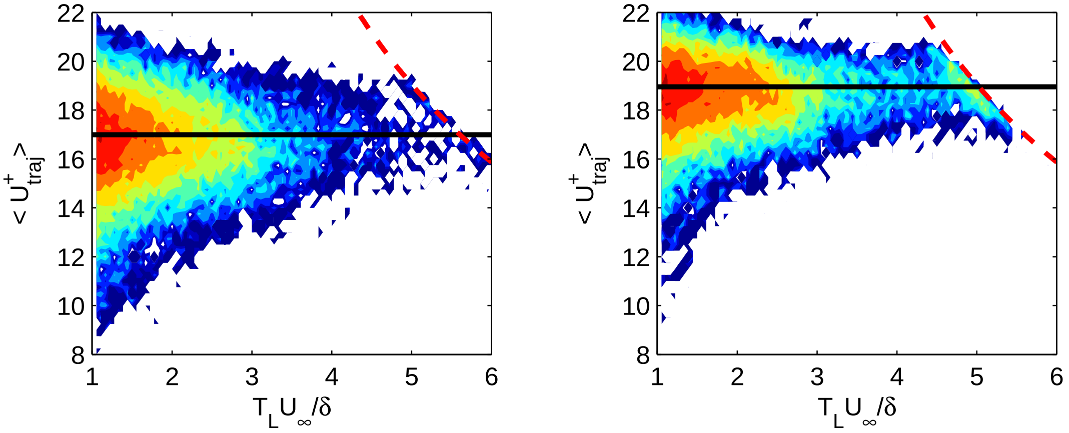

(c) Plane 1, $y^+ = 122$ **(d)** Plane 1, $y^+ = 198$

Figure 46: The joint pdfs of SCS convection velocity and SCS lifespan for plane (a): 1, (b): 2, (c): 3, and (d): 4. The color indicates the probability of having a vortex with a given lifespan and trajectory velocity, where the double integral over $< U^+_{traj} >$ and $T_L U_\infty/\delta$ is equal to 1. Black line: local mean velocity, dashed red line: edge of the domain

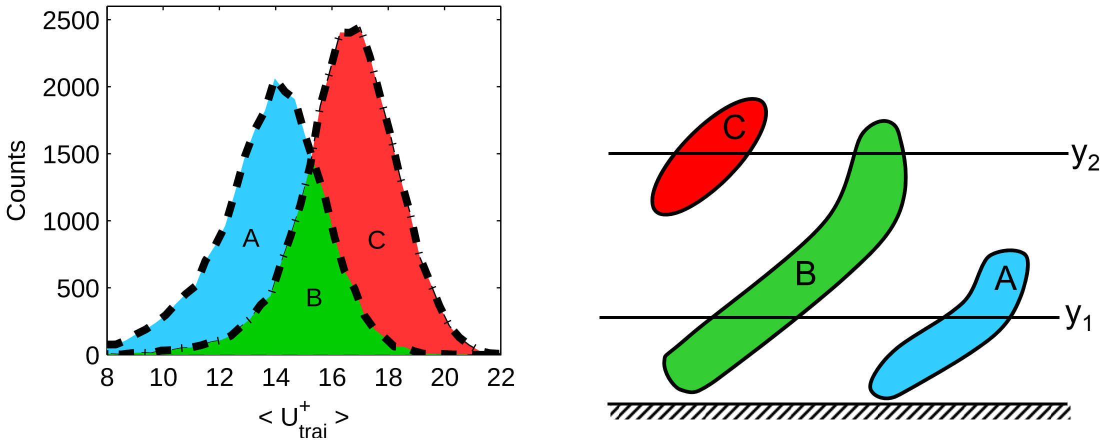

(a) Histogram comparison

(b) Cartoon of inferred structures

Figure 47: (a) Comparison of convection velocity histograms at $y/\delta = 0.08$ and $y/\delta = 0.30$ leading to the identification of 3 distinct regions. The labeled regions are referenced in (b) showing the structure shapes inferred from the histograms in (a).

Fig. 47 shows an overlay of convection velocity histograms for two different planes. Region B, where the histograms overlap, represents structures that convect at the same velocity and could be interpreted to be connected between the two planes. Regions A and C represent structures that exist in only one of the two planes. By analyzing these comparisons for all combinations of the four measured planes, ten different model structures types can be inferred as shown in Fig. 48, organized by likelihood of observation. The percentage of each type of structure in the flow is also recorded in this figure (identified from the four curves in Fig. 44b). To label the structures, we introduce the terminology $\Psi(i,j)$, where i and j are the numbers of the plane nearest the wall and furthest from the wall through which the structure passes, respectively. The method for counting and calculating the convection velocity histograms for these structures is described in Appendix **??**.

Results from this analysis are described in the remainder of this subsection, but first, some limitations of this method are outlined or reiterated. The first issue to note is that the connectivity between wall-parallel planes depends on the threshold chosen to identify SCS. For example, with a lower threshold, more SCS would be identified in all planes, and this could lead to an increase in the connectivity between different planes, possibly increasing the number of SCS that extend to planes 1 and 4. It has also been assumed that the convection velocity is y-independent and constant in time, which does not allow for the growth of SCS, that is they cannot stretch in the streamwise direction as they travel downstream. Similarly, this framework does not have a way to count vortices which grow in wall-normal extent and reach a plane further from the wall at some later point in time.

With these constraints in mind, some statements can be made about the likely distributions of model structure type. From Fig. 48 it is apparent that the most prevalent SCS is $\Psi(1,2)$, a structure that reaches down to plane 1 ($y^+ = 38$) and does not reach beyond the log layer (plane 2). We term this an attached structure, implying only that the footprint of the structure reaches down to the wall. The taller attached structures, $\Psi(1,3)$ and $\Psi(1,4)$, are less common than $\Psi(1,2)$ (which occurs in 22% of all observations), in agreement with the observation that the majority of hairpin heads are found in the log layer [Wu and Christensen, 2006]. Fig. 49a shows the variation of the number of attached structures with wall-normal distance, an approximately logarithmic decay. This decrease in attached structures with wall-normal extent is supported by the measurements Hutchins et al. [2005], where streamwise velocity correlations were used to infer that a majority of structures should be detached by $y/\delta = 0.4$ and at least some should be detached as close as $y/\delta = 0.05$.

Jpdfs, as shown in Fig. 46, can also be constructed for each model structure type. Similar to the process described in Fig. 47, joint lifespan, convection velocity histogram surfaces are constructed for two different planes and overlaid. Regions enclosed by both histogram surfaces can be interpreted as model structures

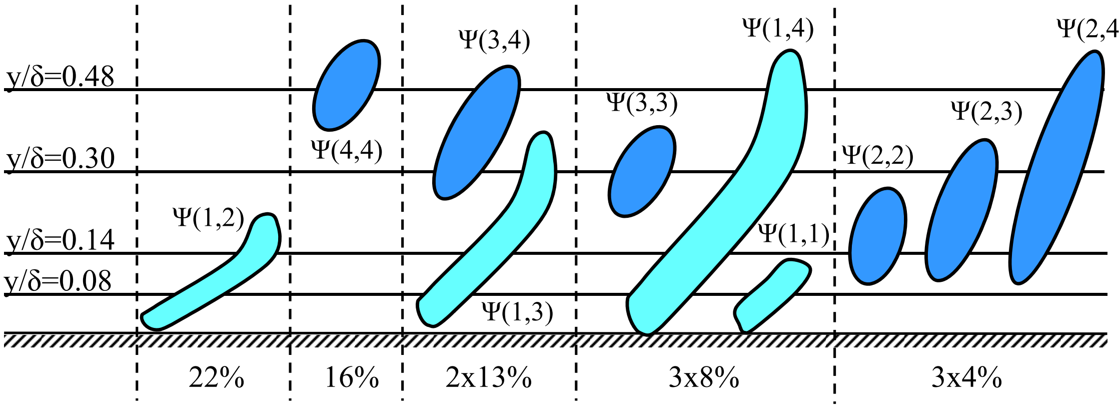
y/δ=0.48
y/δ=0.30
y/δ=0.14
y/δ=0.08
Ψ(1,2)
Ψ(4,4)
Ψ(3,4)
Ψ(1,3)
Ψ(3,3)
Ψ(1,4)
Ψ(1,1)
Ψ(2,2)
Ψ(2,3)
Ψ(2,4)
22%
16%
2x13%
3x8%
3x4%

Figure 48: The model structures are shown in order of their prevalence in the boundary layer. The percentage given is rounded to the nearest percent and SCS with similar percentages are grouped together. Lighter colored SCS are attached and darker colored SCS are detached from the wall.

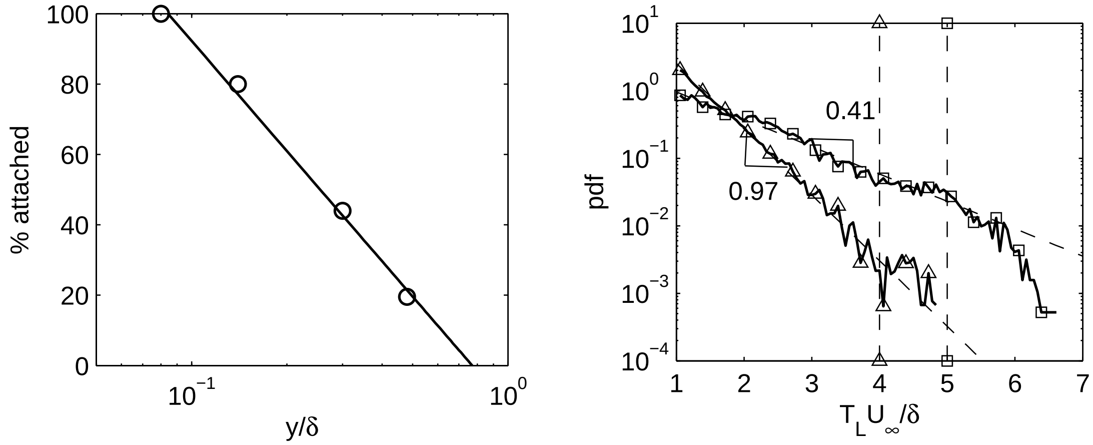

(a) Percentage of attached SCS

(b) Attached/detached lifespan

Figure 49: (a): The percentage of SCS at a given wall-normal distance that are "attached" to the plane nearest the wall. (b): Lifespan pdfs for all attached structures (△) and all detached structures (□). Dashed black lines (no symbols): log fit to the lifespan decay for attached or detached structures up to the vertical dashed line with the corresponding symbols

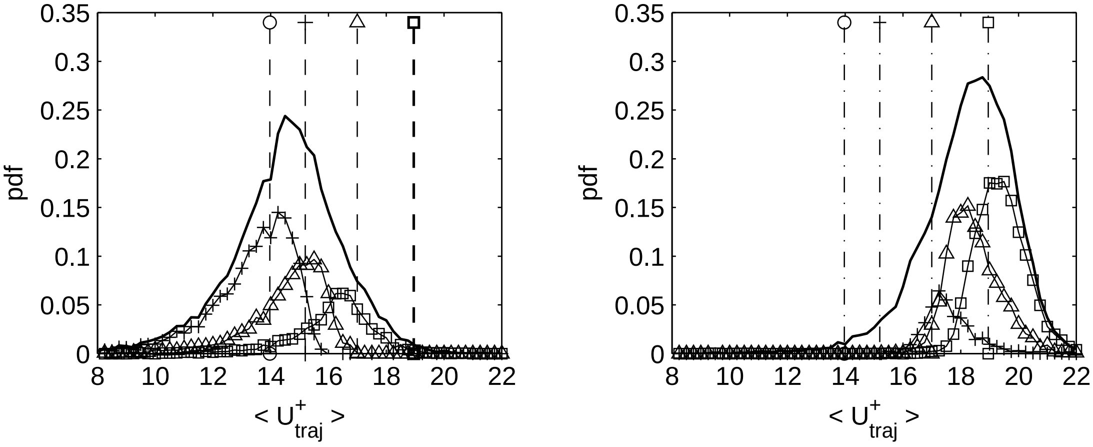

(a) Plane 2 **(b)** Plane 4

Figure 50: The trajectory velocity pdf for planes 2 and 4 are shown by a solid line in (a) and (b), respectively and the vertical dashed lines indicate the local mean velocity in plane 1: ○, 2: +, 3: △, and 4: □. The other lines are the convection velocity pdfs for (a): attached structures passing through plane 2; $\Psi(1,2)$: +, $\Psi(1,3)$: △ and $\Psi(1,4)$: □, (b): detached structures passing through plane 4; $\Psi(2,4)$: +, $\Psi(3,4)$: △, and $\Psi(4,4)$: □.

connected between the two planes, and regions enclosed by only one of the two histograms as structures that exist in only one of the two planes. The process described in Appendix **??** can also be applied to these joint-histograms to determine the distribution $\Psi(i,j)$ for each structure type.

By integrating the jpdf for a particular model structure type over the trajectory velocity, the lifespan of that structure type can be found. The lifespan pdfs for all attached structures were similar as well as all detached structures, so an average lifespan pdf is presented for attached and detached structures in Fig. 49b. The faster decay rate of the attached structures compared to the detached structures is notable, with the probability of having a SCS exist for an additional eddy turnover time dropping by less than half a decade (0.4) for detached structures, but dropping by nearly a full decade for attached structures. The pdf at large T_L is less converged for attached SCS due to the small number of counts at lifespans beyond $4T_E$ and the decay at large times for the detached structures is due to the limited field of view beyond about $5T_E$ as noted earlier.

The convection velocity pdfs associated with each type of model structure can be calculated by integrating the jpdfs over the lifespan. The velocity pdfs of different structure types can be used to elucidate the makeup of the convection velocity pdfs presented in Fig. 44. Two examples are examined in Fig. 50. The convection velocity pdfs of all attached and all detached structure types are shown in Figs. 50a and 50b, respectively. These structure pdfs have been normalized considering the percentage of all structure types which pass through a given plane, such that the sum of all of the structure pdfs produces the trajectory velocity pdf for that plane.

In Fig. 50a, a majority of the model structure detected are attached. Shorter SCS (i.e., $\Psi(1,2)$) convect slower than the local mean (dashed line with + symbol) on average, while taller SCS (i.e. $\Psi(1,4)$) constitute the part of the pdf traveling faster than the local mean, on average. For each attached structure type, the ratio of the mean trajectory velocity to the local mean velocity in the uppermost plane through which the structure passes, j, ranges from 0.85–0.88. This suggests that attached hairpin vortex structures identified by SCS do not convect at the speed of their heads, on average, but at the local mean somewhere between their head and the wall.

Further from the wall, as in Fig. 50b, even the tallest attached structures travel at a speed around 85% of the free-stream velocity ($u^+ = 18.7$) on average, and thus the high speed end of the pdf is representative of detached structures. Detached structures which reach down closer to the wall, $\Psi(2,4)$ and $\Psi(3,4)$, primarily contribute to the low-speed end of the pdf while structures reaching further from the wall, $\Psi(4,4)$ primarily contribute to the high-speed end.

5.7 Summary of TRPIV results

We presented for the first time 3D streamwise velocity power spectra (2D in space and 1D in time) in all regions of the turbulent boundary layer and outlined the method for calculating and normalizing these from PIV measurements. The effect of the PIV interrogation window on the resolution and attenuation of both the spectrum and the measured velocity fluctuations was discussed. In addition, the methods used for reducing aliasing and spectral leakage were outlined. From the 3D spectra presented, the more usual 1D and 2D spectra were also calculated and compared to previous findings. The 3D spectra present input conditions for the resolvent analysis to be presented subsequently.

With the current data set, it was found that the spanwise resolution of the streamwise velocity fluctuations was lacking, while the streamwise and temporal resolution were reasonable. Current experiments are underway to improve the spanwise resolution and also to increase the dynamic range to improve the resolution of spanwise fluctuations so that the spanwise and streamwise-spanwise cross spectrum can be analyzed. Regardless of these issues, it was still possible to consider the convection velocity of streamwise scales over both streamwise and spanwise wavenumbers using the calculated 3D spectrum. The investigation and interpretation of these is an area of current interest.

Swirling coherent structures (SCS) were reliably extracted from two-dimensional information in wall parallel planes and tracked in time with geometric properties matching other data reported in the literature. Using time-resolved measurements, several important conclusions were drawn. First, differences were found in the distribution of trajectory velocities, $< U_{traj} >$, compared to the average core velocity calculated from instantaneous snapshots, $< U_{core} >$, a measure often reported in the literature. The major difference was a longer low-speed tail using the trajectory velocity, indicating that the time-resolved data and the centroid-tracking algorithm allowed the detection of slow traveling vortices (although the error in $< U_{traj} >$ associated with an unquantified potential distribution of wall-normal convection velocities is noted). Besides the low speed tail, the distributions from both calculations were nearly identical.

Time-resolved measurements also allowed the measurement of the lifespan of vortices, which increased with increasing wall-normal distance, and a small percentage of vortices persisted for more than 5 T_E at $y/\delta = 0.48$. This is the first time such a long tracking history has been presented in a wall-bounded shear flow. This is not as long as the structure lifetime predicted by Elsinga and Marusic [2010], but it should be noted that this measure was inferred from a study of the rate of change of the velocity gradient invariants, Q and R, which were integrated to recover trajectories in the (Q, R) plane. These trajectories were found to form an orbit around the origin, oscillating between the 4 basic structure types (stable and unstable nodes and vortices), where the time to complete a full orbit was taken as a measure of the average lifetime of coherent structures. Considering only the time where the flow topology around a fluid particle would be a stable focus, reported to be 39% of the orbit time in a turbulent boundary layer by Elsinga and Marusic [2010], the estimated lifespan, 5.58 T_E, would be closer to the present measurements. It should also be reiterated that since the current measurements were taken in a 2D plane, it is possible for vortex structures to have wall-normal convection velocities, implying that the measured SCS may move out of the plane of view and leading to lifetimes that may in some cases be shorter than that of the real vortex structures, and that the streamwise convection velocity pdfs may be erroneously broadened.

Further analyzing the time-resolved data, SCS trajectories were found to be streamwise aligned for the most part, with trajectory angles no more than ±10°, decreasing with increasing distance from the wall. This finding along with the observations of the evolution of the full time-resolved velocity fields supports the hypothesis that vortex packets do not grow continuously in the spanwise direction as they convect downstream, but must do so in some discrete manner.

Finally, using the convection velocity histograms, and under the limiting assumption that a coherent structure in the flow must travel at or near a single velocity at all distances from the wall, the distribution of "model structures" were inferred with a focus on whether or not these structures were attached, that is, have a signature in the plane nearest the wall. From joint convection velocity, lifetime pdfs, it was found that attached structures decay more than twice as fast as detached structures in time. In addition, the convection velocity pdf for each structure type was used to highlight the composition of the convection velocity pdf with SCS traveling both faster and slower than the local mean. Near the wall, most detected structures were attached to the wall and there was a large spread in convection velocity depending on the wall-normal extent of the structure in question. Further from the wall, the pdf was dominated by detached structures and the high speed tail was thinned compared to the low speed tail because structures do not appear to travel faster than the free-stream velocity. While this method provided results consistent with the attached eddy hypothesis and capable of explaining at least some of the characteristics of SCS, further examination of the three-component, three-dimensional velocity field, either from experiments or simulations, would add confidence in the importance of the findings described here; however this work underlines the importance of time-resolved measurements in determining the characteristics of coherent structure.

6 2D/3C model for the mean velocity in turbulent pipe flow

The stochastically-forced, two-dimensional, three-(velocity) component model for the mean velocity in wall turbulence was introduced by Gayme et al. [2010], who considered channel flow in earlier work. Under the PECASE award, this model was extended to pipe flow. The results revealed some important differences between pipe and channel flow, in that the present work identified the footprint of the turbulent puffs that are observed in pipe flow transition. The capture of the blunting of the laminar mean velocity towards the turbulent profile is an important first step to providing a mean profile for input to the resolvent analysis without resorting to experimental or computational results.

The work described below was published as Bourguignon and McKeon [2011] in Physics of Fluids.

6.1 Model and numerical methods

The streamwise-constant model of turbulent pipe flow is derived from the NSE written in cylindrical coordinates under the assumption of streamwise invariance, i.e., it constitutes a projection of the NSE onto the streamwise direction. We employ a nondimensionalization based on the pipe radius R and the bulk velocity $\bar{U}$, i.e., $\eta = r/R$, $\tau = \bar{U}t/R$, and $Re = 2R\bar{U}/\nu$, where ν is the kinematic viscosity, throughout this paper. Continuity is enforced via the introduction of a dimensionless streamfunction W whose evolution equation is obtained by taking the curl of the NSE projected in the axial direction. The model consists of a forced evolution equation for the streamfunction, from which the radial and azimuthal velocities can be derived, and an evolution equation for the axial velocity (in terms of the deviation from the laminar profile) corresponding to the axial momentum balance, subject to boundary conditions (BCs) of no-slip and no-penetration on the wall of the pipe. The deviation of the local axial velocity from laminar illustrates how the flow evolves away from the laminar state and is defined as

$$u_x = \tilde{u}_x(\eta) - U(\eta), \tag{32}$$

where $\tilde{u}_x$ is the instantaneous axial velocity and $U(\eta) = 1 - \eta^2$ is the laminar base flow.

The 2D/3C model was first derived by Joseph and Tao (1963)6 and is written as follows for the cylindrical coordinate system shown in Figure 1:

$$\begin{aligned}
\frac{\partial \Delta\Psi}{\partial \tau} &= \frac{2}{Re}\Delta^2\Psi + \mathcal{N}_\psi, & (33)\\
\frac{\partial u_x}{\partial \tau} &= C - \frac{1}{\eta}\frac{\partial \Psi}{\partial \phi}\frac{\partial U}{\partial \eta} - \frac{1}{\eta}\frac{\partial \Psi}{\partial \phi}\frac{\partial u_x}{\partial \eta} + \frac{1}{\eta}\frac{\partial \Psi}{\partial \eta}\frac{\partial u_x}{\partial \phi} + \frac{2}{Re}\Delta u_x, & (34)\\
\Psi|_{\eta=1} &= \frac{\partial \Psi}{\partial \eta}|_{\eta=1} = 0 & (35)
\end{aligned}$$

Only the streamfunction equation is forced, based on the results of the study by Jovanovic and Bamieh [2005] which showed that maximum amplification is obtained by forcing in the cross-sectional plane in the linearized NSE. Thus, $\mathcal{N}_w$ represents a forcing term that is required to maintain the perturbation energy in an otherwise stable system and can be considered to represent "noise that is always present in experiments, e.g., wall roughness, vibrations, non-alignment of the different sections of the pipe, thermal effects, as well as taking into account the effects not modeled by the streamwise invariance approximation. In the subsequent sections, we consider two of the simplest possible forms for $\mathcal{N}_w$ in order to investigate the origin of the blunting of the mean velocity profile. The nonlinear terms in the governing equation for the streamfunction are neglected in order to obtain the simplest model able to capture the blunting of the velocity profile and also because their effects can be incorporated into the unstructured forcing term $\mathcal{N}_w$. Moreover, the study of Gayme et al. [2010] showed that there are no significant differences in the Couette flow statistics obtained from the model based on a linearized stream- function equation compared to the fully nonlinear 2D/3C model. The bulk velocity is maintained constant by adjusting the pressure gradient C, i.e., the Reynolds

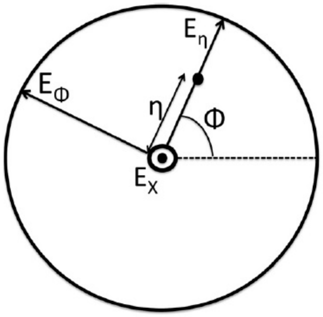

Figure 51: The coordinate system used to project the Navier-Stokes equations.

number is held constant for each study. The streamwise velocity behaves as a passive scalar convected by the in-plane velocities.

The 2D/3C model with stochastic forcing is discretized using a spectral-collocation method based on Chebyshev polynomials in the radial direction and Fourier modes in the azimuthal direction, associated with a third-order semi-implicit time stepping scheme described in Spalart et al. [1991]. The singularity at the origin of the polar coordinate system is avoided by re-defining the radius from - 1 to 1 and using an even number of grid points in the radial direction [Heinrichs, 2004]. Three Sylvester equations are written, respectively, for $\Delta\Psi$, Ψ and u_x, associated with homogeneous Dirichlet boundary conditions and are solved using a Fortran code relying on an optimized Sylvester equation solver from the SLICOT numerical library [Jonsson and Kagstrom, 2003]. The BCs $\Psi = 0$ and $u_x = 0$ at the wall correspond, respectively, to no-penetration and no-slip in the axial direction. The no-slip BC in the azimuthal direction is enforced by adding particular solutions to the streamfunction, follow- ing the influence matrix method for linear equations [Peyret, 2002], such that the azimuthal velocity $u_\phi = -\partial\Psi/\partial\eta$ vanishes at the wall. Under deterministic forcing, the 2D/3C model is reduced to a set of two ordinary differential equations (ODEs) that are solved in MATLAB using spectral methods based on a Chebyshev polynomial expansion.

6.2 Simplified 2D/3C model with deterministic forcing

We begin by developing a simplified version of the 2D/3C model subject to a steady, deterministic forcing to study momentum transfer between the in-plane and axial velocities. The study of optimal disturbance growth in pipe flow by Schmid and Henningson [2001] demonstrated that the streamwise-constant mode with azimuthal wavenumber $n = 1$ is the most amplified based on an energy norm. Thus, we isolate this mode as a candidate perturbation contributing to the blunting of the velocity profile and consider a forcing with only this one mode in the azimuthal direction, namely

$$N_\psi = N(\eta)\sin\phi. \tag{36}$$

The streamfunction $\Psi(\eta,\phi)$ has the same azimuthal dependence as the forcing since its governing equation is linear i.e., $\Psi = \Psi_1(\eta)\sin\phi$. The axial velocity can be written in terms of a mean deviation from laminar u_0 and a zero-mean perturbation $u_1\cos\phi$ corresponding to the linear response of the system to the forcing,

$$u_x(\eta,\phi) = u_0(\eta) + u_1(\eta)\cos\phi. \tag{37}$$

The 2D/3C model can be simplified as follows to predict the steady state mean deviation from laminar, u_0, obtained with the deterministic forcing profile $N(\eta)$:

$$\left(\Delta_\eta - \frac{1}{\eta}\right)^2 \Psi_1 = -0.5ReN(\eta), \tag{38}$$

$$\left(\Delta_\eta - \frac{1}{\eta}\right) u_1 = 0.5Re\Psi_1 d_\eta(U + u_0), \tag{39}$$

$$\Delta_\eta u_0 = -0.5 Re(C\eta - d_\eta(\Psi_1 u_1)), \tag{40}$$

where $\Delta_\eta = \eta D_{\eta\eta} + d_\eta$ is the radial derivative component of the 2D Laplacian premultiplied by η and $D_\eta = \mathrm{d}/\mathrm{d}\eta$. In order to obtain the simplest model able to capture the blunting of the velocity profile, we can linearize equation 40 under the assumption of small amplitude forcing. The resulting model contains only one nonlinear term in one ODE, the other two ODEs being linear. The presence of at least one nonlinear term is required to obtain a change in mean flow since linear models always give the same mean flow as the one used for the linearization.

A simple inspection of equations 38-40 leads to the following observations. Conclusions similar to those of Reddy and Ioannou [2000] on the energy transfer between streamwise constant modes can be recovered, but this time in terms of momentum transfer and for the pipe instead of Couette flow. The mean turbulent mode u_0 cannot extract momentum from the laminar base flow and is sustained by the nonlinear interaction between the axial velocity perturbation u_1 and the streamfunction Ψ_1, i.e., the $d_\eta(\Psi_1 u_1)$ term in equation 40. The non-normality of the system manifests itself in the linear coupling between the laminar base flow and the streamfunction which amplifies the disturbances and generates the axial velocity perturbation u_1 by convection of streamwise momentum (see equation 39). The shape of the streamfunction determines the amount of blunting obtained for a given amplitude coefficient.

In order to advance further analytically, we write the streamfunction profile Ψ_1 as a Taylor series at the origin, i.e.,

$$\Psi_1 = \Sigma_{i=0}^{\infty} \alpha_i \eta^i, \tag{41}$$

and set $\alpha_0 = 0$ in order to enforce continuity in the limit of η tending to zero, recalling that $\Psi(\eta, \phi) = -\Psi(\eta, \phi + \pi)$. The forcing profile generating Ψ_1 is given by

$$N(\eta) = -\frac{1}{Re}\left(\partial_{\eta\eta} + \frac{1}{\eta} - \frac{1}{\eta^2}\right)^2 \Psi_1(\eta). \tag{42}$$

We rescale the coefficients α_i by α_1, i.e., $\Psi_1 = \alpha_1[\eta + \alpha_2\eta^2 + \alpha_3\eta^3 + \alpha_4\eta^4 + ...]$ and choose α_1 such that the change in mean flow induced by the forcing has the same amplitude at its maximum as in the experiments of den Toonder and Nieuwstadt [1997] at the same Reynolds number, in order to facilitate comparison of the results. Note that, depending on the streamfunction profile, the coefficient a1 is not necessarily small in which case the linearization of equation39 is no longer justified. In the following, we solve the nonlinear momentum balance for u_1 (Eq. (6)) regardless of the amplitude of α_1. A fundamental streamfunction profile $\Psi_1 = \alpha_1(\eta - 3\eta^3 + 2\eta^4)$ is obtained by truncating the series expansion to the fourth order term, enforcing the BCs $\Psi_1 = d\Psi_1/d\eta = 0$ at the wall, and requiring that the forcing be bounded at the origin.

Streamfunctions given by $\Psi_{1,a} = \Psi_1$, $\Psi_{1,b} = \Psi_1^2$ and $\Psi_{1,c} = \Psi_1^3$ were investigated in order to ascertain the ability of such simple functions to capture key aspects of the blunting of the mean profile and to identify the role of the radial streamfunction profile. The amplitude coefficients, α_1, were chosen such that the same amount of blunting is realized in each case, as described above in terms of the maximum deviation from laminar. The steady-state equations were solved with 64 grid points in the radial direction, and at a Reynolds number of 24 600, matching one of the pipe flow experiments of den Toonder and Nieuwstadt [1997]. A short convergence study showed that this resolution in the radial direction is sufficient since the maximum relative error com- pared to the solution computed on 192 grid points is less than one percent.

Figure 2 shows the radial forms of the three analytic streamfunctions, $\Psi_{1,ac}(\eta)$, and the respective resulting variations of the mean deviation from laminar. Streamfunction profiles $\Psi_{1,b}$ and $\Psi_{1,c}$ reach maximum amplitudes of about 0.05 and 0.25, respectively, in the core of the pipe, while in comparison $\Psi_{1,a}$ is relatively flat with a maximum amplitude of 0.0085. Despite such a wide variation in streamfunction amplitude between the three cases, the streamwise velocity profiles are remarkably similar. Even the simple streamfunction profile $\Psi_{1,a}$ leads to a good blunting of the velocity profile, in the sense that the general features of the mean pro- file are reproduced. The maxima of the velocity profiles are situated further from the wall compared to the experimental data [den Toonder and Nieuwstadt, 1997] which likely corresponds to the neglect of the influence of the small scales near the wall by the streamwise-constant model. The results obtained with the simplified 2D/3C model also show that the velocity profile is relatively independent of the radial shape of the forcing and streamfunction, i.e., the profile can be said to be robust to the shape of the streamfunction.

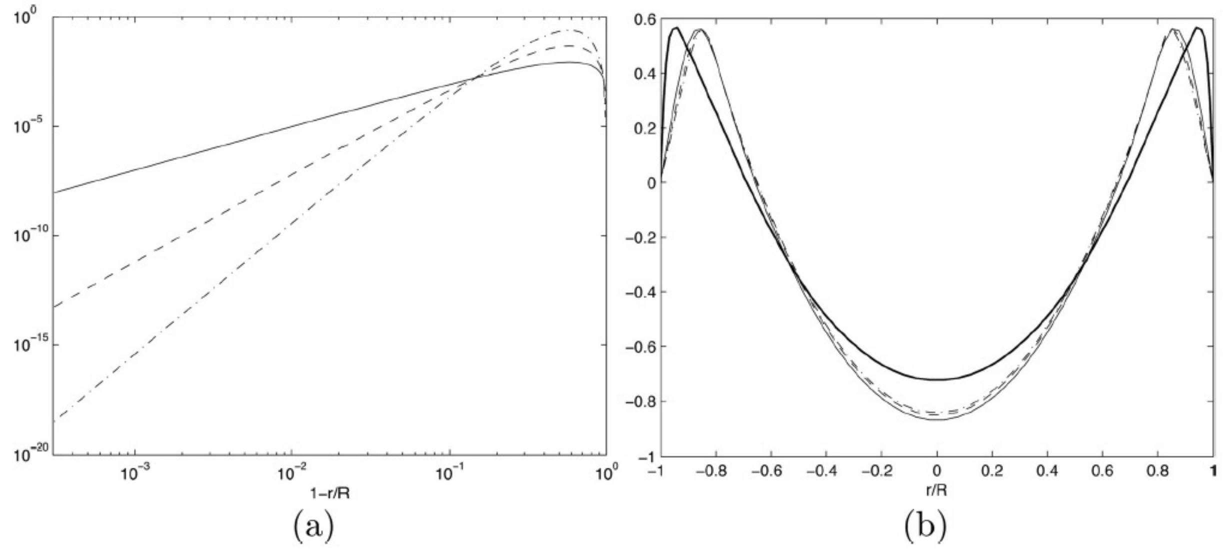

Figure 52: (a)Streamfunctions $\Psi_{1,a-c}(\eta)$ and (b) corresponding velocity profiles $u_0(\eta)$ for $\Psi_{1,a}(\eta) = 0.033(\eta - 3\eta^3 + 2\eta^4)$ (thin solid), $\Psi_{1,b}(\eta) = 0.7(\eta - 3\eta^3 + 2\eta^4)^2$ (dashed), and $\Psi_{1,c}(\eta) = 14(\eta - 3\eta^3 + 2\eta^4)^3$ (dash-dot) and experimental velocity profile of den Toonder and Nieuwstadt [1997] at $Re = 24600$ (thick solid).

The in-plane kinetic energy, defined as the integral of $u_r^2/2 + u_\phi^2/2$ over the pipe cross section, varies from $3.7x10^{-4}$ for $\Psi_{1,a}$ to 0.31 for $\Psi_{1,c}$ even though the same amount of blunting is realized by the three streamfunctions $\Psi_{1,ac}$. This large variation of the in-plane kinetic energy between different streamfunctions (about 3 orders of magnitude) can be understood by consideration of the influence of the near-wall region in the pipe on the overall amplification. Amplification is proportional to the mean shear and surface area, which are both maximum at the wall. Hence, the streamfunction $\Psi_{1,c}$ having a small amplitude near the wall compared to $\Psi_{1,a}$, see Figure 52, does not benefit from the near-wall effects as much as $\Psi_{1,a}$ and needs to reach a larger amplitude in the core (about 30 times larger) in order to give the same amount of blunting as $\Psi_{1,a}$, resulting in a significantly larger in- plane kinetic energy.

The large amplitude reached by $\Psi_{1,c}$ in the core of the pipe results in a maximum radial velocity amplitude of 64% of the bulk velocity compared to 3.3% for $\Psi_{1,a}$, significantly larger than the radial velocity turbulence intensity measured by den Toonder and Nieuwstadt [1997] which is about 1 plus unit or equivalently about 5% of the bulk velocity. A streamfunction that maintains a forcing amplitude comparable to the experimental noise level should, therefore, have a larger amplitude near the wall and relatively constant amplitude over the whole domain. A similar conclusion can be obtained by considering that blunting results from the advection of axial momentum by the radial velocity so that a large amount of blunting is realized when large radial velocities are present. Taking into account that the radial velocity depends on the azimuthal velocity via the continuity constraint, it can be seen that maximization of the ratio

suggests that the flattest streamfunction profile (or equivalently the simplest radial dependence results in the largest amplification. In terms of structures, the largest structures corresponding to the modes with the least zero crossings in the radial direction are more able to redistribute momentum over the cross-section of the pipe. The impor- tance of the modes with the least zero crossings is a known feature of turbulent pipe flow: modes with a radial quantum number of 1 in the study of Duggleby et al. [2007] were shown to capture most of the energy in their dynamical eigenfunction decomposition of turbulent pipe flow. Likewise, the singular modes that are most amplified in the study of McKeon and Sharma [2010] exhibit the lowest number of zero crossings.

Based on our numerical study, the streamfunction $\Psi(\eta) = 0.033(\eta - 3\eta^3 + 2\eta^4)\sin\phi$ leads to a blunting of the velocity profile whose maximum amplitude matches the experimental data at the same Reynolds number and is generated by a forcing profile $N(\eta) = -90/Re$ that is constant in the radial direction and whose

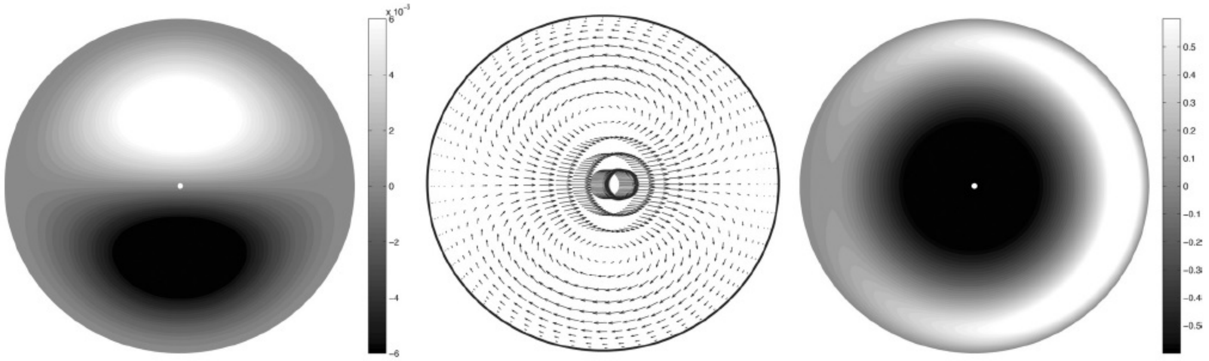

(a) (b) (c)

Figure 53: Model output for deterministic forcing: (a) contours of the streamfunction $\Psi_{1,a}(\eta) = 0.033(\eta - 3\eta^3 + 2\eta^4)\sin\phi$, (b) vector plot of the corresponding in- plane velocities, and (c) contours of the resulting axial velocity field.

amplitude over the pipe cross-section is consistent with the experimentally measured rms amplitude of the turbulence fluctuations. The contours of the streamfunction $\Psi(\eta) = 0.033(\eta - 3\eta^3 + 2\eta^4)\sin\phi$ are plotted on Figure 53 together with a vector plot of the corresponding in-plane velocities and the resulting contours of the axial velocity field. The streamfunction exhibits two counter-rotating rolls which advect the mean shear to create a low- and a high-speed streak of axial velocity defined with respect to the laminar base flow. The high-speed streak sits near the wall whereas the low-speed streak is localized near the centerline. Hence, the flow is on average faster near the wall and slower at the center compared to laminar as is the case for the velocity profile of turbulent pipe flow. The amplification factor between the in-plane and streamwise velocities, defined as the ratio of the extrema, is about 20 in this case.

As a final comment related to this simple, steady, deterministic streamfunction analysis, we note that when the azimuthal wavenumber is chosen to match the azimuthal dependence of the spatial puffs observed by Hof et al. [2004] and a new streamfunction model is derived along the lines described above, the velocity fields produced by our model are remarkably similar to the measured velocity fields near the trailing edge of the puffs. For an azimuthal wavenumber equal to six, the lowest order streamfunction profile that satisfies the BCs and is generated by a forcing profile bounded at the origin is given by $\Psi_6 = \alpha_1(\eta^4 - 2\eta^5 + \eta^6)$; figure 4 shows the resulting variation of the axial velocity. The wall-normal position of the high- and low-speed axial velocity streaks compares well with figures 2(e) and 2(f) in the paper by Hof et al. [2004]. Moreover, our model appears to capture the merging of the low-speed streaks and their congregation near the center of the pipe which is observed in experiments [Hof et al., 2004] but is not present in the traveling wave solutions of the NSE.

Despite the simplicity of the deterministic streamfunction profiles described in this section, key aspects of the axial velocity variation observed in experiments are recovered. In Sec. IV, we consider a more realistic, time-dependent forcing function in an effort to capture more details associated with the mechanisms of momentum transfer.

6.3 Stochastic forcing of the 2D/3C model

Effects that are not captured by the (unforced) 2D/3C model and external perturbations that are always present in experiments but not explicitly described by the NSE are likely much better captured by a stochastic forcing than a deterministic one. In this section, we present the results from a simulation of the 2D/3C model forced by small amplitude white noise, an approach which was successfully explored by Gayme et al. [2010] in Couette flow as well as several previous linear studies. Such stochastic forcing has the advantage over deterministic forcing of not relying on any assumption regarding the spatial and temporal dependence of the

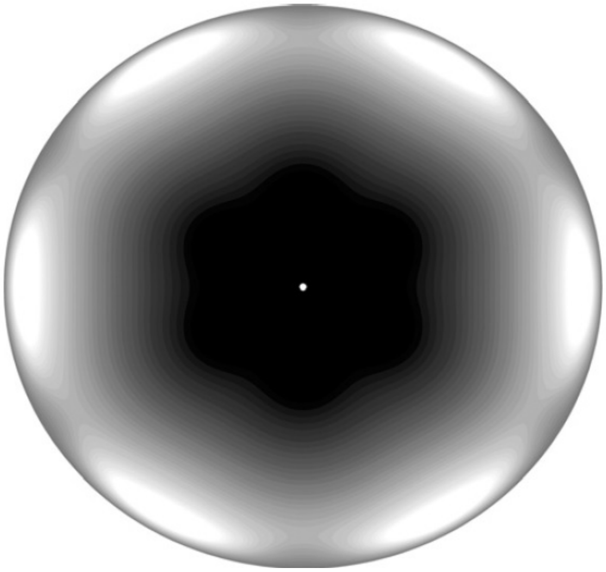

Figure 54: Contours of the axial velocity induced by the streamfunction $\Psi_6(\eta,\phi) = (\eta^4 - 2\eta^5 + \eta^6)\sin(6\phi)$, the light and dark filled contours correspond to regions of the flow, respectively, faster and slower than laminar.

perturbations, such that the resulting velocity field reflects the direction of maximum (assumed dominant) disturbance amplification. The noise, N_ϕ, is applied at each grid point in space and at every time step and follows a normal distribution with zero mean and a variance that depends on the radius such that the variance per surface area is constant. In order to prevent aliasing in the nonlinear coupling terms in the streamwise velocity equation, we truncate the 2D Fourier transform of the forcing term after the lowest two-third wavenumbers, as described in Canuto [2006].

Representative time traces of the centerline velocity for two different Reynolds numbers are reproduced on Figure 5 and show numerous sharp drops, which we identify as the signature of streamwise-constant puffs, before increasing smoothly nearly back to its laminar value. (Since there is no grid point at the centerline, we approximate the centerline velocity by averaging the axial velocity in the azimuthal direction over the grid points closest to the center of the pipe.) The signatures of the streamwise-constant puffs are remarkably similar to the spatial evolution of the centerline velocity from the trailing to the leading edge of the spatial puffs in the numerical simulations of Shimizu and Kida [2009]. We define a puff generation timescale as the time elapsed between two sharp drops of the centerline velocity. At $Re = 2200$, the timescale is about 75 dimensionless time units based on the pipe radius and compares well with the time scale of puffs computed from experimental data[Nishi et al., 20078], in which the puffs are 5 to 20 diameters long depending on Reynolds number and convect at nearly the bulk velocity. A puff of length 20D which is separated from the next puff by a laminar region of length equivalent to one puff would lead to a dimensionless timescale based on the pipe radius of 80.

The puff generation timescale is an increasing function of the Reynolds number, reflecting the fact that puffs tend to be longer in experiments as the Reynolds number increases Figures 5(a) and 5(b), reaching 330 at $Re = 10000$, but is relatively independent of the noise amplitude Figures 5(a) and 5(c). The drop in centerline velocity associated with the trailing edge of a puff can be observed to be sharper and stronger for larger forcing amplitudes. Note that if we relax the BCs to allow for slip in the azimuthal direction, i.e., we use a shear-stress free condition (not shown), the simulations capture the creation of streamwise vortices and streaks as well as the blunting of the velocity profile, but we do not observe clearly the cyclic generation of puffs in the time evolution of the full velocity field or their signature in the time traces of the centerline velocity. However, for a given forcing amplitude, the amount of blunting realized with the slip BC in the azimuthal direction is larger than with no-slip.

The time evolution of the flow field is characterized by the quasi-periodic generation of streamwise-constant

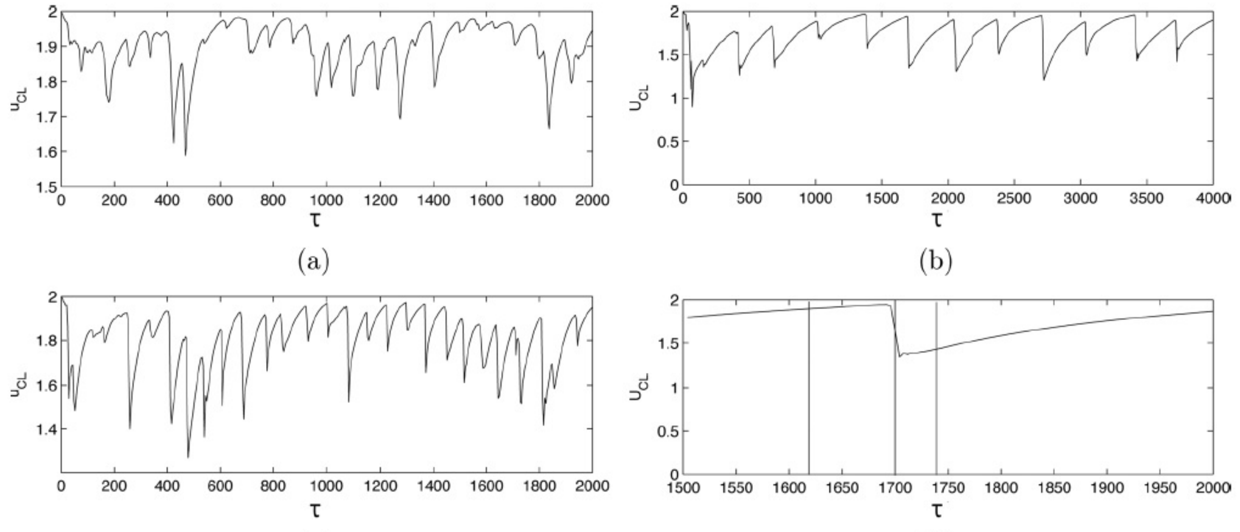

(a) (b)

(c) (d)

Figure 55: Time traces of the centerline velocity from three different simulations, respectively, at $Re = 2200$ with 0.0005 and 0.002 rms noise levels (a) and (c) and at $Re = 10000$ with 0.002 rms noise level (b). The resolution in the radial direction is $N = 48$. (d) Zoom on the time interval during which the samples of Figure 6 are taken. The vertical lines indicate the sampling instants.

puffs followed by their decay and the return of the flow close to the laminar state, i.e., each bursting event is followed by quiescent flow equivalent to the laminar regions that separate the puffs in the experiments of Lindgren [1957]. The three main stages in the evolution of the flowfield corresponding to a streamwise-constant puff are plotted on Figure 6 in terms of the axial velocity ((a) to (c)) and the swirling strength ((d) to (f)), defined as the magnitude of the imaginary part of the in-plane velocity gradient eigenvalues and representative of coherent vorticity without the influence of mean shear. These instantaneous fields correspond to the time instants marked with vertical lines in Figure 5(d). During the first stage, patches of swirl move toward the center of the pipe Figures 6(d) and 5(e) and create streaks by convection of the axial momentum Figure 6(a). The radial motion of the coherent swirl corresponds to a lift up of streamwise vortices away from the wall as observed in the simulations of van Doorne and Westerweel [2009] if we consider the evolution of the vorticity field projected in a plane moving at the bulk velocity. The second stage consists of the segregation of the high- and low-speed streaks, the latter being convected toward the center of the pipe resulting in the blunting of the velocity profile characteristic of turbulent pipe flow, Figure 6(b). Once a low-speed streak reaches the center, the centerline velocity drops sharply, as can be seen on the time traces on Figure 5(b). Finally, the swirling strength and streaks decay Figures 6(c) and 6(f) and the flow returns close to the laminar state before the next cycle starts. As the streamwise vortices convect toward the center of the pipe, the sign of the net azimuthal velocity is reversed such that the rotation sign changes from one cycle to the next.

While the output of the 2D/3C model is a temporal variation of a streamwise constant field, a simplistic comparison with spatial experimental results may be made by assuming an appropriate convection velocity to be the bulk velocity. With this in mind, the time evolution of the velocity field is remarkably similar to the flow visualizations by Hof et al. [2004] in transitioning pipe flow when a puff is observed in a reference frame moving with the bulk velocity. Streak merging in experiments was reported by those authors, who showed that the number of streaks in the cross-section decreases due to their merging as the cross-stream observation plane is moved from the trailing edge to the leading edge of a puff. This streak merging, as well as the segregation of the high- and low-speed streaks observed in the experiments is accurately reproduced by the model, as shown in Figure 5. The time evolution of the vorticity field in our simulations is also consistent with the projection of the 3-dimensional vorticity field inside the puff computed by van Doorne and Westerweel [2009] in a plane moving at the bulk velocity, characterized by a lift up of streamwise vortices

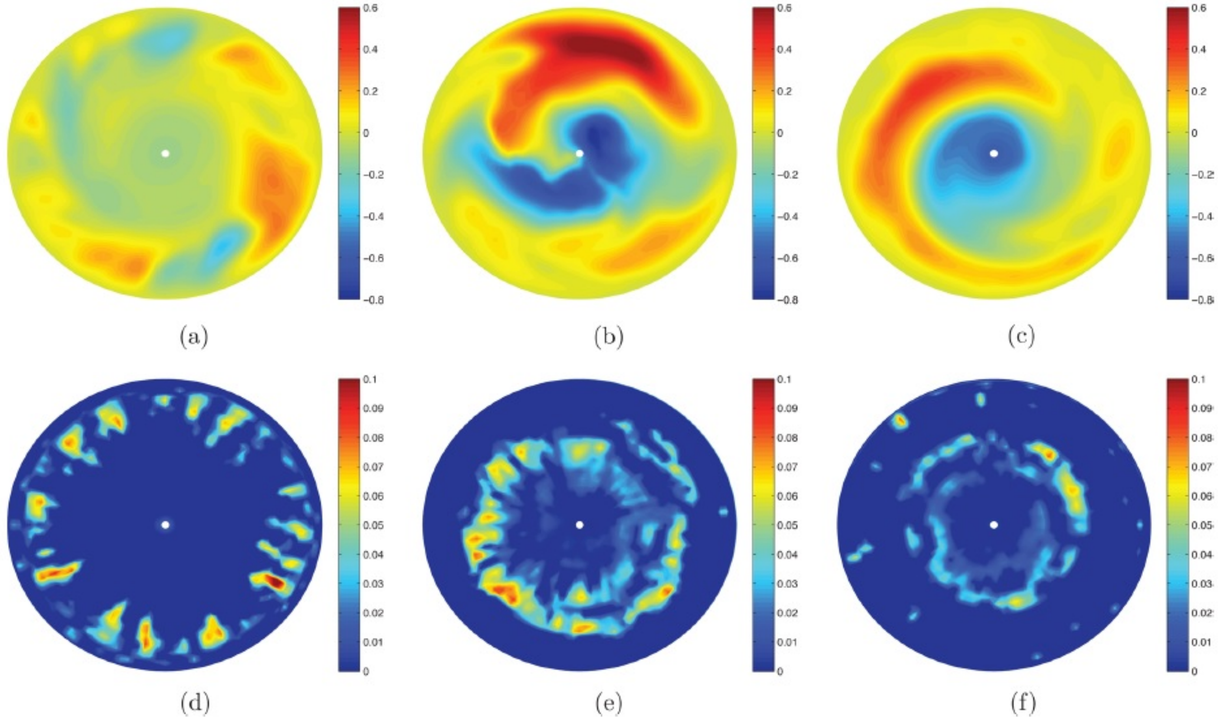

(a) (b) (c)

(d) (e) (f)

Figure 56: Contours of the axial velocity, subfigures (a) to (c), and of the swirling strength for the in-plane velocities, subfigures (d) to (f), computed, respectively, at = 1620, $t = 1700$, and $t = 1740$ dimensionless time units.

away from the wall as we move from the trailing to the leading edge of the puff (corresponding to increasing time in our model).

The generation and subsequent decay of the puffs can be described in terms of a simple process driven by background noise, sketched in the inner loop of Figure 7. In essence, the presence of background noise in the pipe cross-section results in the formation of streamwise-constant vortices which advect axial momentum to create high- and low-speed streaks of axial velocity. The vortices interact nonlinearly with the streaks to segregate them, i.e., to convect the low-speed streaks toward the center and the high-speed streaks toward the wall, leading to the blunting of the velocity profile. We term this a quasi-self-sustaining process (QSSP) to reflect the fact that, while there is no feedback from the axial velocity to the evolution of the streamfunction (denoted by the dashed line in the inner loop of Figure 7) which could sustain the cycle described in Figure 6, the insertion of small-amplitude stochastic forcing in the cross-stream plane appears to provide an effective replacement for this mechanism. The radial shape of the forcing is directly related to the amount of swirl present in the simulations and, therefore, suggests a method to control the flow by shaping the noise forcing in the spirit of the simple control mechanism developed by Hof et al. [2010] which reduces the inflection points of the velocity profile and leads to a relaminarization of the flow.

A well-studied, fully self-sustaining process has been described for the (3D/3C) NSE by Waleffe [1997], which relies on the nonlinear interaction of the disturbances developing from the instability of the streaks to force the stream- wise vortices. Our results suggest that the blunting of the velocity profile can be considered to be, in essence, a nonlinear, two-dimensional phenomenon in which the directional amplification of the 2D/3C model selects the appropriate disturbance shape from stochastic forcing in order to maintain the QSSP. The model suggests that the sustaining mechanisms are, therefore, insensitive to the type of (nonlinear) interaction invoked to force the streamwise vortices. Based on the simulations presented here, we argue that it is the presence of appropriate, small disturbances in the flow (necessarily contained in the white noise of stochastic forcing), and not their specific interaction that sustains the streamwise vortices and streaks. Hence, the 2D/3C model shows that using unstructured (stochastic) forcing to generate the streamwise

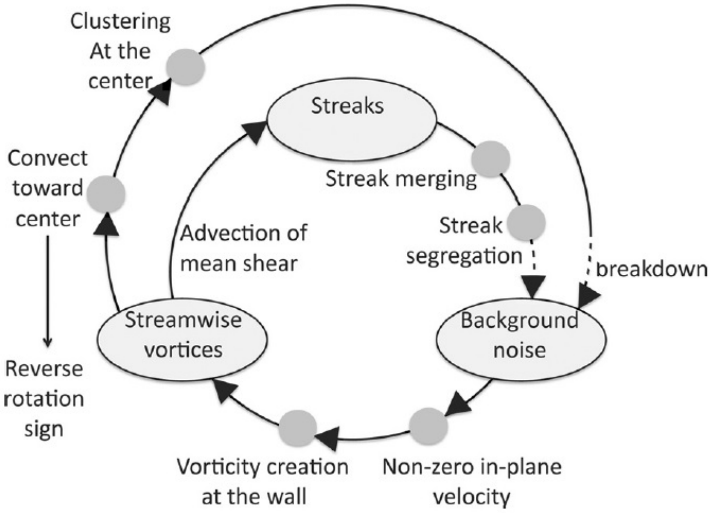

Figure 57: Diagram detailing the different stages of the QSSP. The dashed lines represent unmodeled effects.

vortices appears to be sufficient to capture the formation of the streaks and their segregation resulting in a blunting of the velocity profile and that the overall flow dynamics are relatively insensitive to the particular regeneration process invoked to produce the stream-wise vortices. The QSSP is simpler than other processes described in the literature but does appear to capture the minimum turbulence dynamics and produce flow fields dominated by streamwise vortices and streaks whose temporal evolution and topology compares well to experimental visualizations and numerical simulations of puffs, under an appropriate projection onto a plane convecting at the bulk velocity. In addition, our simulations are significantly less computationally intensive than studies of the full NSE[van Doorne and Westerweel, 2009, Shimizu and Kida, 2009] since our domain is 2D and we do not need to track the position of the puffs in time.

Interestingly, our simulations of the stochastically forced 2D/3C model for pipe flow do not reach fully developed turbulence, regardless of the amount of forcing and Reynolds number, even though the same model applied to Couette flow and described in Ref. 8 reached a steady state with a velocity profile in good agreement with the profiles from full 3D simulations at the same Reynolds number, provided that the amount of forcing is appropriately chosen. Mellibovsky et al. [2009] describe pipe flow transition as a two-stage process, the first stage consists in the formation of the puffs and the second in their spreading in space. Those authors argue that the two stages are caused by different instability mechanisms. Our simulations support this point of view since we are able to capture the first stage using a streamwise-constant model but not the second stage for which three-dimensional effects are necessary to allow for the puffs to destabilize and form slugs which will expand to cover the whole flow domain.

6.4 Summary

We have investigated a (globally stable) streamwise-constant, 2D/3C model of turbulent pipe flow subject to two types of very simple forcing profiles, namely a deterministic, steady streamfunction, and stochastic forcing of the stream-function equation. By retaining (only) the nonlinearity coupling the (cross-plane) streamfunction and the axial velocity, the model permits the study of the physics underlying mo- mentum transfer. This model, which is significantly more tractable than the full Navier-Stokes equations, appears to be capable of capturing key features associated with transition to turbulence, i.e., the blunting of the velocity profile and the generation of streamwise vortices and streaks.

Using the simplest, time-invariant deterministic forcing, we showed that the velocity profile is robust with respect to variations in the forcing profile and we produced realistic velocity fields that are remarkably similar to the flow visualizations by Hof et al. [2004] near the trailing edge of a puff. Thanks to the significant reduction in complexity associated with the 2D/3C projection compared to the full Navier-Stokes equations, several observations can be made by examination of the governing equations: momentum is extracted from the laminar base flow by (zero-mean) perturbations via linear non-normal mechanisms and redistributed via nonlinear interactions of the perturbations to result in a change in mean flow. Hence, our simplistic model allowed us to isolate basic mechanisms leading to the blunting of the velocity profile in pipe flow.

Under stochastic forcing, the model generates "streamwise-constant puffs" at a frequency that depends on the Reynolds number but not on the forcing amplitude. The model captures the first stage of pipe flow transition as described by Mellibovsky et al. [2009], i.e., the formation of puffs but not the second stage (spreading of the puffs in space) for which some three-dimensional effects are necessary. The time evolution of the velocity fields produced by our simulations is remarkably similar to flow visualizations in transitioning pipe flow [Hof et al., 2004] when a puff is observed in a reference frame moving at the bulk velocity. The segregation of the high- and low-speed streaks observed in experiments is accurately captured by the model as well as the streak merging and the lift up of the streamwise vortices away from the wall.

The essential dynamics governing the generation of puffs in pipe flow transition were captured by the streamwise-constant model and are relatively insensitive to the particular regeneration mechanisms invoked to produce the streamwise vortices, permitting the introduction of a quasi self-sustaining process to describe the generation of puffs and the blunting of the mean velocity profile.

7 Conclusions and Outlook

This PECASE award has enabled the development of resolvent analysis for wall turbulence, a promising approach to understanding, and ultimately controlling flows of interest to a range of Air Force vehicles. In addition, experiments and modeling have been performed to support the analysis and provide appropriate input parameters and profiles. We have described here how a straightforward analysis permits significant simplifications in complexity, dimension, and interpretation of the NSE. The most important of these may be the low dimensionality and sparse nature of the formulation, which open the door to the use of state-of-the-art mathematical tools including compressed sampling and techniques for low rank matrix approximation of linear operators [Sharma, 2009]. A study in a turbulent channel [Moarref et al., 2013], enabled by an efficient randomized algorithm for the approximation of the SVD of low rank operators [Halko et al., 2011], gives encouraging results with respect to utilizing the low rank nature of the resolvent for both prediction and modeling purposes: it appears that a very good approximation to the distribution of streamwise turbulent intensity (the dominant contributor to the turbulent kinetic energy) can be obtained using only the first two singular modes and extraordinarily simple assumptions about the amplitude distribution in K space. The sparse nature of the modes identified as being active in real flows in the frequency domainBourguignon et al. [2013] naturally leads to consideration of compressive sampling as a tool for data reduction [Bourguignon et al., 2014a]. Additionally, the resolvent analysis may have implications for simulation, since the frequency domain representation effectively captures aspects of the dynamics that are masked in the time domain, i.e. by time-stepping approaches. This grant has seeded several ongoing collaborative effort aimed at utilizing resolvent analysis towards control of wall turbulence. We propose that the success of the resolvent analysis described here for incompressible, Newtonian flow in canonical flow configurations suggests promise for generalization to more complex flows. In particular, work is ongoing to consider adaptation of the formulation to consider rough-wall, non-Newtonian and compressible flows, and spatial inhomogeneity. This will facilitate understanding and control of a broad range of practical and applied flows.

8 References

References

R. J. Adrian. Statistical properties of particle image velocimetry measurement in turbulent flow. In Laser Anemometry in Fluid Mechanics III, pages 115–129. LADOAN-Instituto Superior Técnico, 1988.

R. J. Adrian. Vortex organization in wall turbulence. Phys. Fluids, 19(041301), 2007.

R. J. Adrian, C. D. Meinhart, and C. D. Tomkins. Vortex organization in the outer region of the turbulent boundary layer. J. Fluid Mech., 422:1–54, 2000.

B. J. Balakumar and R. J. Adrian. Large- and very-large-scale motions in channel and boundary-layer flows. Phil. Trans. Royal Soc. A, 365:665–681, 2007.

B. Bamieh and M. Dahleh. Energy amplification in channel flows with stochastic excitation. Phys. Fluids, 13(11):3258–3269, 2001.

P. Bandyopadhyay and M. R. Head. Visual investigation of turbulent boundary layer structure. Cambridge University Engng Dept Film, 1979.

K.M. Bobba. Robust Flow Stability: Theory, Computations and Experiments in Near Wall Turbulence. PhD thesis, California Institute of Technology, 2004.

J.-L. Bourguignon and B. J. McKeon. A streamwise-constant model of turbulent pipe flow. Phys. Fluids, 23(095111), 2011.

J.-L. Bourguignon, A. S. Sharma, J. A. Tropp, and B. J. McKeon. Compact representation of wall-bounded turbulence using compressive sampling. arXiv, abs/1301.7580, 2013.

J.-L. Bourguignon, A. S. Sharma, and B. J. McKeon. Sparse representations of turbulent pipe flow using a model-based radial basis. In preparation, 2014a.

J.-L. Bourguignon, A. S. Sharma, J. A. Tropp, and B. J. McKeon. Compact representation of wall-bounded turbulence using compressive sampling. Phys. Fluids, 26(015109), 2014b.

K Butler and B Farrell. Three-dimensional optimal perturbations in viscous shear flow. Phys. Fluids, 4(8), August 1992a.

K. Butler and B. Farrell. Optimal perturbations and streak spacing in wall-bounded turbulent shear flow. Phys. Fluids, A5:774–777, 1992b.

C. Canuto. Spectral methods: Fundamentals in Single Domains. Springer, New York, 2006.

J. Carlier and M. Stanislas. Experimental study of eddy structures in a turbulent boundary layer using particle image velocimetry. J. Fluid Mech., 535:143–188, 2005.

P. Chakraborty, S. Balachandar, and R. J. Adrian. On the relationships between local vortex identification schemes. J. Fluid Mech., 535:189–214, 2005.

M.S. Chong, A. E. Perry, and B. J. Cantwell. A general classification of three-dimensional flow fields. Phys. Fluids A, 2(5):765–777, 1990.

D. Chung and B. J. McKeon. Large-eddy simulation investigation of large-scale structures in a long channel flow. J. Fluid Mech., 661:341–364, 2010.

C. Cossu, G. Pujals, and S. Depardon. Optimal transient growth and very large scale structures in turbulent boundary layers. J. Fluid Mech., 619:79–94, 2009.

D. B. DeGraaff and J. K. Eaton. Reynolds-number scaling of the flat-plate turbulent boundary layer. J. Fluid Mech., 422:319–346, 2000.

J. C. del Álamo and J. Jiménez. Direct numerical simulation of the very large anisotropic scales in a turbulent channel. Center for Turbulence Research: Annual Research Briefs, 2001:329–341, 2001.

J. C. del Álamo and J. Jiménez. Linear energy amplification in turbulent channels. J. Fluid Mech., 559: 205–213, 2006.

J. C. del Álamo and J. Jiménez. Estimation of turbulent convection velocities and corrections to Taylor's approximation. J. Fluid Mech., 640:5–26, 2009.

J. C. del Álamo, J. Jiménez, P. Zandonade, and R. D. Moser. Self-similar vortex clusters in the turbulent logarithmic region. J. Fluid Mech., 561:329–358, 2006.

J. M. J. den Toonder and F. T. M. Nieuwstadt. Reynolds number effects in a turbulent pipe flow for low to moderate Re. Phys. Fluids, 9:3398–3409, 1997.

D. Dennis and T. Nickels. On the limitations of Taylor's hypothesis in constructing long structures in wall-bounded turbulent flow. J. Fluid Mech., 614:197–206, 2008.

D. Dennis and T. Nickels. Experimental measurement of large-scale three-dimensional structures in a turbulent boundary layer. Part 2. Long structures. J. Fluid Mech., 673:218–244, 2011a.

D. Dennis and T. Nickels. Experimental measurement of large-scale three-dimensional structures in a turbulent boundary layer. Part 1. Vortex packets. J. Fluid Mech., 673:180–217, 2011b.

A. Duggleby, K. S. Ball, M. R. Pail, and P. F. Fischer. Dynamical eigenfunction decomposition of turbulent pipe flow. J. Turbulence, 8(43):1–24, 2007.

B. Eckhardt, T. M. Schneider, B. Hof, and J. Westerweel. Turbulence transition in pipe flow. Annu. Rev. Fluid Mech., 39(1):447–468, 2007. doi: 10.1146/annurev.fluid.39.050905.110308.

G. E. Elsinga and I. Marusic. Evolution and lifetimes of flow topology in a turbulent boundary layer. Phys. Fluids, 22, 2010.

G. E. Elsinga, C. Poelma, A. Schröder, R. Geisler, F. Scarano, and J. Westerweel. Tracking of vortices in a turbulent boundary layer. J. Fluid Mech, 697:273–295, 2012.

L. P. Erm and P. N. Joubert. Low-Reynolds-number turbulent boundary layers. J. Fluid Mech., 230:1–44, 1991.

B. F. Farrell and P. J. Ioannou. Perturbation structure and spectra in turbulent channel flow. Theor. Comput. Fluid Dynamics, 11:237–250, 1998.

O. Flores and J. Jiménez. Effect of wall-boundary disturbances on turbulent channel flows. J. Fluid Mech., 566:357–376, 2006.

J. M. Foucaut, J. Carlier, and M. Stanislas. PIV optimization for the study of turbulent flow using spectral analysis. Meas. Sci. and Tech., 15:1046–1058, 2004.

B. Ganapathisubramani, E. K. Longmire, and I. Marusic. Characteristics of vortex packets in turbulent boundary layers. J. Fluid Mech., 478:35–46, 2003.

B. Ganapathisubramani, E. K. Longmire, and I. Marusic. Experimental investigation of vortex properties in a turbulent boundary layer. Phys. Fluids, 18, 2006.

Q. Gao, C. Ortiz-Dueñas, and E. K. Longmire. Analysis of vortex populations in turbulent wall-bounded flows. J. Fluid Mech., 678:87–123, 2011.

D. F. Gayme, B. J. McKeon, A. Papachristodolou, B. Bamieh, and J. C. Doyle. Streamwise constant model of turbulence in plane Couette flow. J. Fluid Mech., 665:99–119, 2010.

V.W. Goldschmidt, M.F. Young, and E.S. Ott. Turbulent convective velocities (broadband and wavenumber dependent) in a plane jet. J. Fluid Mech., 105:327–345, 1981.

F. Gómez Carrasco, H. Blackburn, M. Rudman, B. McKeon, M. Luhar, R. Moarref, and A. Sharma. On the origin of frequency sparsity in direct numerical simulations of turbulent pipe flow. Phys. Fluids, 26 (101703), 2014.

M. Guala, M. J. Metzger, and B. J. McKeon. Interactions within the turbulent boundary layer at high Reynolds number. J. Fluid Mech., 666:573–604, 2010.

N. Halko, P. G. Martinsson, and J. A. Tropp. Finding structure with randomness: Probabilistic algorithms for constructing approximate matrix decompositions. SIAM Review, 53(2):217–288, 2011.

M. R. Head and P. Bandyopadhyay. New aspects of turbulent boundary-layer structure. J. Fluid Mech., 107:297–338, 1981.

W. Heinrichs. Spectral collocation schemes on the unit disk. J Comp. Phys., 199(1):66, 2004.

D S Henningson and S C Reddy. On the role of linear mechanisms in transition to turbulence. Phys. Fluids, 6(3), March 1994.

B. Hof, C. W. H. van Doorne, J. Westerweel, F. T. M. Nieuwstadt, H. Faisst, B. Eckhardt, H. Wedin, R. R. Kerswell, and F. Waleffe. Experimental observation of nonlinear traveling waves in turbulent pipe flow. Science, 305(5690):1594, 2004.

B. Hof, A. de Lozar, M. Avila, X. Tu, and T. M. Schneider. Eliminating turbulence in spatially intermittent flows. Science, 327:1491–1494, 2010.

S. Hoyas and J. Jimenez. Scaling of the velocity fluctuations in turbulent channels up to $re_\tau = 2003$. Phys. Fluids, 18(1):011702, 2006.

J. C. R. Hunt, A. A. Wray, and P. Moin. Eddies, stream, and convergence zones in turbulent flows. Center for Turbulence Research Report, CTR-S88:193–208, 1988.

N. Hutchins and I. Marusic. Large-scale influences in near-wall turbulence. Phil. Trans. Royal Soc. A, 365: 647–664, 2007.

N. Hutchins, W. T. Hambleton, and I. Marusic. Inclined cross-stream stereo particle image velocimetry measurements in turbulent boundary layers. J. Fluid Mech., 541:21–54, 2005.

Y. Hwang and C. Cossu. Linear non-normal energy amplification of harmonic and stochastic forcing in the turbulent channel flow. J. Fluid Mech., 664:51–73, 2010.

I. Jacobi and B. J. McKeon. Dynamic roughness perturbation of a turbulent boundary layer. J. Fluid Mech., 668:258–296, 2011.

I. Jacobi, M. Guala, and B. J. McKeon. Characteristics of a turbulent boundary layer perturbed by spatially-impulsive dynamic roughness. AIAA-2010-4474, 2010.

J. Jeong and F. Hussain. On the identification of a vortex. J. Fluid Mech., 285:69–94, 1995.

J. Jiménez and A. Pinelli. The autonomous cycle of near-wall turbulence. J. Fluid Mech., 389:335–359, 1999.

J. Jiménez, J. C. del Álamo, and O. Flores. The large-scale dynamics of near-wall turbulence. J. Fluid Mech., 505:179–199, 2004.

I. Jonsson and B. Kagstrom. Recsy - A high performance library for Sylvester-type matrix equations. In Proceedings of the Euro-Par 2003 Parallel Processing, volume 2790, pages 810–819, 2003.

D. D. Joseph and L. N. Tao. Transverse velocity components in fully developed unsteady flows. J. Appl. Mech., 30:147, 1963.

M. R. Jovanovic and B. Bamieh. Componentwise energy amplification in channel flows. J. Fluid Mech., 534: 145–183, 2005.

MR Jovanovic and B. Bamieh. Frequency domain analysis of the linearized Navier-Stokes equations. Proceedings of the American Control Conference, 4, 2003.

R. D. Keane and R. J. Adrian. Optimisation of particle image velocimeters - Part I: double pulsed systems. Meas. Sci. Technol., 1:1202–1215, 1990.

R R Kerswell. Recent progress in understanding the transition to turbulence in a pipe. Nonlinearity, 18(6): R17, 2005. URL `http://stacks.iop.org/0951-7715/18/i=6/a=R01`.

J. Kim and F. Hussain. Propagation velocity of perturbations in turbulent channel flow. Phys. Fluids A, 5 (3):695–706, 1993.

J. Kim, P. Moin, and R. Moser. Turbulence statistics in fully developed channel flow at low Reynolds number. J. Fluid Mech., 177:133–166, 1987.

K. C. Kim and R. J. Adrian. Very large-scale motion in the outer layer. Phys. Fluids, 11(2):417–422, 1999.

J. C. Klewicki, M. M. Metzger, E. Kelner, and E. M. Thurlow. Viscous sublayer flow visualizations at $R_\theta \sim 1500000$. Phys. Fluids, 7:857–863, 1995.

S. J. Kline, W. C. Reynolds, F. A. Schraub, and P W. Runstadler. The structure of turbulent boundary layers. J. Fluid Mech., 30:741–772, 1967a.

S. J. Kline, W. C. Reynolds, F. A. Schraub, and P. W. Runstadler. The structure of turbulent boundary layers. J. Fluid Mech., 30:741–773, 1967b.

P. -Å. Krogstad, J. H. Kaspersen, and S. Rimestad. Convection velocities in a turbulent boundary layer. Phys. Fluids, 10(4):949–957, 1998.

J. LeHew, M. Guala, and B. J. McKeon. A study of convection velocities in a zero pressure gradient turbulent boundary layer. AIAA-2010-4474, 2010.

J. LeHew, M. Guala, and B. J. McKeon. A study of the three-dimensional spectral energy distribution in a zero pressure gradient turbulent boundary layer. Exp. Fluids, 51(4):997–1012, 2011.

J. LeHew, M. Guala, and B. J. McKeon. Time-resolved measurements of coherent structure in the turbulent boundary layer. Exp. Fluids, 54(1508), 2013.

J Lim and J Kim. A singular value analysis of boundary layer control. Phys. Fluids, 16(6), June 2004.

E. R. Lindgren. The transition process and other phenomena in viscous flow. Arkiv for Fysik, 12:1, 1957.

A. Lozano-Duran, O. Flores, and J. Jiménez. Three-dimensional structure of momentum transfer in turbulent channels. J. Fluid Mech., 694:100–130, 2012.

W. V. R. Malkus. Outline of a theory of turbulent shear flow. J. Fluid Mech., 1(05):521–539, 1956. doi: 10.1017/S0022112056000342.

I. Marusic, B. J. McKeon, P. A. Monkewitz, H. M. Nagib, A. J. Smits, and K. R. Sreenivasan. Wall-bounded turbulent flows at high Reynolds numbers: Recent advances and key issues. Phys. Fluids, 22, 2010.

S A Maslowe. Critical layers in shear flows. Annu. Rev. Fluid Mech., 18(1):405–432, 1986. doi: 10.1146/annurev.fl.18.010186.002201.

R. Mathis, N. Hutchins, and I. Marusic. Large-scale amplitude modulation of the small-scale structures of turbulent boundary layers. J. Fluid Mech., 628:311–337, 2009.

B. J. McKeon and A. S. Sharma. A critical layer model for turbulent pipe flow. J. Fluid Mech., 658:336–382, 2010.

B. J. McKeon, J. Li, W. Jiang, J. F. Morrison, and A. J. Smits. Further observations on the mean velocity distribution in fully developed pipe flow. J. Fluid Mech., 501:135–147, 2004.

B. J. McKeon, A. S. Sharma, and I. Jacobi. Predicting structural and statistical features of wall turbulence. ArXiV, 1012-0426, 2010.

B. J. McKeon, A. S. Sharma, and I. Jacobi. Experimental manipulation of wall turbulence: a systems approach. Phys. Fluids, 25(031301), 2013.

F. Mellibovsky, A. Meseguer, T. M. Schneider, and B. Eckhardt. Transition in localized pipe flow turbulence. Phys. Rev. Lett., 103, 2009.

A. Meseguer and L. N. Trefethen. Linearized pipe flow to Reynolds number 10^7. J. Comp. Phys., 186: 178–197, 2003.

R. Moarref, A. S. Sharma, J. A. Tropp, and B. J. McKeon. Model-based scaling of the streamwise energy density in high-reynolds-number turbulent channels. J. Fluid Mech., 734:275–316, 2013.

R. Moarref, M. R. Jovanovic, J. A. Tropp, A. S. Sharma, and B. J. McKeon. A low-order representation of turbulent channel flow via resolvent analysis and convex optimization. Phys. Fluids, 26(051701), 2014a.

R. Moarref, A. S. Sharma, J. A. Tropp, and B. J. McKeon. A foundation for analytical developments in the logarithmic region of turbulent channels. (Under review), 2014b.

J. P. Monty. Developments in smooth wall turbulent duct flows. PhD thesis, University of Melbourne, 2005.

J. P. Monty and M. S. Chong. Turbulent channel flow: comparison of streamwise velocity data from experiments and direct numerical simulation. J. Fluid Mech., 633:461–474, 2009.

J. P. Monty, N. Hutchins, H. C. H. Ng, I. Marusic, and M. S. Chong. A comparison of turbulent pipe, channel and boundary layer flows. J. Fluid Mech., 632:431–442, 2009.

J. F. Morrison, W. Jiang, B. J. McKeon, and A. J. Smits. Scaling of the streamwise velocity component in turbulent pipe flow. J. Fluid Mech., 508:99–131, 2004.

W. R. B. Morrison and R. E. Kronauer. Structural similarity for fully developed turbulence in smooth tubes. J. Fluid Mech., 39(1):117–141, 1969.

W. R. B. Morrison, K. J. Bullock, and R. E. Kronauer. Experimental evidence of waves in the sublayer. J. Fluid Mech., 49(4):639–656, 1971.

V. K. Natrajan, Y. Wu, and K. T. Christensen. Spatial signatures of retrograde spanwise vortices in wall turbulence. J. Fluid Mech., 574:155–167, 2007.

M. Nishi, B. Uensal, F. Durst, and G. Biswas. Laminar to turbulent transition of pipe flows through puffs and slugs. J. Fluid Mech., 614:425, 20078.

A. E. Perry and M. S. Chong. On the mechanism of wall turbulence. J. Fluid Mech, 119:173–217, 1982.

A. E. Perry and I. Marusic. A wall-wake model for the turbulence structure of boundary layers. Part 1. Extension of the attached eddy hypothesis. J. Fluid Mech., 298:361–388, 1995.

A. E. Perry, S. Henbest, and M. S. Chong. A theoretical and experimental study of wall turbulence. J. Fluid Mech., 195:163–199, 1986.

R. Peyret. Spectral methods for incompressible viscous flow, volume 148. 2002.

S. C. Reddy and P. J. Ioannou. Energy transfer analysis of turbulent plane couette flow. In Springer-Verlag, editor, Proceedings of the IUTAM Laminar-Turbulent Transition, pages 211–216, 2000.

A. Savitzky and M. J. E. Golay. Smoothing and differentiation of data by simplified least squares procedures. Anal. Chem., 36(4):1627–1639, 1964.

P. J. Schmid. Nonmodal stability theory. Ann. Rev. Fluid Mech., 39:129–162, 2007.

P J Schmid and D S Henningson. Stability and Transition in Shear Flows. Springer-Verlag, New York, 2001.

W. Schoppa and F. Hussain. Coherent structure generation in near-wall turbulence. J. Fluid Mech., 453: 57–108, 2002.

M. P. Schultz and K. A. Flack. Reynolds-number scaling of turbulent channel flow. Phys. Fluids, 25(025104), 2013.

A. S. Sharma. Model reduction of turbulent fluid flows using the supply rate. Int. J. Bifurcat. Chaos, 19(04):1267, 2009. ISSN 0218-1274. doi: 10.1142/S0218127409023615. URL `http://www.worldscientific.com/doi/abs/10.1142/S0218127409023615`.

A. S. Sharma and B. J. McKeon. On coherent structure in wall turbulence. arXiv, abs/1301.7580, 2013a.

A. S. Sharma and B. J. McKeon. On coherent structure in wall turbulence. J. Fluid Mech., 728:196–238, 2013b.

A. S. Sharma, J. F. Morrison, B. J. McKeon, D. J. N. Limebeer, W. H. Koberg, and S. J. Sherwin. Relaminarisation of $Re_\tau = 100$ channel flow with globally stabilising linear feedback control. Phys. Fluids, 23 (12):125105, 2011. doi: 10.1063/1.3662449. URL `http://link.aip.org/link/?PHF/23/125105/1`.

M. Shimizu and S. Kida. A driving mechanism of a turbulent puff in pipe flow. Fluid Dyn. Res., 41(045501), 2009.

A. J. Smits, B. J. McKeon, and I. Marusic. High Reynolds number wall turbulence. Annu. Rev. Fluid Mech., 43:353–375, 2011.

P. R. Spalart, R. D. Moser, and M. M. Rogers. Spectral methods for the Navier-Stokes equations with one infinite and two periodic directions. J. Comp. Phys., 96(2):297, 1991.

D. B. Spalding. A single formula for the law of the wall. ASME Trans., Series E: J. Appl. Mech., 28:455–458, 1961.

K. R. Sreenivasan. A unified view of the origin and morphology of the turbulent boundary layer structure. In Turbulence management and relaminarisation; Proceedings of the IUTAM Symposium, Bangalore, India, Jan. 13-23, 1987 (A89-10154 01-34). Berlin and New York, Springer-Verlag, pages 37–61, 1988.

G. I. Taylor. The spectrum of turbulence. Proc. R. Soc. Lond. A, 164:476–490, 1938.

T. Theodorsen. Mechanism of turbulence. In Proc. 2nd Midwestern Conf. on Fluid Mech., pages 1–19, Columbus, Ohio, 1952. Ohio State University.

C. D. Tomkins and R. J. Adrian. Spanwise structure and scale growth in turbulent boundary layers. J. Fluid Mech., 490:37–74, 2003.

C. D. Tomkins and R. J. Adrian. Energetic spanwise modes in the logarithmic layer of a turbulent boundary layer. J. Fluid Mech., 545:141–162, 2005.

A. A. Townsend. The Structure of Turbulent Shear Flows. Cambridge Univ. Press, 2nd edition, 1976.

L N Trefethen, A E Trefethen, S Reddy, and T A Driscoll. Hydrodynamic stability without eigenvalues. Science, 261(5121), July 1993.

M. Tutkun, W. K. George, J. Delville, J.-M. Foucaut, S. Coudert, and M. Stanislas. Space-time correlations from a 143 hot-wire rake in a high Reynolds number turbulent boundary layer. AIAA 2008-4239, 2008.

C. W. H. van Doorne and J. Westerweel. The flow structure of a puff. Phil. Trans. R. Soc., 367:489, 2009.

F. Waleffe. On a self-sustaining process in shear flows. Phys. Fluids, 9(4):883–900, 1997.

M. P Wernet. Temporally resolved PIV for space-time correlations in both cold and hot jet flows. Meas. Sci. Technol., 18:1387–1403, 2007.

C. E. Willert and M. Gharib. Digital particle image velocimetry. Exp. Fluids, 10:181–193, 1991.

Y. Wu and K. T. Christensen. Population trends of spanwise vortices in wall turbulence. J. Fluid Mech., 568:55–76, 2006.

I. J. Wygnanski and F. H. Champagne. On transition in a pipe. Part 1: The origin of puffs and slugs and the flow in a turbulent slug. J. Fluid Mech., 59:281, 1973.

Y. Yang and D. I. Pullin. Geometric study of Lagrangian and Eulerian structures in turbulent channel flow. J. Fluid Mech., 674:67–92, 2011.

N. Young. An Introduction to Hilbert Space. Cambridge University Press, Cambridge, UK, 1988.

J. Zhou, R. J. Adrian, S. Balachandar, and T. M. Kendall. Mechanisms for generating coherent packets of haripin vortices in channel flow. J. Fluid Mech., 387:353–396, 1999.